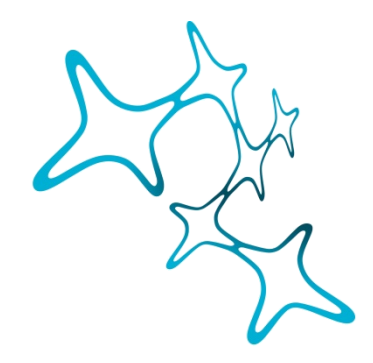
A human stem-cell-derived cortical tissue model to investigate Alzheimer's disease

Julien Klimmt



Graduate School of Systemic Neurosciences

LMU Munich



Dissertation at the Graduate School of Systemic Neurosciences Ludwig-Maximilians-Universität München

June 2022

Supervisor Prof. Dr. Dominik Paquet Institute for Stroke and Dementia Research University Hospital, LMU Munich

First Reviewer: Prof. Dr. Dominik Paquet Second Reviewer: Prof. Dr. Christian Haass External Reviewer: Prof. Dr. Jerome Mertens

Date of Submission: 09.06.2022 Date of Defense: 18.10.2022

Table of contents

A	bbreviati	ons	l
Α	bstract		1
1.	Intro	ductionduction	2
	1.1.	Alzheimer's disease	2
	1.1.1	. Autosomal-dominant AD and APP processing	3
	1.1.2	. The complex role of microglia in AD pathogenesis	4
	1.1.3	. Tau protein and neurofibrillary tangles	5
	1.1.4	. Interactions between the different AD hallmarks	6
	1.2.	Mouse models of Alzheimer's disease	7
	1.2.1	. Lack of human-specific pathology in AD mouse models	8
	1.3.	Human induced pluripotent stem cells (hiPSCs)	9
	1.3.1	. Differentiation of iPSCs into cortical neurons, astrocytes, and microglia	9
	1.3.2	. Approaches to increase physiological relevance of iPSC-derived in vitro models	11
	1.4.	iPSC-based modeling of Alzheimer's disease	12
	1.4.1	iPSC-derived 2D AD models	12
	1.4.2	iPSC-derived 3D AD models	13
	1.4.3	. Chimeric iPSC-based AD models	14
	1.5.	CRISPR/Cas genome editing	15
	1.5.1	. CRISPR/Cas-based disease modelling	16
	1.6.	Hypothesis and aims of the thesis	16
2.	Mate	rials and Methods	18
	2.1.	iPSC lines	18
	2.2.	iPSC maintenance	18
	2.3.	CRISPR/Cas9 gene editing design	18
	2.4.	sgRNA Testing in HEK293 cells	19
	2.5.	iPSC Electroporation	19
	2.6.	Puromycin selection and clonal expansion of electroporated iPSCs	19
	2.7.	Analysis of single cell clones	20
	2.7.1	. Replica Split and Crude Lysate preparation	20
	2.7.2	. Genotyping PCR	20
	2.7.3	. Restriction enzyme digest and expansion and banking of positive clones	21
	2.8.	Quality controls of edited iPSCs	21
	2.8.1	Fingerprinting PCR	21
	2.8.2	. ggPCR Assays to verify allele number at edited locus and BCL2L1 gene locus	21

	2.8.3	3. Off-target analysis	22
	2.8.4	l. Clonality check	22
	2.8.5	5. Pluripotency stainings of iPSCs	22
	2.8.6	5. Molecular Karyotyping	22
	2.9.	Cortical neuron differentiation from iPSCs	22
	2.10.	Astrocyte differentiation from iPSCs	24
	2.11.	Microglia differentiation from iPSCs	25
	2.12.	Long-term 2D cultures	26
	2.13.	Long-term 3D cultures – Matrigel cultures	26
	2.14.	Long-term 3D cultures – 3BTMs	26
	2.15.	Immunofluorescence stainings	27
	2.16.	Amyloid-β measurements in supernatant	29
	2.17.	Sequential protein extraction	29
	2.18.	SDS-PAGE and Western Blotting	30
	2.19.	Electrophysiological measurements	31
	2.20.	2-Photon live cell imaging	32
	2.21.	Single-cell RNA sequencing (scRNAseq)	32
	2.22.	Mass spectrometry	33
	2.22.	.1. Sample Preparation	34
	2.22.	.2. LC-MS/MS analysis	34
	2.22.	.3. Data Analysis	34
	2.23.	Statistical analysis	35
3.	Resu	ılts	37
	3.1.	Differentiation of human iPSCs into neurons, astrocytes, and microglia	37
	3.2.	Generation and optimization of 3D co-cultures of iPSC-derived brain cell types	39
	3.3.	Characterization of 3BTMs	42
	3.4.	Knock-in of synergistic AD mutations using CRISPR/Cas genome editing	46
	3.4.1	L. Quality controls of the established APP triple knock-in line	48
	3.5.	AD phenotypes in knock-in 3D cultures	48
	3.5.1	L. Aβ production and accumulation	48
	3.5.2	2. Effect of APP triple KI on phospho-Tau levels	49
	3.5.3	3. Analysis of global disease-associated alterations using transcriptomics	51
	3.5.4	1. Effect of disease-modifying and external factors on Aβ plaque formation	52
4.	Discu	ussion	56
	4.1.	Additional characterization of 3BTMs	57
	4.2.	Further improvement of 3BTMs	58

4	.3.	Discussion of AD-related phenotypes	60
4	.4.	Induction of Aβ plaque pathology in 3BTMs	62
4	.5.	Summary and Outlook	65
5.	Refe	rences	66
6.	Dank	rsagung	V
7.	Curr	iculum Vitae – Julien Klimmt	VI
8.	List o	of publications	VII
9.	Eide	sstattliche Erklärung/Affidavit	. VIII
10.	D	eclaration of author contributions	IX

Abbreviations

2D 2-dimensional

3BTM 3-dimensional cortical brain tissue model

3d 3 days

3D 3-dimensional 3mo 3 months

3R Tau Tau isoforms with 3 repeat domains
4R Tau Tau isoforms with 4 repeat domains

5FU 5-Fluoro-Uracil
μl Microliter
Aβ Amyloid Beta
AD Alzheimer's Disease

ADAD Autosomal-Dominant Alzheimer's Disease
AICD Amyloid Precursor Protein Intracellular Domain

AIM Astrocyte Induction Medium

AM Astrocyte Medium
ANOVA Analysis of Variances
ApoE Apolipoprotein E

APP Amyloid Precursor Protein

APP^{Swe/Arc/lbe} APP carrying the Swedish (Swe), Arctic (Arc) or Iberian (Ibe) mutations

AQP4 Aquaporin 4 AS Astrocytes

BACE Beta-site Amyloid-Precursor-Protein-Cleaving Enzyme

BCL2L1 B-Cell-Lymphoma-2-Like 1
bFGF Basic Fibroblast Growth Factor
BMP Bone Morphogenic Protein
BSA Bovine Serum Albumin
C3 Complement Component 3

Cas Clustered Regularly Interspaced Short Palindromic Repeats Associated Protein

CD11b/68 Cluster of Differentiation 11b/68

c-myc Cellular Myelocytomatosis CNTF Ciliary Neurotrophic Factor

CRISPR Clustered Regularly Interspaced Short Palindromic Repeats

CSPG Chondroitin Sulphate Proteoglycan

CTF C-Terminal Fragment

CTIP2 Chicken Ovalbumin Upstream Promoter Transcription Factor Interacting Protein 2

DAM Disease-Associated Microglia
DAPI 4',6-Diamidino-2-Phenylindole

DAPT N-[N-(3, 5-Difluorophenacetyl)-l-Alanyl]-s-Phenylglycine-T-butyl ester

DEA Diethylamine
DIV Day *In Vitro*

DM1 Microglia Differentiation Medium 1
DMEM Dulbecco's Modified Eagle's Medium

DMSO Dimethylsulfoxide
DNA Deoxyribonucleic Acid
E8F "Essential 8 Flex" Medium

EAAT1 Excitatory Amino Acid Transporter 1
ECL-IA Electrochemiluminescence Immunoassay

ECM Extracellular Matrix

EDTA Ethylenediaminetetraacetic Acid

EGF Epidermal Growth Factor EM Electron Microscopy

EPSP Excitatory Postsynaptic Potentials

FBS Fetal Bovine Serum

GABA Gamma-aminobutyric Acid

gDNA Genomic DNA

GEM Glial Precursor Expansion Medium
GFAP Glial Fibrillary Acidic Protein

GLAST Glutamate Aspartate Transporter 1

GLT1 Glutamate Transporter 1
GPC Glial Precursor Cell

GT Geltrex Gua Guanidine

HAPLN4 Hyaluronan and Proteoglycan Link Protein 4

HDR Homology-Directed Repair
HEK Cells Human Embryonic Kidney Cells

HemA/B Hematopoietic Differentiation Medium A/B (H)iPSCs (Human) Induced Pluripotent Stem Cells

HPCs Hematopoietic Precursor Cells

HRP Horseradish Peroxidase

HSPG Heparan Sulphate Proteoglycan

Iba1 Ionized Calcium Binding Adaptor Molecule 1

IF Immunofluorescence

IL34 Interleukin 34

InDels Insertions and Deletions

iNs Induced Neurons

KI Knock-in

Klf4 Krüppel-Like Factor 4
LIF Leukemia Inhibitory Factor

MAP2 Microtubule-Associated Protein 2
MAPT Microtubule-Associated Protein Tau
M-CSF Macrophage Colony Stimulating Factor

MG Microglia mRNA Messenger RNA

NB(+) Neurobasal (Plus) Medium

NE Neurons

NEAA Non-Essential Amino Acids NeuroD1 Neurogenic Differentiation 1

NFIA Nuclear Factor 1a
NFIB Nuclear Factor 1b
Ngn2 Neurogenin 2

NHEJ Non-Homologous End Joining NI Neural Induction Medium

NL-G-F Combination of APP Swedish (NL), Arctic (G), And Iberian (F) Mutations

NM Neural Maintenance Medium

NPC Neural Precursor Cell

NRSR Neural Rosette Selection Reagent
OCT4 Octamer-Binding Transcription Factor 4

OT Off-Target

P2RY12 Purinergic Receptor P2Y12 PAM Protospacer Adjacent Motif

PBMC Peripheral Blood Mononuclear Cell

PBS Phosphate-Buffered Saline PCR Polymerase Chain Reaction

PFA Para-Formaldehyde
PHF1 Paired Helical Filament 1

pmol Picomole

pOL Poly-Ornithine + Laminin (coating)

PSD95 Postsynaptic Density 95

PSEN1/2 Presenilin 1/2 pTau Phospho-Tau

qgPCR Quantitative Genomic PCR

RFLP Restriction Fragment Length Polymorphism

RI Rock Inhibitor

RIPA Radioimmunoprecipitation Assay buffer

RNA Ribonucleic Acid
RNP Ribonucleoprotein
RPM Rounds Per Minute
RT Room Temperature
RVC "Revitacell" Supplement
SAD Sporadic Alzheimer's Disease

SATB2 Special AT-Rich Sequence-Binding Protein 2

scRNAseq Single Cell RNA Sequencing

SD Standard Deviation SF "Stemflex" Media sgRNA Single Guide RNA

SMAD "Small" "Mothers Against Decapentaplegic" Protein

Sox2 SRY (Sex Determining Region Y)-Box 2
Sox9 SRY (Sex Determining Region Y)-Box 9
SSEA4 Stage-Specific Embryonic Antigen 4
ssODN Single-Stranded Oligodeoxynucleotides

TALENS Transcription Activator-Like Effector Nucleases

TERT Telomerase Reverse Transcriptase
TGF-B Transforming Growth Factor Beta

Thr Threonine

TMEM119 Transmembrane Protein 119
TRA-1-60 T Cell Receptor Alpha Locus 1-60

TREM2 Triggering Receptor Expressed on Myeloid Cells 2

TTX Tetrodotoxin

TUNEL Terminal Deoxynucleotidyl Transferase dUTP Nick End Labelling

ULA Ultra-low attachment

VTN Vitronectin WT Wildtype

YFP Yellow Fluorescent Protein

Abstract

Alzheimer's disease (AD) is the most common cause of dementia, affecting millions of people worldwide. Despite decades of research, development of mechanism-based AD treatments has been highly difficult and fundamental pathomechanisms remain poorly understood. Both development of disease-modifying treatments and underlying basic research heavily depend on model systems, especially transgenic mice. Therefore, drawbacks of these models, such as species differences or incompleteness of phenotypes and pathologies, may contribute to the failure of drugs in human patients.

Induced pluripotent stem cell (iPSC-)based AD models enable investigation of pathomechanisms in human, disease-relevant brain cell types and thus offer great potential for mechanistic and translational studies. In addition, human iPSC-based models allow time course analyses of disease processes during early and advanced AD pathogenesis, a crucial time window where therapeutic interventions may still be able to stop or even cure the disease. However, current iPSC-AD models often show low reproducibility and cell type diversity and lack physiological human cell-cell and cell-matrix contacts. In addition, they typically only enable investigation of early pathologies including endosomal abnormalities and A β accumulation but lack hallmarks such as neuroinflammation and widespread protein aggregation.

Therefore, the first aim of this thesis was the development of a reproducible and controllable, iPSC-based cortical tissue model made of multiple human brain cell types in a 3D environment. The second aim was to characterize and validate this model on a cellular and functional level, and finally apply it to study AD pathogenesis and underlying disease mechanisms.

To achieve these aims, we first adopted and optimized protocols to differentiate human iPSCs into highly pure cultures of disease-relevant cortical neurons, astrocytes, and microglia. We then used these differentiated cell types to generate modular, 3D cortical brain tissue models (3BTMs) by using the self-aggregating potential of the cells. The resulting cultures display a dense and stable network of mature neurites and astrocytic processes that is tiled by ramified microglia. Further characterizations demonstrate that 3BTMs are postmitotic, show only minimal levels of cell death and no necrotic core formation, and form a brain-like ECM as well as functional synapses over time. Incorporated microglia are phagocytically active, surveil the environment and react to focal laser injuries in 2-photon live cell imaging.

To induce AD pathogenesis in our model system, we knocked in synergistic, AD-causing APP mutations into iPSCs using the CRISPR/Cas9 system. When analyzing our AD knock-in 3BTMs, we found an increased A β secretion and A β 42:40 ratio, a time- and cell-type-dependent accumulation of extracellular A β , increased phospho-Tau levels and potential microglial activation. To trigger late-stage phenotypes such as protein aggregation into A β plaques, we applied seeding approaches with mouse brain lysate and recombinant, human A β 42. Seeding with synthetic A β 42 led to the formation of plaque-like structures with surrounding Tau pathology, indicating axonal dystrophy, after 1 month.

Altogether, we established a human 3D *in vitro* model with several advantages over currently used cultures regarding controllability, reproducibility, modularity, and cell type diversity. We further demonstrate the suitability of the model to investigate AD and potentially other neurological diseases. This new model system will provide a basis to dissect fundamental, potentially human-specific pathomechanisms and enable the field to discover novel therapeutic targets and develop and test disease-modifying compounds.

1. Introduction

1.1. Alzheimer's disease

Clear thinking, remembering, and reasoning are at the core of human cognitive function and social interactions. Their loss therefore strongly interferes with daily life and social activities, and defines the state called dementia. Alzheimer's disease (AD) is the most common cause of dementia, affecting around 32 million people worldwide, with case numbers projected to increase due to the aging of the global society ¹. This poses enormous personal, social, and economic burdens onto families, caretakers, and societies. AD was first described by Alois Alzheimer in 1907², but despite decades of research, only symptomatic drugs are currently approved for the treatment of AD in Europe. These drugs may temporarily relieve symptoms but do not target the underlying causes of the disease and can therefore only delay, but not prevent the progressive deterioration of cognitive function. Recently, an antibodybased, potentially disease-modifying therapy was conditionally approved in the US but refused in Europe due to conflicting study results and subsequent unclear efficacy, combined with high risk of side effects, such as brain swellings 3. Accordingly, there are no therapies available that target the underlying disease mechanisms and no possibility to halt or even cure the disease. Reasons for this include the unique vulnerability of humans to AD 4 and the very protracted course of the disease over several years or decades 5,6. This impairs the development of accurate disease models, leading to a lack of understanding of the underlying, potentially human-specific pathomechanisms. In addition, the different causes of AD are not yet fully understood, especially in the case of so called "sporadic" AD (sAD) that represents the majority of cases. While studies identified several factors increasing the risk for sAD, the strongest one being increasing age ^{7,8}, there is likely an individually distinct, complex interplay of genetic and environmental factors underlying the pathogenesis. However, a small number of cases (probably <1 % 9) are caused by monogenetic mutations and termed autosomal dominant AD (ADAD). Interestingly, although the individual causes vary, the resulting early and late histopathological hallmarks are very similar in sAD and ADAD cases ^{9,10}. These hallmarks include aggregation of amyloidbeta (Aβ) peptide into extracellular plaques, aggregation of Tau protein into intracellular tangles, neuroinflammation and neurodegeneration (Figure 1).

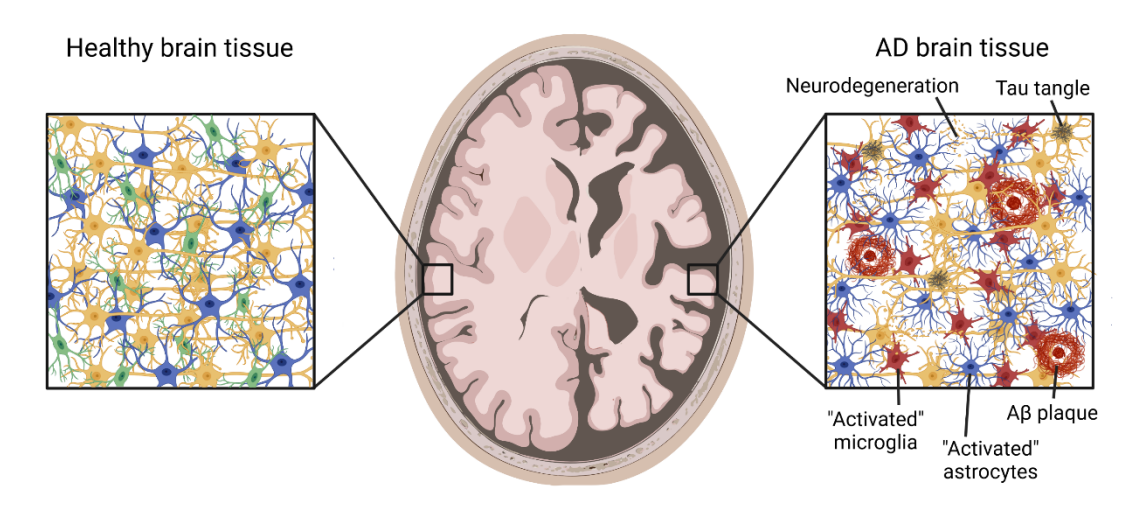


Figure 1: Comparison of healthy and Alzheimer's disease (AD) brain tissue. Schematic showing neurons (yellow), astrocytes (blue) and microglia (green) in healthy brain tissue (left) and AD brain (right). Note the significant atrophy of cortical regions and enlargement of ventricles in AD-affected brain. AD-affected brain tissue displays amyloid beta $(A\beta)$ plaques, Tau tangles, activated microglia and astrocytes causing neuroinflammation, and neurodegeneration.

Assuming that the underlying pathomechanisms are as similar as the resulting pathology, most research on general AD pathogenesis focuses on ADAD, as it can be modeled by the introduction of known mutations into the respective genes of a model organism or cell.

1.1.1. Autosomal-dominant AD and APP processing

The genes affected by ADAD mutations are coding for amyloid precursor protein (APP), presenilin 1 (PSEN1), or presenilin 2 (PSEN2). APP is a transmembrane protein that is cleaved by different proteases to shed a variety of peptides including A β (Figure 2). Originally, two cleavage pathways were described with the first cleavage performed by either alpha (α -) secretase ¹¹ or beta (β -) secretase ¹², starting the non-amyloidogenic (non-A β -producing) or amyloidogenic (A β producing) pathway, and releasing soluble APP α (sAPP α) or sAPP β and C-terminal fragment α (CTF α) or CTF β , respectively. The second series of cuts is then performed by gamma (γ -) secretase, releasing either the p3 or amyloid-beta (A β) peptides as well as an APP intracellular domain (AICD). More recently, another processing pathway has been described, starting by eta (η -) secretase cleavage and the shedding of soluble APP η , followed by either α - or β -secretase cleavage releasing A η - α or A η - β , respectively ¹³. The resulting C-terminal fragments can then be cleaved by γ -secretase to produce p3 or A β peptides as well as the AICD (Figure 2).

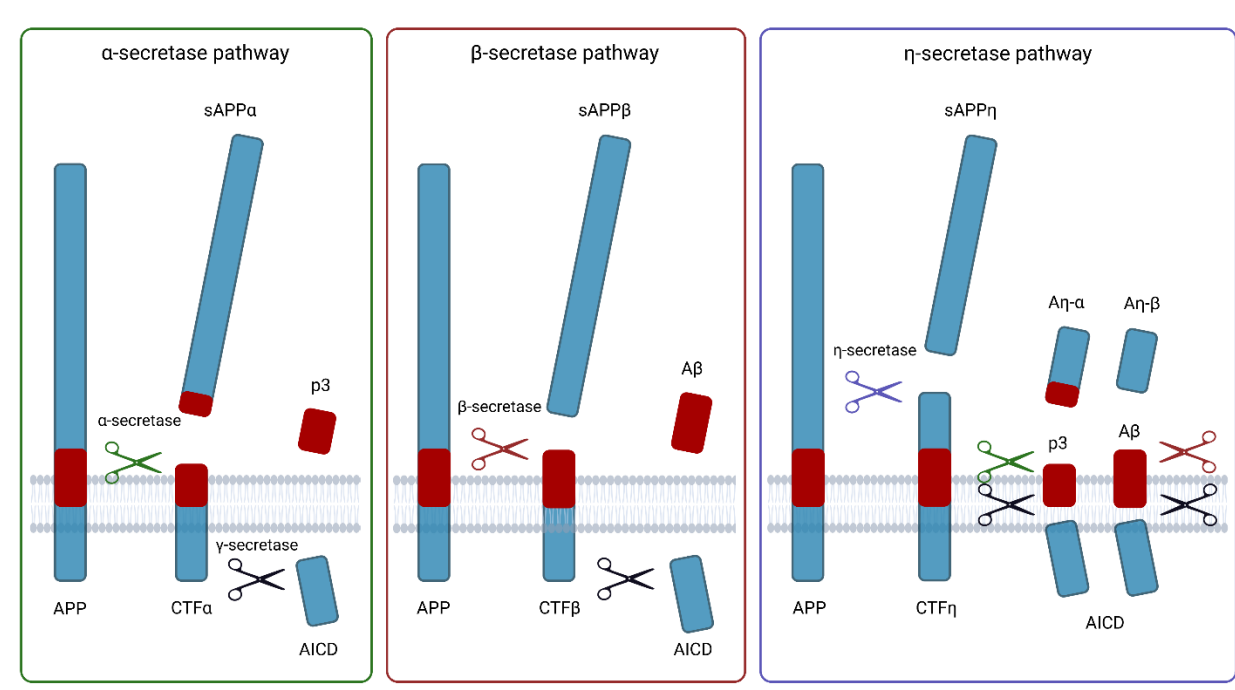


Figure 2: Amyloid precursor protein (APP) processing pathways. Left: APP processing following the non-amyloidogenic, α -secretase pathway yields soluble APP α (sAPP α) and C-terminal fragment α (CTF α) after α -secretase cleavage. CTF α can then further be processed by γ -secretase to produce p3 peptide and the APP intracellular domain (AICD). **Middle:** APP processing following the amyloidogenic, β -secretase pathway yields sAPP β and CTF β after cleavage by β -secretase. CTF β can then further be processed by γ -secretase to produce amyloid- β (A β) peptide as well as AICD. **Right:** APP processing following the γ -secretase pathway first yields CTF γ and sAPP γ . CTF γ can be processed by either γ - or γ -secretase to yield A γ - γ and CTF γ 0 or A γ 1- γ 3 and CTF γ 4, respectively. The CTFs can be further processed by γ -secretase as described above. Modified from Sasaguri et al. ¹⁴.

PSEN1 or PSEN2 are the catalytic subunits of γ -secretase 15,16 and therefore an essential part of this A β producing pathway. This highlights the importance of the pathway in AD and led to the amyloid cascade hypothesis that places the accumulation and aggregation of A β as the initial trigger of AD pathogenesis 17,18 . Both amyloidogenic and non-amyloidogenic pathways are constitutively active in the human brain 19,20 and the resulting fragments perform important physiological functions, for example in regulating synaptic transmission and network activity 21,22 . The physiological roles of A β are still not fully understood, but some studies hint towards a function in long-term potentiation and hippocampus-dependent memories 23,24 as well as an antimicrobial function that is leveraging the

oligomerization and aggregation potential of the peptide to bind, trap and thus neutralize pathogens in the brain 25,26 . In AD, the A β peptide is aberrantly aggregating into oligomers, fibrils and finally dense plaques that consist of a core of highly compacted, fibrillar A β surrounded by a halo of smaller, more soluble fibrils 27 and oligomers 28 . As mentioned above, this accumulation and aggregation of A β into plaques is one of the pathological hallmarks of AD and is detectable years to decades before cognitive impairments occur 29 . This means that therapies targeting the aggregation process, such as antibody therapies removing A β accumulations, would likely need to be started in this very early time window to be successful. However, A β plaque pathology does not correlate well with cognitive decline in patients 30 and it is hypothesized that plaques themselves are not necessarily toxic, but may be the product of the brains attempts to compact and render the smaller, toxic species such as oligomers 31 , harmless 32 .

1.1.2. The complex role of microglia in AD pathogenesis

Recent studies propose that microglia, the brains innate immune cells, perform this protective function of compaction and engulfment of $A\beta^{32,33}$. This also explains histological findings that show microglia surrounding $A\beta$ plaques ³⁴ like a barrier, and increased neuronal damage and loss if this barrier is impaired ^{35,36}, again highlighting a protective role of microglia in AD pathogenesis. However, the microglial response to amyloid pathology may not only be beneficial. For example, it has been shown recently that microglia which phagocytosed plaque-associated $A\beta$ can facilitate the spread of amyloid pathology by carrying the phagocytosed $A\beta$ seeds and releasing them elsewhere ³⁷. In addition, the microglial reaction is accompanied by a general proliferation and "activation" of the cells, called microgliosis, leading eventually to a neuroinflammatory environment ³⁸. This neuroinflammation is another hallmark of AD and other neurodegenerative diseases and characterized for example by increased secretion of pro-inflammatory cytokines by microglia ³⁹. These cytokines can in turn activate astrocytes ⁴⁰, enhancing the inflammatory phenotype, and potentially leading to neuronal and oligodendrocytic degeneration ^{40,41} (Figure 3). In addition, studies in mice showed that the continuous microglial activation leads to an "exhaustion" of the cells with age, resulting in a loss of the protective functions mentioned above ^{42,43}.

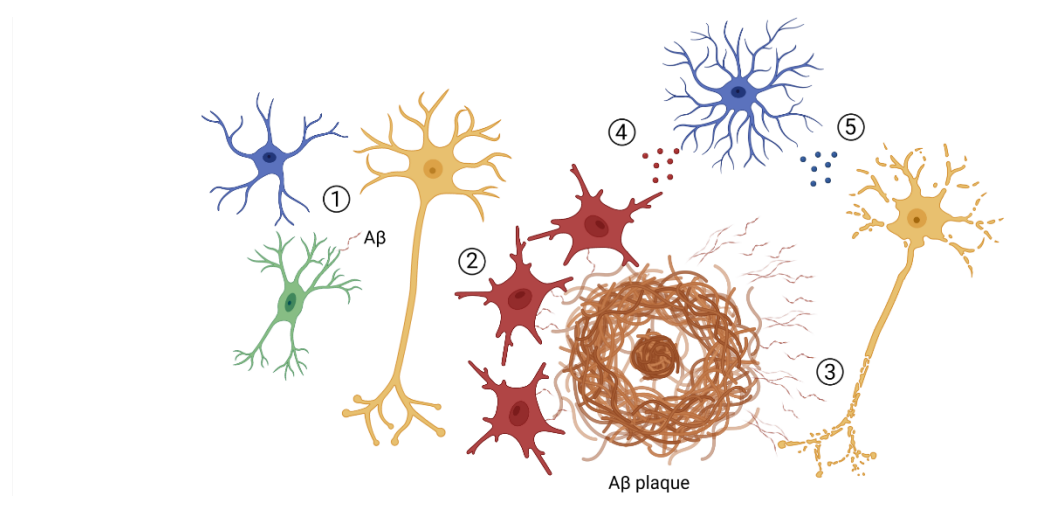


Figure 3: Simplified depiction of microglial roles in AD pathogenesis. Protective functions of microglia (green) include 1) uptake of $A\beta$ which is constantly produced by neurons (yellow) and interactions with astrocytes (blue) and 2) barrier formation of activated microglia (red) around $A\beta$ plaques to limit exposure of surrounding cell types such as neurons to toxic $A\beta$ species. 3) If microglial barrier function is lost, neuronal damage and degeneration is increased. 4) Activated microglia can have detrimental effects by excessive production of pro-inflammatory cytokines which 5) activate astrocytes that in turn secrete toxic factors promoting neuronal degeneration. Modified from Hansen et al. ⁴⁴.

The important role of microglia in AD is underscored by the fact that most AD risk genes found in genome-wide association studies are strongly expressed by microglia in the brain 45, suggesting that microglial function and reaction are central processes in the pathogenesis. One of the strongest risk genes is "triggering receptor expressed on myeloid cells 2" (TREM2) 46,47 and it has been shown that expression of the AD-associated variant TREM2 R47H leads to a TREM2-knockout-like transcriptomic state 48 as well as impaired phagocytosis of A β 49,50 , suggesting that the variant causes a loss of function and impairs microglial reactivity. This in turn would indicate that microglial activation is an overall protective process. All these results together suggest a complex role of microglia in AD pathogenesis that is not yet understood. The microglial activation state, which under physiological conditions is a flexible balance that is carefully controlled, may become imbalanced in either direction, i.e. hypo- or hyperactivation, over the course of the disease. This may again have ambiguous consequences, either promoting or inhibiting disease progression, depending on the current cell state, e.g. "healthy" or "exhausted", the cell environment, e.g. plaque-associated or not, and the disease stage. This intricate, time- and environment-dependent interplay makes it highly difficult to exploit the large therapeutic potential of targeting microglial activation. Therefore, more research is needed to understand the mechanisms underlying and consequences of interfering with this process.

1.1.3. Tau protein and neurofibrillary tangles

Another hallmark of AD are neurofibrillary tangles - intracellular protein aggregates made mainly of Tau 51,52, a microtubule-associated protein encoded by the MAPT gene. By alternative splicing, six different isoforms of Tau can be produced ⁵³ that differ in the number of a specific N-terminal domain (0N, 1N or 2N) as well as the number of repeat domains close to the C-terminus (3R with three repeat domains or 4R with four) (Figure 4). In the fetal human brain, almost exclusively 3R Tau is found, but during the perinatal period there is a rapid shift in isoform expression, leading to a 3R to 4R ratio of approximately 1:1 in the adult human brain ⁵⁴. Tau is an intrinsically disordered protein ^{55,56} that under physiological conditions is essential for microtubule dynamics ⁵⁷ and important for axon elongation and maturation 58,59, maintaining DNA and RNA integrity under oxidative stress 60,61 and regulation of brain insulin signaling 62. In AD, Tau gets hyperphosphorylated 63 on various epitopes, e.g. Threonine 181, 217 and 231, early in disease and can serve as a blood ^{64–66} or cerebrospinal fluid biomarker ^{67–69} of disease progression. Besides hyperphosphorylation, Tau is mislocalized from axonal to somatodendritic compartments ^{70,71}, misfolds ^{72,73} and adopts a highly AD-specific, aggregation prone conformation 74, leading to accumulation of both the 3R and 4R isoforms of the protein and finally their aggregation into Tau tangles inside neurons ⁵³ (Figure 4). As with Aβ aggregation it is not fully understood which Tau species confer toxicity, but it has been shown that small oligomeric Tau species are toxic to neurons 75, and that the ability to aggregate is required for toxicity in vitro 76.

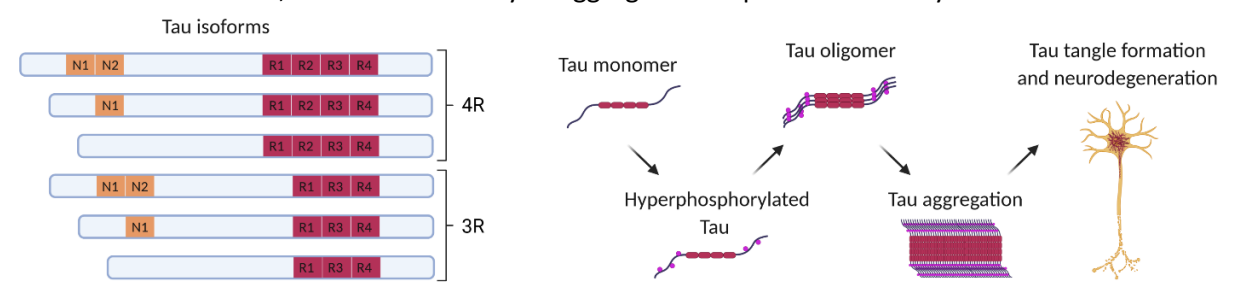


Figure 4: Tau isoforms and pathogenic Tau aggregation pathway. Left: Depiction of the 6 Tau isoforms expressed in adult human brain that differ in the number of an N-terminal domain (N1/N2) and the number of C-terminal repeat domains (R1-R4) leading to 3R and 4R isoforms. Right: In AD, Tau gets hyperphosphorylated and aggregates into oligomers and larger fibrils, leading to the formation of Tau tangles inside neuronal cell bodies and neurodegeneration.

1.1.4. Interactions between the different AD hallmarks

Ultimately, AB plaques, neuroinflammation, and Tau tangles likely cause neurodegeneration, but the exact mechanisms connecting the different pathologies and how they eventually lead to cell death are still under debate. Tau tangle pathology correlates better with cortical atrophy 77, a sign of neurodegeneration, and general disease severity compared to amyloid plaques 30,78. In addition, it was found that deletion of Tau in AD mouse models ameliorates plaque deposition ⁷⁹, synapse and neuron loss as well as memory deficits 80. On the other hand, various studies in mouse models suggest that Aβ pathology strongly enhances Tau spreading and tauopathy phenotypes and increases neurodegeneration in tauopathy models ^{81–84}. In addition, it has been shown that small Aβ oligomers can cause hyperphosphorylation of Tau at AD-relevant epitopes 85 as well as somatodendritic mislocalization 86. In humans, a neuroimaging study indicates that both Aβ and Tau pathology are necessary for memory decline 87. Overall, these studies suggest that there may be a bidirectional relationship between AB and tau, with AB pathology promoting Tau spreading, phosphorylation and mislocalization and with the resulting Tau pathology in turn enhancing $A\beta$ pathology. Interestingly, histological studies of human non-demented and AD patient brains have shown that Aβ and Tau pathologies originate in distinct brain regions, and then spread, likely along axon tracts, to anatomically connected regions throughout the brain ^{88,89} (Figure 5). Aβ pathology starts in the basal temporal cortex and then spreads heterogeneously into other isocortical and finally subcortical areas 90-92, while Tau tangles are first found in the transentorhinal cortex and hippocampal formation, only later spreading into isocortical areas ⁹⁰, likely facilitated by the Aβ pathology present there ⁹³. This suggests that there could be a time window, also called preclinical AD ¹⁴, during which disease progression may still be slowed or halted. This may be achieved by removing cortical amyloid pathology, thereby preventing the spread of Tau pathology before they coincide and reinforce each other in isocortical areas. However, to achieve this or treat AD even at later stages, a deeper understanding of the underlying pathomechanisms and interactions is required. Therefore, ever since these histopathological hallmarks and the ADAD-causing mutations were described, researcher aimed to mimic AD pathologies in model systems to study the underlying mechanisms and find therapeutics to modulate them.

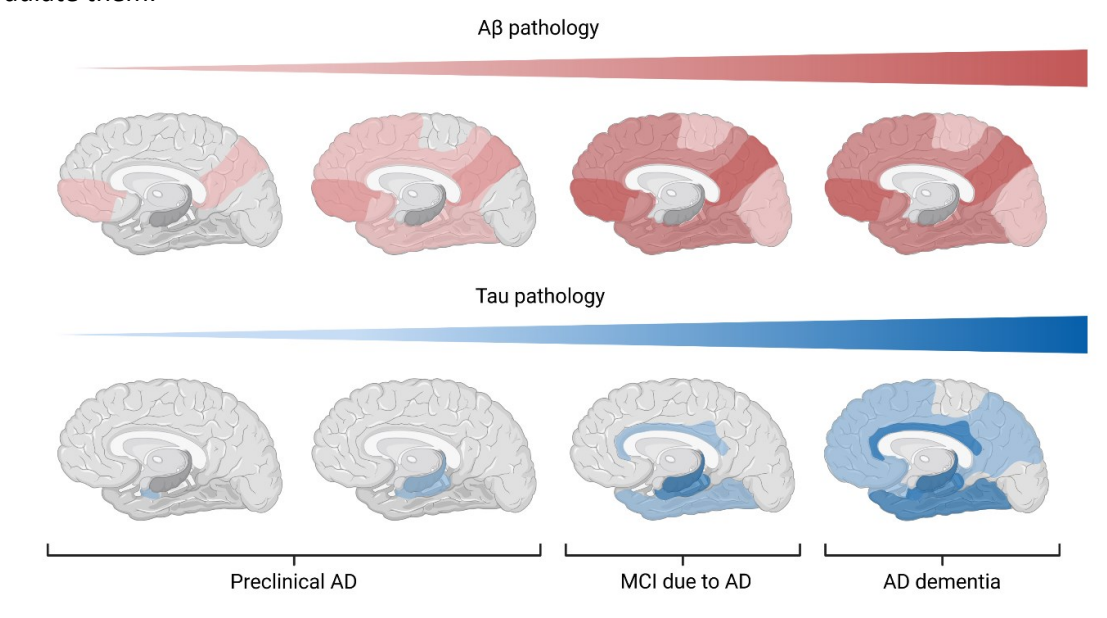


Figure 5: Spread of A β and Tau pathologies in AD. Top: A β pathology starts in association areas in the cortex and spreads mainly to other isocortical areas with little changes in pathology severity during later stages of the disease – from mild cognitive impairment (MCI) to AD dementia. Bottom: Tau pathology starts in the transentorhinal cortex and spreads to the hippocampal formation and only in the later stages into the cortex, likely facilitated by the A β pathology present there. In preclinical stages of the disease, both pathologies are still spatially separated, potentially opening a therapeutic window. Data is summarized from positron emission tomography (PET) and neuropathological studies. Modified from van der Kant et al. ⁹⁴

1.2. Mouse models of Alzheimer's disease

For years, AD was mostly modelled and studied in mice overexpressing mutant forms of (human) APP and PSEN1 and combinations thereof 95. Although mice do not naturally develop Alzheimer's disease, these models show aggregation and deposition of AB in plaques within few months as well as concomitant micro- and astrogliosis 96,97. In addition, an increase in neurofilament light chain (NfL) levels in body fluids 98 and increased tau phosphorylation 96 have been observed in some models, suggesting starting axonal degeneration and early tauopathy phenotypes as described above. However, these models fail to recapitulate AD hallmarks such as Tau tangle formation and subsequent neurodegeneration if only AD-causing mutations are introduced. In addition, these mouse models have several limitations, including the possible destruction of endogenous loci at transgene insertion as well as unspecific effects and artificial phenotypes due to the overexpression of APP itself and all its cleavage products, not only Aβ, and subsequent aberrant interactions with other cellular proteins ¹⁴. It has been shown for example that the neurodegeneration seen in a commonly used Tauopathy mouse model was not due to overexpression of human Tau alone, but rather due to the insertion of ~70 copies of the transgene that disrupted a gene encoding for a growth factor needed for neuronal survival 99. To avoid these caveats, knock-in mouse models were developed by introduction of a combination of AD-causing mutations into the humanized, endogenous APP gene in the mouse genome 100-102. Most prominently, NL-G-F mice carrying the APP Swedish (APPSwe), Arctic (APPArc) and Iberian (APP^{lbe}) mutations ¹⁰⁰ are currently used ¹⁰¹ (Figure 6).

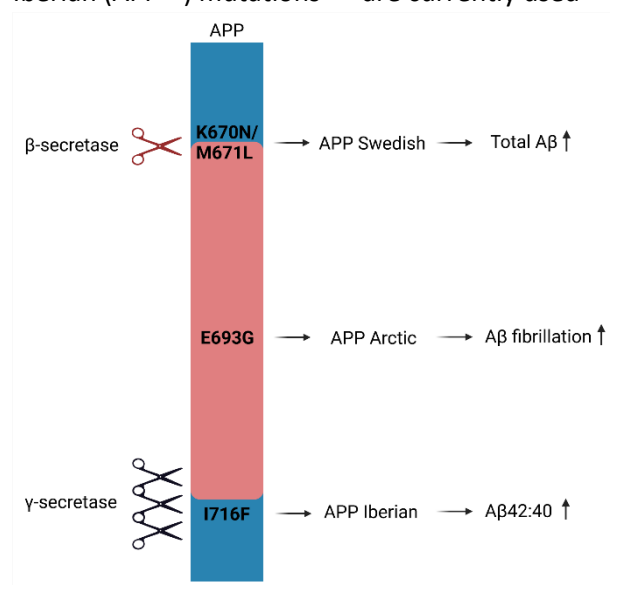


Figure 6: APP NL-G-F mutations and their effect on APP processing. APP Swedish mutation (K670N/M671L) is located right at the β -secretase cut site, thereby increasing total $A\beta$ production by promoting β -secretase over α -secretase cleavage. APP Arctic mutation (E693G) is located within the $A\beta$ peptide (red), accelerating $A\beta$ fibrillation. APP lberian mutation (I716F) is located within the γ -secretase cleavage region on position 45 of the $A\beta$ peptide, thereby altering γ -secretase cleavage and increasing the $A\beta42:40$ ratio.

The APP^{Swe} mutation is located close to the β -secretase cut site and has been shown to increase total A β levels ¹⁰³ by increasing β - compared to α -secretase cleavage, thereby promoting the amyloidogenic processing pathway ^{104–106}. APP^{Arc} is a mutation found in the middle of the A β peptide itself and has been shown to accelerate protofibril formation and thus the aggregation process ^{107,108}. The APP^{Ibe} mutation is found around the γ -secretase cut sites. γ -secretase cleavage is a sequential process that typically cleaves off tripeptides, starting at position 48 or 49 of the A β sequence ¹⁰⁹. Under physiological conditions, A β 40, consisting of 40 amino acids, is the most prominent cleavage product, with shorter (A β 37/38) and longer (A β 42/43) isoforms also present at lower amounts ^{110,111}. As amino acids 41-49 are largely hydrophobic, the longer isoforms are more aggregation prone and important for densecore plaque formation ^{112–114}. The APP^{Ibe} mutation has been shown to destabilize the γ -secretase-CTF complex *in vitro*, leading to higher dissociation probabilities and therefore on average longer, more aggregation-prone A β species ¹¹⁵. Indeed, the mutation strongly increases levels of A β 42 and decreases levels of A β 40 ¹¹⁶. The original study describing the NL-G-F mice ¹⁰⁰ also generated NL-F mice lacking

the APP^{Arc} mutation and could show that this slowed down Aβ aggregation, leading to cortical plaque formation only after around 9 months compared to 3 months in NL-G-F mice, thus demonstrating the synergistic effect of the different mutations. In addition, NL-G-F mice showed synapse loss and microgliosis as well as possible cognitive deficits after 6 months of age. NL-F mice in comparison developed cognitive deficits only after 10 months ¹¹⁷. However, both knock-in mouse models did not develop Tau tangle pathology or neurodegenerative phenotypes.

1.2.1. Lack of human-specific pathology in AD mouse models

The lack of Tau pathology may be explained by species-specific differences for example in general Tau biology and specifically splicing. In adult mice, only 4R Tau is expressed ¹¹⁸, while adult human neurons express approximately equal amounts of 3R and 4R Tau 54,118, with aberrations from this ratio in any direction leading to frontotemporal dementia, a neurodegenerative disease ^{119,120}. In addition, it was shown that both 3R and 4R Tau are part of the paired helical filaments that make up Tau tangles in AD 121, suggesting that adult mice may be unable to form these filaments and develop AD-specific tangle pathology. Supporting this hypothesis, a recent preprint shows that Tauopathy phenotypes such as hyperphosphorylation, misfolding and aggregation arise specifically in human neurons transplanted into AD mouse brains, but not in adjacent mouse neurons 122. Furthermore, as isoform expression is different in mice, molecular Tau interaction partners may be different and alternatively regulated, thus humanizing the MAPT gene would still not fully mimic human Tau biology. The lack of neurodegenerative phenotypes in mouse models may similarly be due to species-specific differences, as the transplantation study mentioned above and a previous study from the same group showed not only Tauopathy phenotypes, but also selective degeneration of human neurons transplanted into AD mice, while adjacent mouse neurons were unaffected ^{122,123}. As Tau pathology correlates with synapse and neuron loss, the lack of the first may also prevent the latter in mice.

In addition, although microglia respond to plaque pathology in both mice and humans, the resulting microglia transcriptional signature is rather different between the species 124-127, potentially because in human AD brain a combination of Aβ and Tau pathologies is present. In 2017, the first single-cell RNA seq (scRNAseq) study from a transgenic AD/amyloidosis mouse model was published. The authors found a population of disease-associated microglia (DAMs) that is mostly located close to amyloid plaques and displays a specific transcriptomic signature including upregulation of ApoE and TREM2, the two strongest genetic risk factors for AD, and other "activation" markers and downregulation of homeostatic genes such as P2RY12 and TMEM119 128. They also found the reaction to be a two-step process with a first, TREM2-independent and a second, TREM2-dependent stage. Another study confirmed this signature in another mouse model by Nanostring-based RNA expression analysis and showed the dependence of the activation on a TREM2-ApoE signaling pathway ¹²⁹. In addition, the publications showed that this DAM signature is not unique to AD, but is also found in normal aging as well as other neurodegenerative diseases such as amyotrophic lateral sclerosis (ALS) and multiple sclerosis (MS). This suggests that reactivity is a more general response, potentially to protein aggregation as DAMs clustered around amyloid plaques, or to neuronal degeneration and tissue damage as it was induced by phagocytosis of apoptotic neurons. The studies also showed increased expression of key genes in human AD brains by immunostainings and in-situ hybridization experiments. However, when Mathys et al. published the first single-nucleus RNA sequencing study from human AD patient brains, only a very small overlap of 28 out of 257 upregulated mouse DAM genes was conserved in the human samples 124. This overlap included the central DAM gene ApoE, suggesting that the fundamental activation pathways may be similar, but that downstream effectors and other genes may differ. For example, no significant upregulation of TREM2 was found in AD patient microglia in this study. Additional studies on AD post-mortem brains confirmed these differences between human and mouse, but found again different AD-associated microglial signatures, also compared to Mathys et al.,

to an extent that there is only one gene significantly upregulated in AD brain microglia in all human studies, which is ApoE ^{125,127,130,131}. This discrepancy may be due to the different brain regions studied, e.g. prefrontal cortex versus entorhinal cortex, and due to technical differences, such as the method of microglia isolation and the sequencing method and platform used, highlighting the need for more standardized and controlled studies. In addition, while post-mortem studies give unique insights into the human disease in patients, they only reflect the end stage of disease, when most pathological changes already occurred, and the therapeutic window is likely closed.

Therefore, to enable the analysis of earlier disease stages and pathomechanisms in a human system and complement mouse models and their drawbacks, it is important to develop human *in vitro* AD models. This can be achieved using the emerging potential of human induced pluripotent stem cells.

1.3. Human induced pluripotent stem cells (hiPSCs)

In 2006, a team led by Shinya Yamanaka discovered that mouse fibroblasts could be reprogrammed into "induced" pluripotent stem cells (iPSCs) by retroviral transduction of four transcription factors important for stem cell renewal and function, namely Oct4, Klf4, c-Myc and Sox2 ¹³². These iPSCs can be differentiated into cells of all germ layers of the embryo, yielding an almost unlimited resource of non-immortalized, karyotypically normal, somatic cells. In 2007, the reprogramming was adapted to human fibroblasts ¹³³, opening a new era of biomedical research, and leading to the Nobel prize in 2012. Since then, reprogramming techniques have been refined by delivering the transcription factors using non-integrating viruses ^{134,135}, plasmids ¹³⁶, episomal vectors ¹³⁷, recombinant peptides ¹³⁸, synthetic mRNA ¹³⁹ or micro RNAs ¹⁴⁰, and by optimizing reprogramming from different starting cell types that are easier to obtain, such as peripheral blood cells ^{141–144}, keratinocytes ¹⁴⁵, or renal tubular cells present in urine ¹⁴⁶. In addition, differentiation protocols for a variety of cell types have been published and optimized, enabling the study of different diseases and their underlying mechanisms in human, disease-relevant cell types.

1.3.1. Differentiation of iPSCs into cortical neurons, astrocytes, and microglia

In the case of AD, relevant cell types include for example cortical forebrain neurons, which are most affected by neurodegeneration, as well as astrocytes, and microglia, which are known to modulate disease progression as described above. For each of these cell types, differentiation protocols starting from iPSCs have been published ^{147–152}. These protocols often use small molecules and specific cytokines and growth factors to inhibit pathways important for pluripotency and to promote pathways that are active in the target lineage and cell type (Figure 7), recapitulating developmental cues found *in vivo*. Alternatively, overexpression of lineage-specific transcription factors can be used to yield differentiated cell types more quickly.

Cortical forebrain neurons are commonly differentiated using "dual-SMAD inhibition" to inhibit transforming growth factor beta (TGF β) and bone morphogenic protein (BMP) signaling, thereby suppressing the maintenance of pluripotency and promoting differentiation into the neural lineage, leading to the emergence of neural precursor cells (NPCs) ¹⁵³. By maintaining these NPCs at high density ^{153,154}, they can be differentiated into cortical forebrain, glutamatergic projection neurons, supported by the addition of retinoic acid as a patterning factor ¹⁴⁷. Following the stereotypical order of cortical layer formation in the human brain, the cells first form deep-layer neurons followed by mid- and upper-layer cells. The resulting cell population has been shown to express typical markers such as microtubule-associated protein 2 (MAP2) and β 3-Tubulin, form synapses and be electrically active in electrophysiological measurements ^{147,154}. However, the dual-SMAD inhibition approach yields (deep-layer) neurons only after around 4-5 weeks of differentiation. More recently, another approach has been published to generate induced neurons (iNs) from iPSCs within one week by short-term

overexpression of selected transcription factors such as neurogenin 2 (Ngn2) or Neurogenic differentiation 1 (NeuroD1) ¹⁵⁵. The original publication suggests that the resulting cells are an almost pure population of electrically active, excitatory neurons of mainly cortical layer 2/3. However, a more recent single cell analysis of the differentiated cells suggests a larger cellular heterogeneity including cells of more peripheral neuron identity, and that this variability depends on the exact differentiation protocol, e.g. duration of Ngn2 overexpression ¹⁵⁶. This indicates that the short-term expression of the transcription factor may not faithfully recapitulate normal human neuron development and needs to be tightly controlled and monitored.

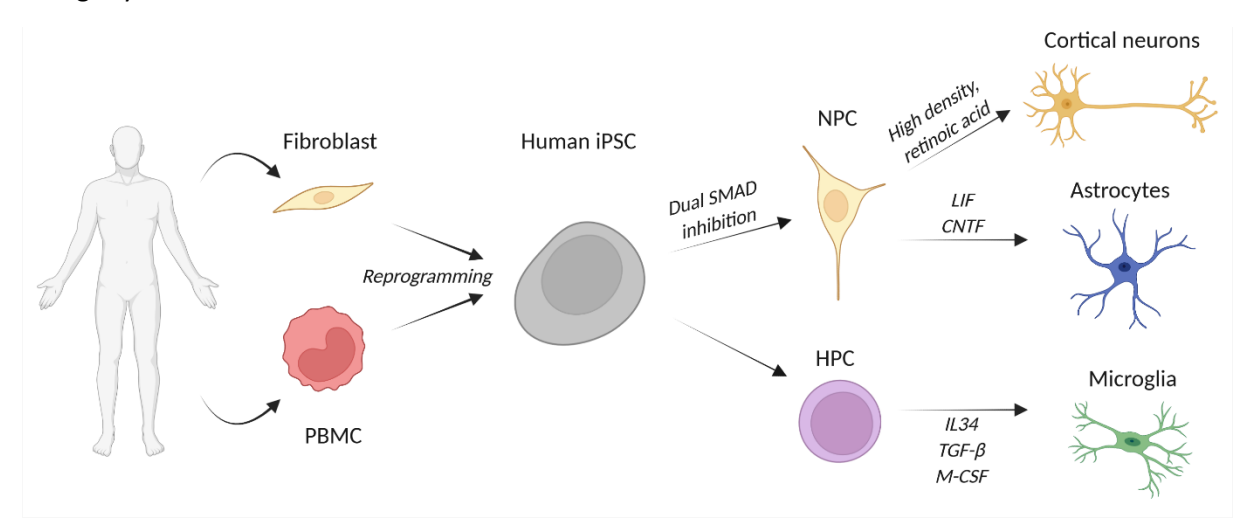


Figure 7: Generation of induced pluripotent stem cells (iPSCs) from human donors and differentiation into brain cell types. iPSCs are commonly derived from healthy donor fibroblasts or peripheral blood mononuclear cells (PBMCs) by reprogramming with specific transcription factors. As stem cells, iPSCs can then be differentiated into a variety of cell types, including cortical neurons and astrocytes via neural precursor cell (NPC) intermediates or microglia via hematopoietic precursor cell (HPC) intermediates. Differentiation can be induced by inhibition or activation of lineage-specific signaling pathways, such as dual-SMAD inhibition for neurons and astrocytes, addition of specific cytokines and growth factors such as retinoic acid for neurons, LIF and CNTF for astrocytes or IL34, TGF-β and M-CSF for microglia, or specific culture conditions such as high-density culture for neurons.

For astrocyte differentiation, initial dual-SMAD inhibition can be used as well, as both neurons and astrocytes arise from the same, neural lineage ¹⁵⁷. However, after NPCs arise, additional growth factors such as epidermal growth factor (EGF) and leukemia inhibitory factor (LIF) are added to promote cell proliferation and the gliogenic switch, turning NPCs into glia progenitor cells (GPCs) that are then differentiated into astrocytes by addition of trophic factors such as ciliary neurotrophic factor (CNTF) ^{158–161}. By avoiding serum exposure during the differentiation and maturation, the cells can be kept in a non-reactive state ¹⁶². The resulting astrocytes express typical markers such as glial fibrillary acidic protein (GFAP), S100beta, and excitatory amino acid transporter 1 (EAAT1), are functional as seen by promotion of neuronal survival, glutamate uptake and calcium imaging and can be activated by serum stimulation ¹⁵⁰. As for cortical neurons, the differentiation using small molecules is a protracted process of about 10 weeks and recently alternative protocols using overexpression of specific transcription factors have been published. In contrast to iN differentiation, the transcriptions factors are combinations of gliogenic factors such as nuclear factor 1a (NFIA) or 1b (NFIB) and/or Sox9 that are overexpressed in NPCs instead of iPSCs ^{163–166}. All published protocols using transcription factors yield astrocytes within 1-2 months that are functional and similar to primary astrocytes and astrocytes differentiated with small molecules on a transcriptomic level.

The differentiation of microglia from iPSCs follows a different protocol, as they arise from primitive macrophage precursors from the yolk sac 167,168 , not from ectoderm as neurons and astrocytes. Microglia differentiation protocols from iPSC follow two steps: First, iPSCs are differentiated into hematopoietic progenitor cells (HPCs) by activation of BMP and TGF- β signaling and hematopoietic

signaling pathways, similar to the macrophage precursors *in vivo*. These HPCs are then further specified into microglia-like cells by providing brain-like cues $^{151,169-172}$. One widely adopted protocol that was also applied here uses a commercially available kit for the first step followed by a defined medium with specific cytokines and growth factors - interleukin 34 (IL34), TGF β and macrophage-colony stimulating factor (M-CSF) - to promote microglia differentiation 173 . The resulting cells are similar to human primary microglia as seen by RNA sequencing, express typical markers such as Iba1, PU.1, P2RY12, TREM2, CD11b and are functional as seen by phagocytosis of human synaptosomes, wound scratch assays and cytokine secretion 151,152 . As for the other cell types, recently a protocol differentiating microglia using overexpression of transcription factors, namely PU.1 and CCAAT/enhancer-binding protein alpha (CEBPA), has been published 174 . The protocol yields functional cells that are similar to primary microglia on a transcriptomic level in 10 days compared to 24-40 days for previous protocols.

1.3.2. Approaches to increase physiological relevance of iPSC-derived in vitro models

All these cell types can be cultured in 2-dimensional (2D) monocultures on plastic dishes. However, this leads to artificial cell morphologies and aberrant cell-cell interactions due to the lack of other cell types normally present in the brain. Therefore, one way to create a more physiological environment is the combination of several brain cell types in co-cultures. It has been shown for example that co-cultures of iPSC-derived neurons and astrocytes display increased spontaneous and synchronized neuronal activity ¹⁷⁵ as well as synapse maturation ¹⁷⁶, and generally enhanced neuronal and synaptic network activity and maturity ¹⁷⁷. Co-cultures of iPSC-derived microglia with neurons increased expression of microglial markers as well as microglial ramification and motility ¹⁶⁹.

Another important factor to increase physiological relevance of iPSC-derived cultures is a 3dimensional (3D) culture format. A 3D environment promotes in-vivo-like cell-cell and cell-matrix interactions that are important for proper cell function and enables relevant studies on drug efficacy and toxicity ¹⁷⁸ and thus greatly increases translatability for studies of diseases affecting the brain such as AD. Over the past years, several approaches have been established to generate human 3D brain cell cultures (Figure 8). Currently, the most commonly used models are brain organoids. Brain organoids are formed by the aggregation of iPSCs into small spheres followed by their differentiation into the neural lineage. One approach to achieve this is undirected differentiation, taking advantage of the "default" pathway of stem-cell differentiation into forebrain lineages 179,180, and leading to the development or organoids with various brain region identities that can be used to study human cerebral development over time in vitro 181,182. Another approach is the directed differentiation by addition of lineage and patterning factors such as dual-SMAD inhibition, that yields organoids with specific brain region identities depending on the external cues provided 183,184, including cerebral cortex ¹⁸⁵ that is largely affected by AD pathology. As an alternative to organoids, NPCs instead of iPSCs can be aggregated into a 3D spheroid and differentiated into neuron-astrocyte co-cultures ^{186,187}. This approach increases reproducibility by removing the variable of initial iPSC differentiation efficiency, making them more suitable for drug screens. However, only culture periods of up to 2 months have been described, which may be too short for AD pathologies to arise. Another study combined inducible NPCs with iPSC-derived astrocytes into self-assembled 3D spheroids and completed neuronal differentiation during the cell aggregation step ¹⁸⁸. This approach yielded 3D neuron-astrocytes cocultures with a homogeneous distribution of both cell types and no neural rosette formation as seen in organoids. However, the cultures show a large variability in sizes and morphologies. This heterogeneity could be avoided by aggregating the cells in microwells, leading however to very small cultures sizes of $< 200 \mu m$ diameter and again no long-term culture of those spheroids was shown ¹⁸⁸. Finally, various studies used natural or synthetic hydrogels as a scaffold to embed iPSC-derived brain cell types and confirmed survival and maturation of the cells in the gel ^{189–192}. However, as the brain ECM has a very distinct composition ¹⁹³ that cannot yet be faithfully modelled *in vitro*, this yields an artificial environment for the cells which may not support physiological signaling and cell interactions.

Taken together, several approaches have been published to generate human 3D neural tissue models by cell aggregation or hydrogel embedding. However, the existing models do not provide a physiological tissue due to lack of brain cell types, experimental reproducibility, brain-like organization and/or long-term stability. Therefore, more work is needed to fully unfold the potential of iPSCs for brain tissue modeling and application of such models for AD research, as elaborated below.

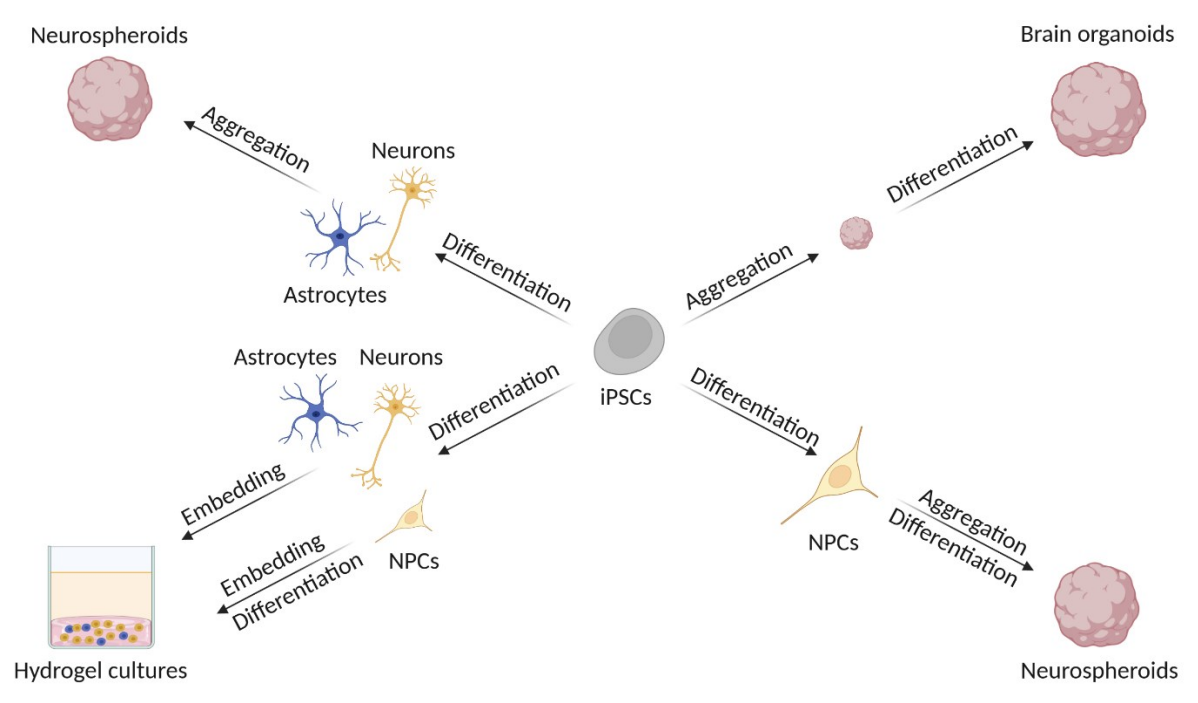


Figure 8: Approaches to generate human 3D brain cell cultures. Top right: 3D neural tissue is commonly generated by aggregating iPSCs followed by directed or undirected differentiation into brain or brain region organoids. Alternative approaches include (bottom right) differentiation of iPSCs into NPCs in 2D, followed by their aggregation and further differentiation into neurospheroids, or (bottom left) differentiation of iPSCs into NPCs or further into neurons and astrocytes, followed by their embedding into hydrogels as a 3D scaffold. **Top left:** Finally, iPSCs can be differentiated into neurons and astrocytes which are then aggregated to form neurospheroids.

1.4. iPSC-based modeling of Alzheimer's disease

1.4.1. iPSC-derived 2D AD models

The first iPSC-based AD models used cortical neurons derived from ADAD and sAD patients grown in 2-dimensional (2D) monoculture. They observed phenotypes such as altered A β secretion ¹⁹⁴, endoplasmic reticulum and oxidative stress ¹⁹⁵, enlarged endosomes ¹⁹⁶ and impaired endocytosis ¹⁹⁷, mitochondrial impairments ¹⁹⁸, increased phospho-Tau (pTau) levels ¹⁹⁶ as well as intracellular A β accumulation ¹⁹⁵. Other studies analyzed AD patient-derived astrocytes in 2D monoculture and found a less complex morphological appearance and abnormal localization of key astroglia markers ¹⁹⁹ as well as altered cytokine release, dysregulated Ca²⁺ homeostasis, increased oxidative stress and compromised neuronal supportive function in ADAD compared to isogenic control astrocytes ²⁰⁰. Lin et al. analyzed the effect of the strongest genetic risk factor for sporadic AD, ApoE4 ^{201,202}, on astrocytes and found dysregulated lipid metabolism, impaired A β uptake and cholesterol accumulation compared to isogenic ApoE3 astrocytes ²⁰³. The same group analyzed the effect of ApoE4 genotype on microglia and found altered morphologies and reduced phagocytosis of A β in ApoE4 microglia. Another study confirmed these results and found a general pro-inflammatory phenotype in ApoE4 microglia, but not in ADAD patient-derived microglia, possibly indicating a differential role of microglia in ADAD compared to sAD patients carrying ApoE4 alleles ²⁰⁴.

In general, these 2D monocultures of iPSC-derived brain cells are a simple, high-throughput approach to model AD *in vitro*. They can be manipulated rather easily, and show early, cell-autonomous disease phenotypes. However, these phenotypes could also be artefacts of the isolated, 2D culture conditions and the following lack of physiological signaling between the different cell types found in the brain. A recent study therefore established a 2D model system with iPSC-derived neurons, astrocytes, and microglia to improve on these drawbacks and establish a more physiological model with additional, disease-relevant brain cell types. The authors found strongly increased secretion of complement component 3 (C3) only in cultures containing all three cell types, that was further enhanced in AD versus control cultures, due to a reciprocal signaling between microglia and astrocytes ²⁰⁵. This example highlights the importance of incorporating additional cell types to enable more physiological cell interactions to increase the relevance of *in vitro* models and discover novel pathomechanisms.

However, although these 2D co-cultures are more physiological than monocultures, they still display artificial cell morphologies and lack cell-matrix and cell-cell interactions as well as spatial complexity. In addition, a 2D format likely prevents aggregation of endogenous proteins, for example into extracellular A β plaques, due to the lack of a 3D environment that would limit diffusion of the peptide into the media and the subsequent wash-out of produced A β at media changes ²⁰⁶. To avoid these drawbacks, 3D iPSC-based AD models have been developed.

1.4.2. iPSC-derived 3D AD models

The first iPSC-based 3D model was published in 2014 and used cortical neurons embedded in a synthetic hydrogel. The authors found altered levels of mechanotransduction- and cytoskeletonassociated proteins which cannot faithfully be studied in 2D, as well as altered responses to AB oligomer treatment in 3D vs. 2D cultures ¹⁹². Another study in the same year used a similar 3D hydrogel system but embedded immortalized human NPCs that strongly overexpressed APP and PSEN1 with a combination of AD causing mutations. The NPCs differentiated into neurons and the authors observed the formation of potentially plaque-like structures as well as Tau hyperphosphorylation and possible aggregation ²⁰⁷, making it the first description of AD-relevant protein aggregation in a human *in vitro* system. However, as described for mouse models, the strong overexpression may lead to artifactual phenotypes and impair the study of underlying pathomechanisms. In addition, in this study NPCs from the ventral midbrain were used, a region affected rather little and late by AD pathology 90,208, potentially limiting the relevance of the model to study disease processes that normally occur in the cerebral cortex. In 2016, Raja et al. pioneered the application of cortical organoids in AD research, implementing a more relevant and physiological model. Using different ADAD-patient-derived lines, the authors found increased secretion of $A\beta$ into the media, accumulation of the peptide within the cultures over time as well as increased pTau levels and endosomal abnormalities compared to wildtype organoids, but no advanced pathology such as plaques or tangles ²⁰⁹. Interestingly, another group analyzed whole-brain organoids made from iPSCs from one of the same patients and showed few isolated structures resembling plaques and tangles ²¹⁰. As the cells were derived from the same patient as in the first study, this discrepancy in phenotype formation cannot be due to variations in genetic background, but may rather be due to the applied organoid differentiation approaches, highlighting the need for standardized protocols. Another study compared a variety of healthy control and AD organoids, with each group containing ApoE3 and ApoE4 carriers. They found increased Aβ levels, but no insoluble A β , as well as increased pTau levels and potential synapse and neuron loss in AD organoids, with all disease phenotypes being enhanced in ApoE4 compared to ApoE3 carrier-derived lines ²¹¹.

All these studies show early disease phenotypes, but lack the formation of hallmarks such as widespread protein aggregation in plaques and tangles as well as neuroinflammation, the latter mainly

because of the lack of microglia in the models. In general, brain organoids have several limitations to study AD in vitro. First, due to the complex 3D arrangement of the cells during differentiation and subsequent heterogeneous access to patterning factors, there is a large variability in efficiency of organoid formation between cell lines and differences between organoids in size/morphology and cell type composition, especially in undirected and to a smaller extent in directed organoid protocols 182,212-²¹⁴. In addition, as models of brain development, organoids are built of proliferative neural rosettes with comparatively small brain parenchyma-like areas, and contain mainly neurons, with astrocytes arising only after around 2 months in culture at low percentages ¹⁸⁵ and not in every organoid ²¹⁴. Therefore, long culture periods of more than 6 months are necessary, until an adult ratio of neurons and astrocytes is achieved, while the organoid is growing in size ¹⁸⁵. This growth in turn leads to the formation of hypoxic areas and a necrotic core ^{215,216} due to a lack of oxygen and nutrient supply in the center of the cultures. This can be avoided by repetitive, acute slicing of organoids into sections ^{215,216}, however this is a very time-consuming process that requires special equipment and is therefore not feasible on a large scale. Together, while brain organoids are good models to unravel human-specific features of early brain development ^{217,218}, all the above-mentioned factors limit their applicability for systematic studies of AD pathomechanisms and especially drug screening approaches.

1.4.3. Chimeric iPSC-based AD models

To avoid some of these caveats and provide a brain-like environment with increased cellular diversity that supports physiological cell interactions, human iPSC-derived brain cells have recently been transplanted into mouse brains. Xenografting of stem-cell-derived, wildtype NPCs into neonatal, transgenic AD mouse brains led to differentiation into cortical neurons followed by plaque formation also within the human graft and subsequent tauopathy phenotypes including Tau hyperphosphorylation and misfolding, but not tangle formation ¹²³. In addition, the authors observed specific loss of human but not mouse neurons in response to the pathology. The results have been replicated in a recent preprint using the NL-G-F mouse model, again showing tau misfolding and aggregation specifically within human neurons as well as their degeneration by necroptosis 219. Together, this highlights the importance of analyzing human neurons in an AD context and brain-like environment. Transplantation of astrocyte progenitor cells into a transgenic AD mouse model led to the differentiation into different astrocyte subtypes, their functional integration into the mouse brain and morphological changes in response to amyloid plaques ²²⁰. Finally, a variety of studies investigated the response of xenografted microglia on AD pathology 126,221,222. They confirmed a widespread engraftment of transplanted HPCs over most of the mouse cortex, the maturation into homeostatic microglia in the brain environment and tiling of the tissue. Human stem-cell-derived microglia transplanted into AD mice clustered around Aβ plaques, showed accumulation of lipid droplets ²²², and partially human-specific, transcriptomic changes not seen in DAMs in mice 221, that all depend on TREM2 function. Similar transcriptomic changes were seen by another group upon injection of oligomeric Aβ into wildtype mouse brains with human MG xenografts ¹²⁶.

One disadvantage of such transplantation experiments is the incompatibility with drug screens due to the low throughput. In addition, the human cells are xenografted into a non-human environment which may lead to unphysiological cell interactions and thus impair the analysis of human-specific disease mechanisms. Finally, immunodeficient mice have been used for the experiments, to avoid host immune reactions against the transplanted cells. This reduces the advantage of the *in vivo* system regarding increased cell type diversity and prohibits studies on peripheral immune responses to AD pathology, which may play important roles in pathogenesis ²²³. Although a recent study showed that transplanted microglia can survive in immunocompetent mice, the approach did not lead to colonization of the mouse cortex ²²⁴, the area most affected by plaque pathology and degeneration in humans.

In summary, a variety of iPSC-based AD models has been published, from 2D over 3D to xenografted models, and contributed to our understanding of pathological processes and underlying mechanisms. However, most current *in vitro* models lack advanced AD hallmarks such as widespread aggregation of endogenous proteins. This may be due to the common use of patient-derived lines with mutations that in humans cause typical pathology only after decades. Therefore, a solution to induce advanced pathology within experimentally trackable time frames while avoiding overexpression artefacts could be to combine synergistic, AD-causing mutations as in the NL-G-F mouse model ¹⁰⁰. This requires easy and versatile genomic access to introduce the desired alterations, e.g., to knock in disease-causing mutations, which has been enabled by the discovery and development of CRISPR/Cas genome editing systems.

1.5. CRISPR/Cas genome editing

The CRISPR/Cas (Clustered regularly interspaced short palindromic repeats/CRISPR associated protein) genome editing system is originally a bacterial and archaeal adaptive immune system against viruses ^{225,226}, but has quickly been adopted and optimized for precise and efficient genome engineering in human cells ^{227,228}. The optimized system consists of the Cas nuclease and an engineered single guide RNA (sgRNA), that guides the nuclease to the desired target locus by complementary base pairing ^{229,230} upstream of a specific motif (protospacer adjacent motif - PAM) ²³¹ (Figure 9). The system can be delivered via plasmids that encode sgRNA and Cas protein ^{227,228}, or via RNPs ²³², in which recombinant Cas9 protein is complexed with a synthetic sgRNA in vitro. When the Cas9-sgRNA complex reaches and binds the target locus, a double-strand break is introduced that can be repaired by non-homologous end joining (NHEJ) or by homology-directed repair ^{227,228}. NHEJ is an error-prone pathway that directly fuses the two DNA strand ends together, commonly resulting in small insertions or deletions (InDels) at or around the cut site ²³³. These InDels can cause frameshift mutations, leading to premature stop codons and can thus be used to knock out protein-coding genes. Homology-directed repair in turn can be used for precise gene editing including knock-ins by providing a synthetic repair template that carries the desired changes, such as AD-causing mutations 154, and is inserted into the cells genome during the repair process ^{227,228}. Although other technologies such as zinc-finger nucleases and transcription activator-like effector nucleases (TALENs) enabled precise gene editing before ²³⁴, these rely on engineered proteins to achieve binding to a specific DNA sequence. As RNAs are much easier and cheaper to synthesize than proteins, the CRISPR/Cas systems revolutionized biomedical research by providing quick and easy genomic access also for non-specialized labs.

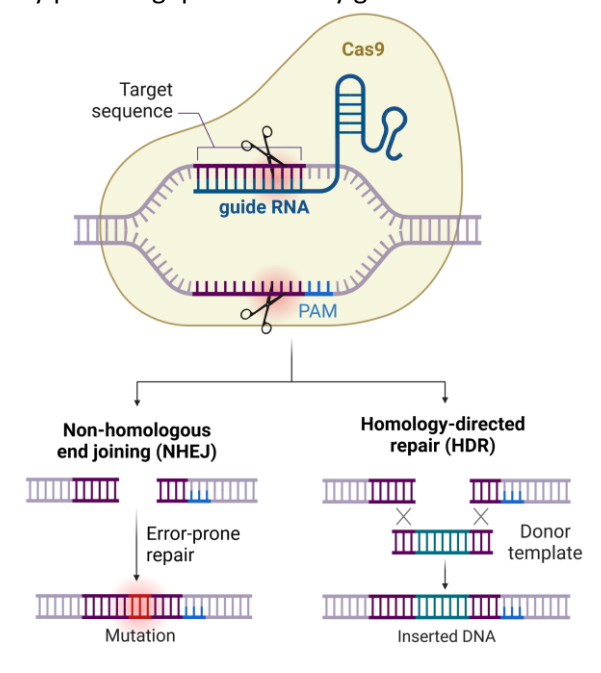


Figure 9: Working principle of the CRISPR/Cas9 gene editing system. The Cas9/single guide RNA complex binds to the targeted locus by complementary base pairing of the guide RNA with the target sequence, directly upstream of the protospacer adjacent motif (PAM). The Cas9 enzyme then introduces a double-strand break (DSB) 3 base pairs upstream of the PAM sequence (indicated by scissors). The DSB can then be repaired by 1) non-homologous end joining, an error-prone pathway that religates the free DNA ends, frequently introducing unspecific insertions or deletions around the cut site, or 2) homology-directed repair, which uses a partially homologous donor template to repair the DSB and can be exploited to introduce specific edits such as insertions or knock-ins by supplying a template carrying the desired changes.

1.5.1. CRISPR/Cas-based disease modelling

The combination of CRISPR/Cas genome editing and hiPSC technology yields especially useful tools as it enables 1) analyzing effects of risk variants and disease-causing mutations in the disease-relevant, human cell types and 2) the generation of isogenic cell lines, allowing for a direct comparison of cells that only differ by the variant of interest. Isogenic cell lines can be generated either by correcting the mutation in a patient-derived cell line, or by inserting the mutation into a healthy donor line. The first has the advantage that the whole genetic background is included, which may carry disease-modifying risk variants and thus influence pathogenesis. The latter has the advantage that healthy donor lines are more readily available and that several, possibly synergistic mutations can be used to accelerate naturally occurring pathology formation. In addition, mutation insertions can be done in wellcharacterized iPSC lines that are known to differentiate into the cell types of interest ¹⁵⁴. These lines can then also be used to compare the effect of different mutations in an isogenic background ²³⁵. As mentioned above, this is an important factor when modelling neurodegenerative diseases that commonly affect elderly or adults and thus have protracted disease courses that are too long to fully recapitulate in a model system. Alternatively, more mutations can also be knocked into patient-derived lines to combine both approaches. In addition to mutation knock-ins, CRISPR/Cas genome editing enables the investigation of the pathogenic effect of risk variants such as ApoE4 or more rare variants, by knock-out of the respective gene or knock-in of a known variant.

In summary, CRISPR/Cas genome editing strongly advanced biomedical research as it allows introducing almost any desired genomic edit into cells of interest and analyzing its effect for example in pathogenesis.

1.6. Hypothesis and aims of the thesis

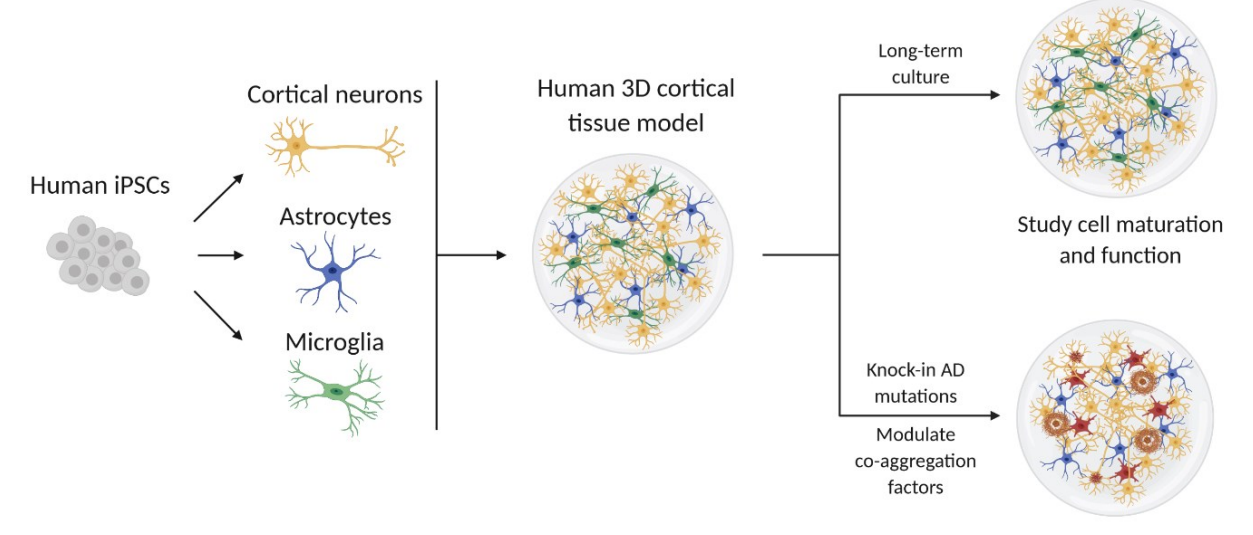
Based on the current research, the central hypothesis of this thesis is that human-specific disease mechanisms contribute to the formation of complete AD pathology. Consequently, it requires human brain cells in a 3D, brain-tissue-like environment to generate the full pathology and discover potentially human-specific disease mechanisms and thus novel therapeutic targets.

Current human iPSC-derived 3D models such as organoids have several limitations including high variability and low phenotype penetrance due to the heterogeneous cell composition, presence of proliferative areas, lack of physiological numbers of glia cells, and formation of a necrotic core. Therefore, the main objectives of this thesis were 1) the generation and characterization of a more physiological, controllable, and reproducible human cortical tissue model and 2) the analysis of its potential for modelling Alzheimer's disease *in vitro* (Figure 10).

To establish the model, I first aimed to adopt and optimize protocols to differentiate human iPSCs into highly pure cultures of cortical neurons, astrocytes, and microglia. Using these differentiated, human brain cell types I then focused on establishing modular 3D co-cultures to create reproducible and controllable cortical brain tissue models (3BTMs), and characterize the cultures over time to analyze cell maturation and functionality.

To analyze the model's potential for modelling AD, I then aimed to induce $A\beta$ accumulation in 3BTMs by knock-in of three synergistic, AD-causing APP mutations to accelerate naturally occurring disease processes. I would then analyze emerging phenotypes and underlying mechanisms, and finally investigate additional disease-modulating factors to trigger the formation of advanced disease hallmarks such as protein aggregation in $A\beta$ plaques. These factors include prolonged culture periods, genetic alterations in AD risk genes such as TREM2, presence or absence of non-neuronal cell types

such as microglia and astrocytes, seeding approaches with mouse brain lysate or recombinant human $A\beta42$, as well as the 3D environment that promotes retention and seeding of aggregating proteins.



Analyze AD phenotypes and pathomechanisms

Figure 10: Overview of the project. The first objective of this thesis was the generation and characterization of a controllable and reproducible, human 3D cortical tissue model. To generate this model, I aimed to differentiate human iPSCs into AD-relevant cell types such as cortical neurons, astrocytes, and microglia (left). These differentiated brain cell types are then combined to generate modular 3D cortical tissue models (middle), that are analyzed regarding cell maturation and function over time (top right). The second objective was to use the cultures for modelling AD *in vitro*. To this end, I aimed to knock in AD-causing mutations and modulate co-aggregation factors and analyze emerging AD phenotypes and underlying pathomechanisms.

2. Materials and Methods

2.1. iPSC lines

iPSC experiments were performed in accordance with all relevant guidelines and regulations. Wildtype iPSC-lines used in this study were: 7889SA2 (short SA2), a single cell clone derived from the male 7889SA line described by Paquet et al. ¹⁵⁴, as well as the commercial, female iPSC line A18944 (Thermo Fisher #A18945). Cell line 7889SA2-P4F8 (short P4F8) was derived from line SA2 by introduction of the APP Swedish mutation as described by Paquet et al. ¹⁵⁴.

2.2. iPSC maintenance

iPSCs were maintained on vitronectin (VTN)-coated (Thermo Fisher #A14700) 6-well plates (Corning #353046) in Essential 8 Flex medium (E8F, Thermo Fisher #A2858501). For VTN coating, the stock solution was diluted 1:100 in Dulbecco's phosphate buffered saline (PBS) without Calcium/Magnesium (Sigma-Aldrich #D8537). 1 ml of stock solution was added per 6-well well and incubated for one hour at room temperature (RT). Cells were kept as colonies and split every 3-4 days. For splitting, cells were washed once with PBS, and then incubated for 5 minutes at RT in PBS with 0.5 mM UltraPure EDTA (Thermo Fisher #15575020). PBS/EDTA was aspirated and 3 ml of DMEM/F-12 (Thermo Fisher #11320074) were added to wash the colonies off the plate. The cell solution was triturated to achieve homogenous colony sizes and then transferred to the new plate.

To freeze iPSCs, cells were detached as described above and washed off with cold freezing medium made of 45% E8F, 45% fetal bovine serum (FBS, Thermo Fisher #10500064), 10% DMSO (Sigma-Aldrich #D2650) and 10 μ M rock inhibitor Y27632 (RI, Selleckchem #S1049). The cell suspension was transferred into cryovials, stored at -80 °C for 24 hours and subsequently at -140 °C. To thaw iPSCs, the cell suspension was shortly incubated in a 37 °C water bath until almost thawed, then transferred into a 15 ml conical tube (VWR #525-0061) containing 9 ml of DMEM/F-12, and spun at 1000 rpm (162 g) for 4 min. The supernatant was aspirated, cells were resuspended in 2 ml E8F medium with 10 μ M RI and plated onto VTN-coated 6-well wells.

2.3. CRISPR/Cas9 gene editing design

SgRNAs were designed using the CRISPOR online tool (http://crispor.tefor.net/) ²³⁶. SgRNA sequences were cloned into the BsmBI restriction site of plasmid MLM3636 (a gift from K. Joung, Addgene 43860). CRISPR editing was performed as described by Paquet et al. ¹⁵⁴ using Cas9 plasmid pSpCas9(BB)-2A-Puro (PX459) V2.0 (a gift from F. Zhang, Addgene 62988). Single-stranded oligodeoxynucleotides (ssODNs) were used as repair oligos and designed manually. SsODNs were purchased from IDT. Sequences of used sgRNAs and ssODNs can be found in Table 1.

Table 1: Sequences of sgRNAs and ssODNs

adde 1. Sequences of Spirits and SSOPIES				
Locus	Sequence (5'-3')			
sgRNAs				
APP ^{lbe} GACAGTGATCGTCATCACCT <u>TGG</u> APP ^{Arc} GGTGTTCTTTGCAGAAGATG <u>TGG</u>				
		ssODNs		
APP ^{lbe}	GTCAAGTTTACCTACCTCCACCACACCATGATGAATGGATGTGTACTGTTTCTT CTTCAGCATCA <u>CTA</u> AG GT GATGACGA <mark>A</mark> CACTGTCGCTATGACAACACCGCCCA			
APP ^{Arc}	GACGAACACTGTCGCTATGACAACACCGCCCACCATGAGTCCAATGATTGCAC CTTTGTTTGAAC <u>CGA</u> CG TC TCCTGCAAAGAACAACCTTGAAAACAAATTAAGAAA			
bold = cut site, red = intended mutation, blue = CRISPR/Cas-blocking mutation, underlined = NGG				

2.4. sgRNA Testing in HEK293 cells

To test sgRNA efficiency, sgRNA and Cas9 plasmids were transfected into HEK293 cells. Per transfection, 2.4 μl X-tremeGENE™ 9 DNA Transfection Reagent (Sigma-Aldrich #6365779001) were diluted in 100 μl DMEM (Thermo Fisher #31966021) and incubated at RT for 5 minutes. In the meantime, for each transfection Cas9 and sgRNA plasmids were mixed in a separate tube in a 2:1 ratio with 0.8 μg Cas9 plasmid and 0.4 μg sgRNA plasmid. 100 μl of the X9/DMEM solution were added to each plasmid solution and incubated for 20 minutes at RT. Following the incubation, 100 μl of the solution was added to each 12-well well of HEK293 cells. Two days following transfection, a cell pellet from the transfected HEK293 cells was collected and gDNA was isolated using the NucleoSpin Tissue Kit (Macherey-Nagel #740952.250, always used for gDNA extraction if not indicated otherwise), according to the manufacturer's instructions. PCR amplification around the target loci followed by Sanger sequencing was performed and editing efficiency was calculated using the TIDE online tool (https://tide.nki.nl/) ²³⁷.

2.5. iPSC Electroporation

Two days before electroporation, 6-well plates were coated with Geltrex (GT, Thermo Fisher #A1413302) diluted 1:150 in DMEM/F12 at 37° for at least 1 hour. To prepare cells for electroporation, iPSC colonies were detached using Accutase (Thermo Fisher #A1110501) for 5 min at 37 °C. Accutase was stopped by addition of DMEM/F12 with 10 μ M RI and cells were triturated to single cells, spun down at 160 g and plated at 250.000 cells/well onto the GT-coated 6-well plates in StemFlex media (SF, Gibco # A3349301) with 10 μ M RI. On the day of electroporation, a 10 cm dish (Thermo Fisher #150350) was coated with GT for each reaction. The iPSCs were detached using Accutase as described above, triturated to single cells, mixed 1:1 with Trypan Blue (Sigma-Aldrich #T8154) and counted manually using a Neubauer chamber (Wagner & Munz GmbH #717805). After centrifugation, iPSCs were resuspended at 20 Mio. cells/ml in 100 μ l electroporation solution (see Table 2).

Table 2: Composition of the electroporation solution

Component	amount
Cas9 plasmid	30 µg
sgRNA plasmid	5 μg
ssODN	30 µg
BTXpress™ High Performance Electroporation Solution (VWR #732-1285)	To 90 μl

The cell suspension was added to a 1 mm cuvette (Fisher Scientific #15437270) and placed inside a safety dome (BTX #45-2021) of the BTX Gemini X2 electroporation system (#45-2006). Electroporation was performed with 2 pulses of 65V for 20 ms each with 10 ms interval. Immediately after electroporation, the cell suspension was transferred to the GT-coated 10 cm dish in SF media with Revitacell (RVC) supplement (1:100, Thermo Fisher #A2644501).

2.6. Puromycin selection and clonal expansion of electroporated iPSCs

On days 1-3 after electroporation, cells were fed with fresh SF + RVC media supplemented with puromycin (VWR, #J593-25MG) at a final concentration of 350 ng/ml to select transfected cells. From day 4 on, cells were fed with SF + RVC media. Once small colonies formed, media was switched to SF only. After 7-8 days, each clonal colony was manually detached and transferred into a single well of a GT-coated 96-well plate (Corning # 5380522) in SF media with 10 μ M RI. Single cell clones were fed with SF as needed until almost confluent.

2.7. Analysis of single cell clones

2.7.1. Replica Split and Crude Lysate preparation

To extract gDNA for the restriction fragment length polymorphism (RFLP) analysis, each single cell clone was split into a new, GT-coated 96-well well. To this end, cells were incubated with 40 μ l Accutase for 10 min at 37 °C and subsequently washed off the plate by addition of 100 μ l SF with 10 μ M RI. 20-30 μ l of the cell suspension was transferred into the same position of the new 96-well plate containing 100 μ l SF media with 10 μ M RI. The remaining cell suspension was spun down for 12 min at 2500 g and the cell pellets were prepared for gDNA extraction by addition of 25 μ l lysis buffer (Table 3) and incubation for 10 min at RT on a rotational shaker at 150 rpm. Cells were washed off the plate and the resulting suspension was transferred to a 96-well PCR plate (Brand #781374) and incubated at 55 °C for 4 hours for complete lysis, followed by 10 min at 95 °C to inactivate Proteinase K.

Table 3: Composition of lysis buffer and 10x jumpstart buffer stock

Lysis Buffer	For 1 plate [μl]
Proteinase K (NEB #P8107S)	41.25
10x Jumpstart Buffer	275
Ultrapure H ₂ O (Thermo Fisher #10977035)	2431
10x Jumpstart Buffer stock	[ml]
1M Tris pH8.3 (Carl Roth #0188.3)	3
1M KCl (AppliChem #A3582)	15
1M MgCl ₂ (Carl Roth # KK36.1)	0.45
0.1% Gelatin (Sigma-Aldrich #ES006B)	3
MilliQ H ₂ O	8.55

2.7.2. Genotyping PCR

Following cell lysis, the genomic region surrounding the targeted locus was amplified by PCR. For each clone, 10 μ l of Taq PCR master mix (Table 4) and 2.5 μ l of lysate were pipetted into one well of a new 96-well PCR plate and the PCR was run according to Table 5 using primers OL1208/OL1212 (Table 18).

Table 4: Composition of Taq PCR Master Mix

Taq PCR Master Mix	1 plate (110x) [µl]
Primer 1 (100 μM)	2.75
Primer 2 (100 μM)	2.75
OneTaq® Quick-Load® 2X Master Mix (NEB #M0482L)	687.5
Ultrapure H ₂ O	407

Table 5: Taq Polymerase PCR program

Step	Temp [°C]	Time [mm:ss]	Cycles
Initial Denaturation	95	02:00	1
Denaturation	95	00:30	
Annealing	60	00:30	35
Extension	68	00:30	
Final Extension	68	02:00	1
Hold	10	∞	1

2.7.3. Restriction enzyme digest and expansion and banking of positive clones

To identify edited clones, the PCR-amplified region was digested with a specific restriction enzyme to screen for the gain of a restriction site introduced by HDR editing. 5 μ l of digestion master mix (Table 6) and 5 μ l of PCR product of each clone were incubated for 3 h at the enzyme-specific temperature (Table 7) and cleavage products were separated on a 2 % agarose (Serva, #11406.02) gel. Positive clones were sent for Sanger sequencing at GATC/Eurofins.

Table 6: Composition of Digestion Master Mix

Digestion Master Mix	1 plate (110x) [µl]
CutSmart buffer (NEB #B7204S)	110
Restriction Enzyme (Table 5)	13.75
Ultrapure H ₂ O	426.25

Table 7: Restriction Enzymes for RFLP Clone Screening

Editing Locus	ting Locus Restriction Enzyme Incubation Gain/Loss		Gain/Loss	Cleavage Products	
Editing Locus	Restriction Enzyme	ilicubation	Gaill/LUSS	Edited	Unedited
APPlbe	Ddel (NEB #R0175S)	3 h, 37 °C	Gain	248, 175	423
APP ^{Arc}	HpyCH4IV (NEB #R0619S)	3 h, 37 °C	Gain	163, 260	423

Successfully edited clones were expanded to 6-well plates, and cleaned from differentiated cells before cell banking. Before the single cell clones were frozen as described above, approximately 50 % of a confluent 6-well well was used for gDNA extraction with the NucleoSpin Tissue Kit according to manufacturer's instructions for following quality controls.

2.8. Quality controls of edited iPSCs

2.8.1. Fingerprinting PCR

To verify the origin of each edited cell line, a microvariation at the human D1S80 locus was analyzed by fingerprinting PCR. For each cell line, $20\,\mu l$ of Taq Master Mix (Table 4) and primers OL1240/OL1241 (Table 18) were combined with 50 ng gDNA. A PCR was run as in Table 5, but with 70°C annealing temperature and 60 sec extension time. PCR products were separated on a 2% agarose gel and the band pattern compared to the parent cell line.

2.8.2. qgPCR Assays to verify allele number at edited locus and BCL2L1 gene locus

For each edited cell line, the number of alleles at the edited locus was estimated by using a qPCR in comparison to the parental cell line as described by Weisheit et al. 238 . To this end, 7.5 μ l 2x PrimeTime Gene Expression Master Mix (IDT #1055772) were mixed with 0.75 μ l 20x human TERT TaqMan Copy Number Reference Assay (Thermo Fisher #4403316) as internal control, 0.75 μ l 20x target qgPCR assay containing the genotyping primers (0.5 pmol/ μ l) and PrimeTime Eco Probe (0.25 pmol/ μ l, HPLC-purified, IDT) according to Table 8 and 3 μ l of DNase-free H₂O per sample.

Per edited line, $25.4~\mu$ l of this master mix was mixed with $6.54~\mu$ l gDNA dilution (prepared at $10~ng/\mu$ l). From this mix, $15~\mu$ l were pipetted in duplicate into a 96-well qPCR plate (VRW #732-2934). QgPCR was run on a StepOne Plus Real-Time PCR system (Thermo Fisher #4376600) according to Table 9. Resulting Ct values were normalized to internal TERT reference and a karyotypically normal control sample to calculate allele copy numbers.

The procedure was repeated to exclude triplications at the BCL2L1 locus, a common chromosomal aberration that gives a growth advantage to iPSCs. For primers and probe see Table 18 and Table 8, respectively.

Table 8: QgPCR primers and probes (for primer sequences see Table 18).

Locus	Primers	Probe Sequence 5'-3'
APP Exon 17	OL1209/OL1212	56-FAM/CCTCCACCA/ZEN/CACCATGATGAATGGA/3IABkFQ
BCL2L1	BCL2L1_F/BCL2L1_R	56-FAM/TGTGGAAGA/ZEN/GAACAGGACTGAGGC/3IABkFQ

Table 9: QgPCR program

Step	Temp [°C]	Time [mm:ss]	Cycles	
Polymerase activation	95	05:00	1	
Denaturation	95	00:15	40	
Annealing/extension	60	01:00	40	
Hold	10	∞	1	

2.8.3. Off-target analysis

For each sgRNA, potential off-target (OT) editing sites were predicted by CRISPOR online tool (http://crispor.tefor.net/). Edited cell lines were then tested to exclude alterations at the top five off-target loci. A 50 μ l PCR was performed to amplify each off-target locus using primer combinations as in Table 10 and the PCR program as in Table 5. Off-target editing was then excluded by Sanger sequencing.

Table 10: Primers used for top five off-target editing sites for each mutation (primer sequences see Table 18).

ОТ	APP ^{Arc}	APPlbe
1	OL1512/OL1513	OL1522/OL1523
2	OL1546/OL1547	OL1524/OL1525
3	OL1516/OL1517	OL1526/OL1527
4	OL1518/OL1519	OL1528/OL1529
5	OL1520/OL1521	OL1530/OL1531

2.8.4. Clonality check

To confirm clonality, each edited line was split into single cells using Accutase and plated as single cells on 10 cm dishes. At least 30 clones were picked into 96-well plates and screened using RFLP assay as in 2.7..

2.8.5. Pluripotency stainings of iPSCs

To confirm pluripotency in edited cell lines, expression of common pluripotency factors Oct4, Tra160, SSEA4 and Nanog was analyzed by immunofluorescence staining (see Table 14 for antibodies). To this end, iPSCs were split with EDTA as in 2.2 on acid-etched coverslips (VWR # 630-2190) coated with VTN. For acid-etching, coverslips were incubated in 30 % hydrochloric acid (Carl Roth # X896.2) over night at RT on an orbital shaker. Coverslips were then washed 3x 10 min in ddH $_2$ O and stored in 100 % ethanol (VWR # 20.821.310). iPSC colonies were fixed 2-3 days after the split using 4 % PFA (Morphisto #1.176.201.000) for 10 min at RT and stained as described in 2.14..

2.8.6. Molecular Karyotyping

To exclude large chromosomal aberrations on a global scale, 15 μ l (50-100 ng/ μ l) of fresh gDNA from each edited line were sent to HelmholtzZentrum München for molecular karyotyping analysis.

2.9. Cortical neuron differentiation from iPSCs

Cortical neuron differentiation was performed using a custom protocol based on dual-SMAD inhibition as described before ¹⁵⁴. iPSCs were split into single cells using Accutase as in 2.5., resuspended in 2/3

of Essential 6 media (E6, Table 11) mixed with 1/3 neural induction medium (NI, Table 11) and supplemented with 10 μ M RI and 5 μ M XAV939 (a WNT inhibitor that has been shown to promote cortical forebrain neuron differentiation ¹⁴⁸), and plated on GT-coated 12-well plates at 1 million cells per well (= day in vitro 0 (DIV0)). On DIV1, media was changed to 1/3 E6 + 2/3 NI supplemented with 5 μΜ XAV939. On DIV2, media was changed to NI. On DIV6/7, cells were split into high-density spots on dried 6-well plates coated 4 hours with poly-L-ornithine (pO, Sigma-Aldrich #P4957, diluted 1:100 in ddH2O) and overnight with laminin (L, Thermo Fisher #23017015, diluted 1:100 in PBS). Before cell dissociation, the laminin solution was aspirated, and the plates were left open to dry in a laminar flow hood. Cells were split with Accutase for 10 min and resuspended in NI supplemented with 10 μ M RI (NI/RI) at 30 million cells per ml. 250-350 μl of the cell suspension were slowly added to each well to form spots. After one hour, 2 ml NI/RI were carefully added to each well. On DIV10, medium was changed to neural maintenance medium (NM, Table 11) supplemented with 20 ng/ml bFGF (Stemcell Technologies #78003.2) (NM/bFGF) for two days. Cells were then maintained in NM until neural rosettes formed and piled up (around DIV20-23). At this point, cells were incubated in 1 ml StemDiff™ Neural Rosette Selection Reagent (NRSR, STEMCELL Technologies #5832) for 60-90 min at 37 °C. Rosettes from the center of the spot were then manually isolated using a pipette tip, spun down, carefully resuspended in NM/bFGF to keep rosettes intact, and plated on pOL-coated 6-well plates. Cells were fed with NM/bFGF for 1-2 days and then kept in NM until rosettes became confluent (DIV28-31). On this day, rosettes were carefully dissociated from each other with Accutase for 4 min and the rosettes were plated on pOL-coated 6-well plates in NM/bFGF. Again cells were fed with NM/bFGF for 1-2 more days, then maintained in NM until DIV35-38 and then frozen. To this end, rosettes were split with Accutase for 4min, resuspended in cold neuron freezing medium (NM with 10% DMSO and 20 ng ml⁻¹ bFGF), transferred to -80 °C and after 24 hours to liquid N2 for long-term storage.

Thawing of rosettes was performed as described for the iPSCs, but rosettes were transferred into Neurobasal medium instead of DMEM/F-12. One vial of rosettes was plated on one pOL-coated 6-well well in 2 ml NM/bFGF. Cells were fed with NM/bFGF again for two days after thawing, then with NM as needed until they were split for 2D or 3D cultures.

Table 11: Composition of media for cortical neuron differentiation and maturation

Essential 6 Medium (E6)	[ml]
DMEM/F-12 (Thermo Fisher #11320-074)	482
L-ascorbic-acid-2-phosphate (Sigma-Aldrich #A8960, dissolved to 64 mg/ml in H ₂ O)	0.5
Insulin-Transferrin-Selenium (ITS -G, 100X) (Thermo Fisher #41400045)	9.7
HEPES (Sigma-Aldrich #H3375, dissolved to 1 M in H ₂ O)	7.5
Neural Maintenance Medium (NM)	[ml]
Neurobasal (Thermo Fisher #21103-049)	235
DMEM/F-12 (Thermo Fisher #11320-074)	235
Penicillin-streptomycin (Thermo Fisher #15140-122)	5
B27 supplement with Vit. A (Thermo Fisher #17504044)	5
GlutaMAX (Thermo Fisher #35050)	5
NEAA (Thermo Fisher #11140-050)	5
N-2 supplement (Thermo Fisher #17502048)	2.5
Insulin (500 µg/ml) (Sigma-Aldrich #10516)	2.5
2-Mercapto-ethanol (Thermo Fisher #21985-023)	0.45
Neural Induction Medium (NI)	[ml]
NM	100
SB-431542 (Selleckchem #S1067)	10 µM
LDN-193189 (Selleckchem #S2618)	0.25 μM

NB+/B27+	[ml]
Neurobasal Plus (Thermo Fisher #A3582901)	485
Penicillin-streptomycin (Thermo Fisher #15140-122)	5
B27PLUS (Thermo Fisher #A3582801)	10
GlutaMAX (Thermo Fisher #35050)	1.25

Table 12: Composition of media for astrocyte differentiation

Glial Precursor Expansion Medium (GEM)	[ml]		
DMEM/F-12 (Thermo Fisher #11320-074)	475		
Penicillin-streptomycin (Thermo Fisher #15140-122)	5		
B27 supplement without Vitamin A (Thermo Fisher #12587-010)	10		
GlutaMAX (Thermo Fisher #35050)	5		
N-2 supplement (Thermo Fisher #17502048)	5		
bFGF (StemCell Technologies #78003.2)	10 ng/ml		
EGF (Peprotech #100-15)	10 ng/ml		
Astrocyte Induction Medium (AIM)	[ml]		
DMEM/F-12 (Thermo Fisher #11320-074)	475		
Penicillin-streptomycin (Thermo Fisher #15140-122)	5		
B27 supplement without Vitamin A (50x, Thermo Fisher #12587-010)	10		
GlutaMAX (Thermo Fisher #35050)	5		
N-2 supplement (100x) (Thermo Fisher #17502048)	5		
LIF (Peprotech #300-05)	10 ng/ml		
EGF (Peprotech #100-15-100)	10 ng/ml		
Astrocyte Medium (AM)	[ml]		
DMEM/F-12 (Thermo Fisher #11320-074)	480		
Penicillin-streptomycin (Thermo Fisher #15140-122)	5		
B27 supplement without Vitamin A (50x, Thermo Fisher #12587-010)	10		
GlutaMAX (Thermo Fisher #35050)	5		

2.10. Astrocyte differentiation from iPSCs

Initially, differentiation of iPSCs to astrocytes was performed following the protocol by TCW et al. with minor modifications. iPSCs were differentiated as in the cortical neuron differentiation protocol up to DIV23-26, 3 days after the NRSR split. On this day, rosettes were split using Accutase and plated into GT-coated 6-well wells at 70.000 cells/ml in NM/bFGF. The next day, media was changed to commercially available astrocyte medium (ScienCell #SC-1801) with all supplements. Cells were fed every 2-3 days as needed, and split again with Accutase to 70.000 cells/ml when reaching confluency. After 30 days in astrocyte medium, cells were used for experiments or frozen in 70% astrocyte medium with 20% FBS, and 10% DMSO. As the protocol uses serum exposure, which activates the cells, and cells did not survive in the medium used for co-cultures with neurons, another protocol was established and optimized for the majority of experiments (Figures 12-19). 161. iPSCs were differentiated as in the cortical neuron differentiation protocol up to DIV14-15 when rosettes were first visible. Media was then changed to glial precursor expansion medium (GEM, Table 12) and exchanged every day. 3 days later, rosettes were split using NRSR as described in 2.9. into pOL-coated 6-well wells in GEM. When reaching confluency, rosettes were split using Accutase and plated into GTcoated 6-well wells at 1 million cells/ml. Media was exchanged again every day and cells were split using Accutase when confluent. After 14-21 days, media was changed to astrocyte induction medium (AIM, Table 12) to induce neural to glial precursor cell transition. From this point on, when confluent, cells were split using Accutase and plated in GT-coated 6-well plates at 0.5 million cells/ml. After 14 days, media was changed to astrocyte medium (AM, Table 12) supplemented with 20 ng/ml CNTF

(Peprotech #450-13) to induce astrocyte differentiation and maturation. Cells were fed with AM+CNTF and splitted as needed for 28 days, then media was changed to AM. Cells can be frozen at any step of the protocol in the respective medium supplemented with 10 % DMSO.

Thawing of astrocytes was performed as described for iPSCs, but after centrifugation cells were resuspended in AM, plated onto GT-coated 6-well plates, and fed with AM until they were split for 2D or 3D cultures.

2.11. Microglia differentiation from iPSCs

Differentiation of iPSCs to microglia was performed following the protocol by McQuade et al. 152 with minor modifications 239 . iPSCs were split with PBS+EDTA as described in 2.2 when 70-80 % confluent and plated at low density (1:100-1:200 split to get around 40 colonies per well) on GT-coated 6-well plates in E8F medium. The next day (DIV0), media was changed to Medium A (Table 13) of the StemDiffTM Hematopoietic Kit (StemCell Technologies #05310). Half of the media was changed on DIV2. On DIV3, media was changed to Medium B (Table 13). On DIV5 and 7, again half of the medium was replaced, on DIV10 1 ml of medium was added on top. On DIV12 the emerged, floating hematopoietic precursor cells (HPCs) were harvested, spun down at 300 g for 4 min and either frozen in BamBanker or plated on GT-coated 6-well wells at 160.000 cells/well in microglia differentiation medium (DM1, Table 13). On DIV14 and DIV16, 1 ml of DM1 was added on top. On DIV 18 cells were washed off the plate and 50 % of the medium was transferred to new GT-coated 6-well wells and on both new and old wells 1 ml DM1 was added on top. On DIV20 and DIV22 again 1 ml DM1 was added on top. On DIV24 cells were washed off the plate with a P1000 pipette, collected, spun down at 300 g for 4 min, resuspended in NB+/B27+ media with the growth factors as in DM1 media, and added on 3D cultures.

Thawing of HPCs was performed as described for iPSCs, but after centrifugation cells were resuspended in DM1, plated onto GT-coated 6-well plates, and fed with DM1 as described above until they were collected for 2D or 3D cultures.

Table 13: Composition of media for microglia differentiation

Medium A	[ml]
StemDiff™ Hematopoietic Basal Medium	45
StemDiff™ Hematopoietic Supplement A	0.225
Medium B	[ml]
StemDiff™ Hematopoietic Basal Medium	75
StemDiff™ Hematopoietic Supplement B	0.375
Differentiation medium (DM1)	[ml]
DMEM/F-12 (Thermo Fisher #11320-074)	457.5
Penicillin-streptomycin (Thermo Fisher #15140-122)	5
B27 supplement (with Vit. A) (Thermo Fisher #17504-044)	10
GlutaMAX (Thermo Fisher #35050)	5
NEAA (Thermo Fisher #11140-050)	5
N-2 supplement (Thermo Fisher #17502048)	2.5
Insulin (500 µg/ml) (Sigma-Aldrich #10516)	5
Insulin-Transferrin-Selenium (ITS-G, 100x) (Thermo Fisher #41400045)	10
Monothioglycerol (Sigma-Aldrich #M1753-100ML)	0.0173
IL34 (Peprotech #200-34)	100 ng/ml
TGF-β (Peprotech #AF-100-21C)	50 ng/ml
M-CSF (Peprotech #300-25)	25 ng/ml

2.12. Long-term 2D cultures

To prepare 2D cortical neuron cultures, neural rosettes were split into single cells to pOL-coated 12-well plates or onto pOL-coated, acid-etched coverslips in 24-well plates. For the split, rosettes were incubated with Accutase for 10-12 min, washed off the plate with a P1000 pipette and triturated 8-10 times to yield single cells. Cells were counted, spun down, and resuspended in NB+/B27+ (Table 11) supplemented with 10 μ M DAPT (Selleckchem #S2215) at 1 million cells per ml. 1 million cells were plated per 12-well well and 0.5 million cells per 24-well wells. Two days after plating, cells were fed again with NB+/B27+ with 10 μ M DAPT. Three days after plating media was switched to NB+/B27+ supplemented with 10 μ M DAPT, 5 μ M 5-Fluorouracil (5-FU, Sigma-Aldrich #F6627) and 5 μ M Uridine (Sigma-Aldrich #U3750). Afterwards, half the medium was changed 2-3x per week. DAPT was added for a total of 7 days to promote terminal differentiation of residual NPCs. 5-FU and uridine were added for a total of 10 days to kill residual dividing cells while maintaining RNA translation.

To prepare 2D cortical neuron-astrocyte co-cultures, neural rosettes were split as described above. Astrocytes were split using Accutase for 5 min, counted, and mixed with the neurons in a 1:3 (astrocytes:neurons) ratio. Cells were spun down, resuspended at 1 million cells/ml, and plated and fed as described above.

To prepare 2D cortical neuron-astrocyte-microglia co-cultures, rosettes and astrocytes were split and plated as described above. After the treatment with 5FU and uridine ended, microglia at DIV24 of differentiation were washed off the plate and collected, spun down, counted, and added on top of the neuron-astrocyte co-cultures in NB+/B27+ medium supplemented with IL34, TGF- β and M-CSF as in microglial differentiation medium DM1 (Table 13). 150.000 microglia were added per 12-well well and 75.000 per 24-well well.

2.13. Long-term 3D cultures – Matrigel cultures

To prepare 3D cortical neuron cultures, neural rosettes were split into single cells as described in 2.12., but cells were resuspended in low volumes of NB+/B27+ media, and mixed on ice with cold Matrigel (Corning #11553620) using pre-chilled pipette tips, to a final Matrigel concentration of 7 μ g/ μ l and 25 Mio cells/ml. For transwell cultures, 100 μ l of the Matrigel-cell-suspension were then transferred to a 24-well transwell insert (VWR #734-0036) and left at 37 °C for 30 min to polymerize, before 1 ml of NB+/B27+ media was added to the 24-well well bottom compartment and 200 μ l to the top compartment. For free-floating cultures, 30 μ l of Matrigel-cell-suspension was added into dimples made by pressing parafilm onto a P200 tip rack, polymerized again for 30 min at 37 °C and then washed out of the dimples into 12-well wells using a P1000 tip and 1 ml of NB/B27+ media.

To prepare 3D neuron-astrocyte co-cultures, neural rosettes were split as described above. Astrocytes were split using Accutase for 5 min, counted, and mixed with the neurons in a 1:3 ratio (astrocytes:neurons), spun down and resuspended as indicated above to a total of 25 Mio cells/ml.

All cultures were fed with DAPT and 5FU as described in 2.12.

2.14. Long-term 3D cultures – 3BTMs

To prepare 3D cortical neuron cultures, neural rosettes were split into single cells as described in 2.12., but cells were not plated on pOL-coated plates but transferred to ultra-low attachment 96-well round-bottom plates (Sigma-Aldrich #CLS7007-24EA) at 250.000 cells/well and spun down 4 min at 300 g. Cells were then fed as described in 2.12. including supplementation with DAPT, 5FU and Uridine. 7-10 days after the split, aggregated 3D cultures were transferred to 12-well wells coated with anti-adherence rinsing solution (StemCell Technologies #07010) for long-term culture.

To prepare 3D neuron-astrocyte co-cultures, neurons and astrocytes were split as described for 2D cultures, and plated again at a neurons:astrocytes = 3:1 ratio with a total of 250.000 cells, spun down 4 min at 300 g and fed as described in 2.12..

To prepare 3D neuron-astrocyte-microglia co-cultures, neurons and astrocytes were mixed and aggregated as in 2.12.. After the treatment with 5FU and uridine ended, cultures were transferred to ultra-low attachment 96-well V-bottom plates (PHCBI #MS-9096VZ). Microglia at DIV24 were collected and added as in 2.12. in NB+/B27+ media with IL34, TGF- β and M-CSF. 40.000 microglia were added per 3D culture. When microglia had migrated into the cultures (4-7 days), cultures were transferred back to 12-well plates coated with anti-adherence rinsing solution for long-term culture.

For seeding experiments with APP/PS1 mouse brain lysates, brain lysate was obtained from Samira Parhizkar (AG Haass, DZNE, Munich) and processed as described previously 240 . Brain lysate was added when 3BTMs were generated at 1 μ l lysate per culture. For seeding experiments with recombinant A β 42 (Hölzel Biotech #AS-72216), lyophilized A β 42 was resuspended at 5 mM in DMSO and further diluted in PBS to 100 μ M. Resuspended peptide was incubated at 4 °C for 24 h before being frozen at -80 °C for long-term storage. For experiments, recombinant A β 42 was added into culture media at 1.25 μ M on day 8, 10, 13 and 15, before MG were added to the cultures.

2.15. Immunofluorescence stainings

For 2D immunofluorescence staining, cells were plated on pOL-coated, acid-etched cover slips as in 2.12. At the day of fixation, cells were washed once with PBS and fixed with 4% PFA for 10 min at RT. Cells were then washed with PBS for 3x 5 min and either stored in PBS with 0.02 % NaN₃ or stained immediately. For stainings, cells were blocked for 1 hour at RT in blocking solution, containing 3% donkey serum (Jackson ImmunoResearch #017-000-121), 0.1% Triton X-100 (Thermo Fisher # 85111) and 0.02% NaN₃ (Sigma-Aldrich #S2889) in PBS, and then incubated at 4 °C overnight with primary antibodies (Table 14) diluted in blocking solution. Unbound antibodies were washed off with PBS for 3x5 min and cells were incubated with secondary antibodies (Table 14) and 4',6-diamidino-2-phenylindole (DAPI, Thermo Fisher #D1306, stored as 5mg/ml stock solution, 1:50.000 dilution) diluted in blocking solution for 2 hours at RT in the dark. Cells were then washed again for 3x 5 min with PBS, and coverslips were mounted on glass slides (Thermo Fisher #J1800AMNZ) in Fluoromount-G (Thermo Fisher #00-4958-02). Coverslips were imaged with a fluorescent microscope (Zeiss Axio Observer Z.1) and images were processed in Fiji ²⁴¹.

3D cultures were washed once with PBS and fixed with 4 % PFA for 30 min at RT. Cultures were washed with PBS for 3x 30 min and transferred into 30 % sucrose in PBS with 0.02 % NaN₃ over night at 4 °C. Cultures were then transferred into OCT compound (Sakura Finetek Tissue-Tek O.C.T. Compound, Fisher Scientific #12351753), cryosectioned using a Leica CM1950 cryotome into 40 μm thick slices, transferred into PBS + 0.02 % NaN₃ and stored at 4 °C or stained immediately. For stainings, slices were mounted onto glass slides, dried on a heated plate at 45°C, surrounded with a liquid blocking line (Super PAP Pen, Science Services #N71312-N), rehydrated with MilliQ H₂O and transferred into a humidified box. Slices were blocked for 1 hour at RT and incubated overnight at 4 °C with primary antibodies diluted in blocking solution. Primary antibodies were washed off with PBS for 3x 20 min and cells were incubated with secondary antibodies and DAPI as described for 2D stainings. Slices were washed again with PBS for 3x 20 min in PBS and mounted in Fluoromount-G under cover glasses (Marienfeld #107222). TUNEL stainings were performed on slides as described above using the In Situ Cell Death Detection Kit, TMR red (Sigma-Aldrich #12156792910) according to manufacturer's instructions. Samples were imaged using a Zeiss LSM 880 confocal microscope using 10x, 40x and 100x objectives on ZEN black software, and images were processed and analyzed with Fiji. TUNEL-positive cells, Ki67-positive cells, DAPI-positive cells and AB puncta were quantified by thresholding the

relevant channel and subsequent use of the "Analyze Particles" function. Synapses were quantified using the SynQuant plugin ²⁴². 3D surface renderings of synapses on/in microglia were done using Imaris Version 9.4 (Oxford Instruments).

Table 14: List of primary and secondary antibodies used for stainings

Antibody	Species	Manufacturer	Reference	Dilution
Primary antibodies				
AT270	Mouse	Thermo Fisher	MN1050	1:200
CTIP2	Rat	Abcam	ab18465	1:300
K9JA (Tau)	Rabbit	Dako	A0024	1:1000
MAP2	Chicken	Millipore	AB15452	1:1000
NANOG	Rabbit	Cell Signaling	4903	1:500
OCT4	Rabbit	Stemgent	S090023	1:500
PSD95	Mouse	Thermo Fisher	MA1-046	1:250
SSEA4	Mouse	Abcam	ab16287	1:500
Synapsin-1	Rabbit	Cell Signaling	5297	1:500
TRA-1-60	Mouse	Millipore	MAB4360_2016625	1:500
82E1 (Aβ)	Mouse	IBL/Tecan	JP10323	1:100
GFAP	Guinea pig	Synaptic Systems	173004	1:500
lba1	Rabbit	Thermo Fisher	PA5-27436	1:500
Ki67	Rabbit	Abcam	ab15580	1:500
Cleaved Caspase 3	Rabbit	Cell Signaling	9664	1:500
SATB2	Mouse	Abcam	ab51502	1:100
GLAST	Mouse	Miltenyi Biotec	130-095-822	1:200
GLT1	Guinea Pig	Sigma-Aldrich	AB1783	1:300
S100β	Mouse	Sigma-Aldrich	S2532	1:300
TuJ1	Rabbit	Covance	MRB-435P	1:500
AQP4	Rabbit	Alomone labs	AQP-004	1:200
PU.1	Rabbit	Cell Signaling	2258	1:300
CD11b	Rabbit	Novusbio	NB110-89474SS	1:400
CD68	Rabbit	Bio-Rad	MCA1957	1:100
Hyaluronic acid binding protein-Biotin	recombinant	Hölzel-Biotech	HKD-BC41	1:100
• •	Seconda	ry antibodies		
Anti-chicken Alexa Fluor Plus 488	Goat	Thermo Fisher	A32931	1:500
Anti-chicken Alexa Fluor Plus 647	Goat	Thermo Fisher	A32933	1:500
Anti-mouse Alexa Fluor Plus 488	Donkey	Thermo Fisher	A32766	1:500
Anti-mouse Alexa Fluor 647	Donkey	Thermo Fisher	A31571	1:500
Anti-rabbit Alexa Fluor 568	Donkey	Thermo Fisher	A10042	1:500
Anti-rabbit Alexa Fluor 647	Goat	Thermo Fisher	A27040	1:500
Anti-rat Alexa Fluor 488	Donkey	Thermo Fisher	A21208	1:500
Anti-rat Alexa Fluor 647	Goat	Thermo Fisher	A21247	1:500
Anti-Guinea Pig Alexa Fluor 488	Goat	Thermo Fisher	A11073	1:500
Anti-Guinea Pig Alexa Fluor 568	Goat	Thermo Fisher	A11075	1:500
Peroxidase AffiniPure Donkey Anti- Rabbit IgG (H+L) HRP conjugate	Donkey	Jackson ImmunoResearch	711-035-152	1:10.000
Goat anti-Chicken IgY (H+L) Antibody, HRP	Goat	Thermo Fisher	A16054	1:10.000
Peroxidase AffiniPure Donkey Anti- Mouse IgG (H+L)	Donkey	Jackson ImmunoResearch	715-035-151	1:10.000
Avidin-FITC	-	Thermo Fisher	434411	1:500

2.16. Amyloid-β measurements in supernatant

Culture supernatant was conditioned for 5 days, collected into 1.5 ml tubes on ice, spun down for 5 min at 300 g at 4 °C, flash frozen in liquid nitrogen and stored at -80 °C until all samples were collected. After thawing on ice, supernatants were spun at 11,000 g for 10 min at 4 °C and used to measure secreted A β 38, A β 40 and A β 42 using the V-PLEX Plus A β Peptide Panel 1 Kit (6E10, Meso Scale Discovery #K15200G) according to manufacturer's instructions. To calculate "total A β " levels, measurements from the three different isoforms were summed up. For each sample, A β values were normalized to total protein or RNA levels extracted from lysate of the cultures used to condition the media. Protein extractions were done with the NucleoSpin RNA/Protein Kit (Macherey-Nagel #740993) according to manufacturer's instructions. Total protein levels were determined according to Karlsson et al. ²⁴³ as described in the kit and total RNA levels were determined on a Qubit 4 Fluorometer using the Qubit RNA High Sensitivity kit (Thermo Fisher #Q32852).

2.17. Sequential protein extraction

Protein was sequentially extracted from 3D cultures in 1) DEA buffer (0,2% DEA in 50mM NaCl, pH = 10), 2) RIPA buffer (Table 17) and 3) Guanidine buffer (buffer RP1 from Macherey-Nagel RNA/Protein Kit, without β -mercaptoethanol). To reduce protein degradation, all buffers were supplemented with protease inhibitor (Sigma-Aldrich #P8340, 1:200) and all steps up to addition of the Guanidine buffer were performed on ice or at 4 °C.

Table 15: Composition of RIPA buffer for sequential protein extraction

Component	Final concentration
TRIS-HCI pH = 7.5	20 mM
NaCl	15 mM
Na ₂ EDTA	1 mM
EGTA	1 mM
NP-40	1 %
Sodium deoxycholate	1 %
Sodium pyrophosphate	2.5 mM
MilliQ H ₂ O	

For initial lysis, 15-25 3D cultures were pooled per sample, transferred into 100 µl DEA buffer and dissociated using ceramic beads on a Precellys Evolution homogenizer at 6500 rpm for 30 sec at 4 °C. The cell suspension was then centrifuged for 10 min at 2500 g and the supernatant was transferred to an ultracentrifuge tube (Beckman Coulter #357448) without touching the pellet and spun down at 100.000 q for 30 min. The supernatant ("DEA fraction") was neutralized by addition of 1/10 0.5 M TRIS (pH = 6.75), transferred to a new, protein low-binding tube and flash frozen in liquid nitrogen. The resulting pellet was resuspended in 20 µl RIPA buffer, combined with the pellet from the first centrifugation step and homogenized again by pipetting 10-20 times until no clumps were visible. The resulting suspension was ultracentrifuged at 100.000 g for 30 min and the supernatant ("RIPA fraction") transferred to a new, protein low-binding tube and flash frozen. The resulting pellet was resuspended in 20 μ l Guanidine buffer by pipetting and ultracentrifuged at 100.000 g for 30 min. The resulting supernatant ("Guanidine fraction") contained the "insoluble" proteins and was again transferred to a new, protein low-binding tube and flash frozen. Protein concentrations in the different fractions were measured using Pierce BCA Protein-Assay (for DEA (undiluted) and Guanidine (1:2 diluted) fractions) and Pierce Detergent Compatible Bradford Assay Kit (for RIPA fraction, 1:10 diluted, Thermo Fisher #23246). Before samples were analyzed using the MSD Human Aβ V-PLEX kit (6E10),

RIPA and Guanidine fractions were diluted 1:10 with Diluent 35 from the kit to ensure compatibility with the assay. MSD assay results were normalized to total protein levels for each fraction and sample.

2.18. SDS-PAGE and Western Blotting

Total protein was extracted with the NucleoSpin RNA/Protein Kit (Macherey-Nagel #740933) according to manufacturer's instructions or as described in 2.22. (for phospho-Tau epitopes). 2-5 µg of protein were separated on 10% TRIS-Glycine gels hand-casted using the TGX Stain-Free™ FastCast™ Acrylamide Starter Kit, 10% (Bio-Rad # 1610182), first at 80 V for 25 min then at 120 V for 1-2 h, in a Mini-Protean Tetra Cell 4-Gel System attached to a Biorad PowerPac HC. Proteins were then transferred to nitrocellulose membranes (0,45 µm pore size, VWR #10600002) at 100 V for 1 h on ice. For running buffer and blotting buffer see Table 16.

Table 16: Composition of buffers used for SDS-PAGE and Western Blot

Running buffer for SDS-PAGE	Final concentration	
TRIS base (AppliChem #A2756.0500)	25 mM	
Glycine (Sigma-Aldrich #G8898-500G)	192 mM	
Sodium dodecyl sulfate (SDS, Carl Roth #CN30.2)	1 mM	
Blotting Buffer for Western Blot		
TRIS base (Sigma-Aldrich	25 mM	
Glycine (Sigma-Aldrich #G8898-500G)	192 mM	
Methanol (Carl Roth #0082.3)	20 %	
TBS		
TRIS base	20 mM	
NaCl	137 mM	
Adjust pH to 7.6 with HCl, add 0,1 % Tween-20 for TBS-T		

Membranes were blocked in 3 % BSA (Sigma-Aldrich #A9418) in TBS-T (Table 16) and incubated in primary antibody (Table 14, AT270 1:400, K9JA 1:10.000) in 1 % BSA in TBS-T overnight at 4 °C. After 3x 10 min washes in TBS-T, HRP-labeled secondary antibodies (Table 14) were added for 1 h at RT in the same diluent as primary antibodies. After 3x 10 min washes in TBS-T protein signals were detected using Clarity Western ECL Substrate (BioRad #170-5060) on a Fusion Fx7 imager (Vilber). Band intensities were measured using FiJi.

To detect A β , the protocol was altered as follows: Proteins were separated using Tricine-SDS-Page on a hand-casted, three-layered gel as shown in Table 17, based on a published protocol ^{244,245} with minor modifications.

Table 17: Composition of gels for Aβ western blot

	Stacking gel	Intermediate gel	Resolving gel
38 % Glycerol			1,6 ml
ddH2O	1,4 ml	1,2 ml	
30 % Acrylamide	0,3 ml	0,8 ml	2,7 ml
3M TRIS HCI, pH = 8.45		1 ml	2,14 ml
1M TRIS HCI, pH = 8.45	0,3 ml		
10 % SDS	20 μΙ	30 μΙ	60 µl
10 % APS	20 μΙ	30 μΙ	60 µl
TEMED	2 µl	3 µl	3 μΙ

SDS-PAGE was performed with separate anode and cathode buffers. Anode buffer was made of 0.2 M Tris-HCl (pH = 8.9), cathode buffer was made of 0.1 M Tris-HCl, 0.1 M Tricine and 0.1 % SDS. 2 Gels were run at the same time for 40 min at 70 V followed by 90 min at 120 V. Proteins were transferred onto 0.2 μ m nitrocellulose membranes (VWR #10600011) for 50 min at 100 V in blotting buffer as described above, but without methanol. After transfer, membranes were immediately boiled in PBS for 5 min, then blocked in 4 % milk in TBS-T for 1h and processed as described above with antibodies diluted in 2 % milk in TBS-T.

2.19. Electrophysiological measurements

Experiments were performed by Dr. Lars Paeger at AG Herms (DZNE Munich) on slices from 6-month-old 3D cultures. Sections were cut after embedding the 3D cultures in 4% low-melting point agarose. Agarose was prepared ~12 hours prior to experiments and stored in small plastic cubes overnight at 4°C. Before slicing, agarose in plastic cubes was heated in a microwave and put in the fridge for ~2 min until temperature dropped to ~35°C. 3D cultures were transferred from culture medium into agarose using a small glass pasteur pipette. Quickly, agarose including 3D cultures were placed at -20°C for 30-60s until agarose became rigid. Subsequently, the agarose block was trimmed and glued on the specimen holder of a vibratome and placed in ice cold (2-4°C) cutting solution containing (in mM): NMDG, 2.5 KCl, 2 MgCl2, 2 CaCl2, 1.2 NaH2PO4, 10 HEPES, 21 NaHCO3, and 5 Glucose adjusted to pH 7.2 with HCl. Sections were recovered for 15 mins in preheated (36°C) cutting solution and 40-60 minutes at RT in normal aCSF containing (in mM): 125 NaCl, 2.5 KCl, 2 MgCl2, 2 CaCl2, 1.2 NaH2PO4, 21 NaHCO3, 10 HEPES, and 5 Glucose adjusted to pH 7.2 with NaOH. While recording, sections were continuously superfused with carbogenated aCSF at a flow rate of ~2 ml/min and a temperature of 30-32°C.

Current-clamp recordings were performed in the perforated patch clamp configuration. Neurons were visualized with a fixed stage upright microscope (BX51WI, Olympus, Hamburg, Germany) using 60x water-immersion objectives (LUMplan FL/N 60x, 1.0 numerical aperture, 2 mm working distance, Olympus). Electrodes with tip resistances between 4 and 6 M Ω were fashioned from borosilicate glass (0.86 mm inner diameter; 1.5 mm outer diameter; GB150-8P; Science Products) with a vertical pipette puller (PC-10; Narishige, London, UK). All recordings were performed with an EPC10 patch-clamp amplifier (HEKA, Lambrecht, Germany) controlled by the program PatchMaster (version 2.32; HEKA). In parallel, data were recorded using a micro1410 data acquisition interface and Spike 2 (version 10) (both from CED, Cambridge, UK). Data were sampled at 25 kHz and low-pass filtered at 2 kHz with a four-pole Bessel filter. The calculated liquid junction potential of 14.6 mV between intracellular and extracellular solution was compensated or subtracted offline (calculated with Patcher's Power Tools plug-in from https://www.mpibpc.mpg.de/groups/neher/index.php?page=softwarefor IGOR Pro 6 (Wavemetrics, Lake Oswego, OR, USA)). Recordings were performed with pipette solution containing (in mM): 147 K-gluconate, 10 KCl, 10 HEPES, 0.1 EGTA, 2 MgCl2 adjusted to pH 7.2 with KOH. ATP and GTP were omitted from the intracellular solution to prevent uncontrolled permeabilization of the cell membrane. The patch pipette was tip filled with internal solution and back filled with internal solution, which contained the ionophore to achieve perforated patch recordings and 0.02 % tetramethylrhodamine-dextran (3000 MW, D3308, Invitrogen) to monitor the stability of the perforated membrane. Amphotericin B (A4888; Sigma) was dissolved in DMSO (D8418, Sigma) to a concentration of 40 mg/ml. The used DMSO concentration (0.1%–0.3%) had no obvious effect on the investigated neurons. The ionophore was added to the modified pipette solution shortly before use. The final concentration of amphotericin B was ~200-240 mg/ml. Amphotericin solutions were prepared from undissolved weighted samples (stored at 4 °C protected from light) on every recording day. During the perforation process, access resistance (Ra) was constantly monitored, and experiments were started after Ra had reached steady state (\sim 5–20 min) or the action potential amplitude was stable.

Intrinsic characteristics were quickly determined using a set of depolarizing and hyperpolarizing current injection either in perforated mode with stable action potential amplitude and/or membrane potential or after the membrane ruptured spontaneously.

2.20. 2-Photon live cell imaging

Experiments were performed together with Dr. Severin Filser at AG Plesnila (ISD) on a Zeiss LSM 7 MP multi-photon microscope using a W Plan-Apochromat 20x/1.0 DIC D=0.17 M27 75mm objective. Cultures were immobilized in a 60 mm dish (VWR#734-2318) in 5μ droplets of low-melting point agarose (Thermo Fisher #R0801): Agarose was heated until liquid, cooled down to ~40°C, 5μ droplets were placed on the 60 mm dish, cultures were transferred onto the top of the droplets with a cut P200 tip, and normal culture media (NB+/B27+) was carefully added. Dishes were placed on a heat pad under the microscope and imaging was started. Experiments were performed using YFP-expressing microglia and an excitation wavelength of 950 nm. Time lapse experiments of z-stacks were done at 3x zoom for 15 minutes with 30-45 seconds between acquisitions.

2.21. Single-cell RNA sequencing (scRNAseq)

To obtain a single cell suspension for scRNAseq, cultures at 1 or 3 months of age were dissociated using the Neural Tissue Dissociation Kit P (Miltenyi Biotec #130-092-628). For each sample, 7-8 cultures were pooled and dissociated in a mix of 2.375 ml buffer X, 62.5 μ l enzyme P, 10 μ l enzyme A 20 μ l buffer Y and 11.25 μ M Actinomycin D (Sigma-Aldrich #A1410) in gentleMACSTM C Tubes (Miltenyi Biotec #130-093-237) on a gentleMACSTM Octo Dissociator (Miltenyi Biotec #130-095-937). A custom protocol was used as described in Table 17.

Table 18: 3D culture dissociation protocol for gentleMACS™ Octo Dissociator			
Step	Time (min)	Rotation speed (rpm)	Ro

Step	Time (min)	Rotation speed (rpm)	Rotation direction
1	4.5	20	Counter-clockwise
2	0.5	100	clockwise
3	4.5	20	Counter-clockwise
4	0.5	250	clockwise
5	4.5	20	Counter-clockwise
6	0.5	300	clockwise
7	4.5	20	Counter-clockwise
8	0.5	300	clockwise
9	2	20	Counter-clockwise

After dissociation, the cell suspension was always kept on ice or at 4 °C during centrifugations, and all plasticware was pre-treated with 1 % bovine serum albumin solution (BSA, from 7.5 % stock, Thermo Scientific #15260-037) to prevent cell adhesion. To prepare cells for fluorescence-activated cell sorting (FACS), the cell suspension was transferred to 15 ml tubes (VWR #525-0061) through a 70 μm cell strainer pre-wet with PBS and spun down at 300 g for 5 min. The supernatant was discarded, and cells resuspended in 50 μl FACS buffer (Thermo Scientific #00-4222-26) and transferred to FACS tubes (Corning #352052). As always 2 samples were to be pooled during FACS, the cell suspension was then incubated for 20 min with Hashtag-coupled Antibodies (Sample 1 with TotalSeqTM-B0251 anti-human Hashtag 1 Antibody (Biolegend #394631), sample 2 TotalSeqTM-B0252 anti-human Hashtag 2 Antibody (Biolegend #394633). Next, 1 ml of FACS buffer was added to wash and cells were pelleted again for 5 min at 300 g and resuspended in 300 μ l FACS buffer. 5 min before sorting, DAPI was added at 250

ng/ml to exclude dead cells. Single, live cells were sorted on a FACSAria Fusion (BD Biosciences) into cooled, 2 ml protein low-binding tubes (Eppendorf #0030108132) filled with 1 ml FACS buffer. The same number of cells from samples 1 and 2 (labelled with different hashtag antibodies) were pooled into the same collection tube. Samples were then further processed, including GEM generation, reverse transcription, library preparation and sequencing, by the Synergy Transcriptome Hub at AG Beltrán.

Cells were washed in 0.04% BSA/PBS and approximately 16,500 cells per sample were loaded onto the 10x Chip G (10× Genomics). Single cell gene expression and cell hashing libraries were generated on the 10× Genomics Chromium platform using the Chromium Next GEM Single Cell 3' Reagent Kits v3.1 according to the manufacturer's protocol (CG000317 Rev C). Gene expression and hashtag libraries were sequenced on a NovaSeq 6000 S4 v1.5 flow cell (Illumina).

Raw paired-end sequencing files of the GEX and cell hashing libraries were aligned to the human GRCh38 reference genome and reference hashtag barcode sequences using 10x Genomics Cell Ranger (v6.0.0). Filtered gene- and hashing-barcode matrices with unique molecular identifier (UMI) counts that reached the threshold for cell detection were supplied into the R package Seurat (version 4.1.0). Cells that expressed fewer than 500 genes and/or >15% mitochondrial reads, and genes expressed in less than 3 cells were removed from the count matrix. Cell hashing raw counts were normalized using centered log ratio (CLR) transformation, where counts were divided by the geometric mean of a hashtag across cells and log-transformed. We filtered out doublets and cells where no hashtag was detected. After QC, only raw gene counts in high-quality singlets were submitted to: log-normalization; identification of high variable genes by using the vst method; scaling; and regression against the number of UMIs and mitochondrial RNA content per cell. 2000 variable features were supplied as input to principal component analysis (PCA). The first 7 dimensions were used to assign the cells to transcriptional clusters with the Seurat functions FindNeighbors and FindClusters 246 at a cluster resolution of 0.5 using a graph-based clustering approach incorporating Louvain modularity optimization and hierarchical clustering. UMAP was calculated using the first 7 dimensions. Differentially expressed genes between each cluster and all other cells were calculated using the FindAllMarkers function. Cell clusters were annotated by combination of up-regulated genes for each cluster and visual inspection of key markers using UMAP visualization.

2.22. Mass spectrometry

For mass spectrometry analysis, 3D cultures were washed once with PBS and then dissociated in RIPA buffer (Table 16) supplemented with protease inhibitors (Sigma-Aldrich #4693159001) and phosphatase inhibitors (Sigma-Aldrich #4906845001) using ceramic beads (VWR #432-0293) on a Precellys® Evolution homogenizer as in 2.18.. For each sample, three 3D cultures were pooled to increase total protein yield. After dissociation, the lysates were transferred to 1.5 ml protein low-binding tubes (Eppendorf #0030108116) on ice and centrifuged for 20 min at 18.000 g and 4 °C. Supernatants were transferred to a new, 1.5 ml protein low-binding tube and protein concentrations were measured using PierceTM BCATM Protein-Assay (Thermo Scientific #23227) following the manufacturer's instruction for the microplate assay. Samples were then frozen at -80 °C until analysis. All further processing, including sample preparation and analysis, was performed in the Synergy Proteome hub.

Table 19: Composition of RIPA buffer for Mass spectrometry

Component	Final concentration
Milli-Q water	
HEPES-KOH, pH 7.5	50mM

LiCl	500mM
EDTA, pH 8.0	1mM
Igepal (NP40)	1%
Sodium desoxycholate	0,7%

2.22.1. Sample Preparation

A protein amount of 15 μ g per sample was subjected to tryptic digestion. First, 100 mM MgCl2 was added to a final concentration of 10 mM and DNA was digested with 25 units Benzonase (Sigma Aldrich, US) for 30 min at 37°C. Proteins were reduced at 37°C for 30 min with 15 mM dithiothreitol (DTT) followed by cysteine alkylation with 60 mM iodoacetamide (IAA) for 30 min at 20 °C. Excess of IAA was removed by adding DTT. Detergent removal and subsequent digestion with 0,2 μ g LysC and 0,2 μ g trypsin (Promega, Germany) was performed using the single-pot, solid-phase-enhanced sample preparation as previously described ²⁴⁷. After vacuum centrifugation, peptides were dissolved in 20 μ L 0,1% formic acid (Sigma Aldrich, US). Peptide concentrations after tryptic digestion were estimated using the Qubit protein assay (Thermofisher Scientific, US).

2.22.2. LC-MS/MS analysis

350 ng of peptides were separated on a nanoElute nanoHPLC system (Bruker, Germany) in an in-house packed C18 analytical column (15 cm \times 75 μ m ID, ReproSil-Pur 120 C18-AQ, 1.9 μ m, Dr. Maisch GmbH). Peptides were separated with a binary gradient of water and acetonitrile (B) containing 0.1% formic acid at flow rate of 300 nL/min (0 min, 2% B; 2 min, 5% B; 94 min, 24% B; 112 min, 35% B; 120 min, 60% B) and a column temperature of 50°C.

The nanoHPLC was online coupled to a TimsTOF pro mass spectrometer (Bruker, Germany) with a CaptiveSpray ion source (Bruker, Germany). For relative protein quantification, a Data Independent Acquisition (DIA) – Parallel Accumulation Serial Fragmentation (PASEF) method was used ²⁴⁸. Each scan cycle included one full MS scan followed by 34 windows of 26 m/z width (1 m/z overlap) covering an m/z range of 350-1200 using 2 windows per PASEF ramp of 100 ms. This resulted in a cycle time of 1.9 s. One measurement per lysate from 3D cultures was performed.

2.22.3. Data Analysis

The MS raw data was analyzed with the Software DIA-NN (Version 1.8) ²⁴⁹. First, a spectral library was generated in DIA-NN using 24 samples. Trypsin was defined as protease and 2 missed cleavages were allowed. The data was searched against a canonical one protein per gene human protein database from UniProt (download: 2022-01-18, 20600 entries). Oxidation of methionines and acetylation of protein N-termini were defined as variable modifications, whereas carbamidomethylation of cysteines was defined as fixed modification. The precursor and fragment ion m/z ranges were limited from 350 to 1200 and 200 to 1700, respectively. Peptide and peptide fragment tolerances were optimized by DIA-NN. The match between runs option was enabled. An FDR threshold of 1% was applied for peptide and protein identifications. The generated spectral library includes 12550 protein isoforms, 13783 protein groups and 187812 precursors in 149807 elution groups. Afterwards, all samples were searched against this spectral library with the same settings for protein label-free quantification (LFQ).

Keratins were deleted from the results tables because of likely skin particle contaminations. For statistical analysis, results from all iPSC derived cultures were compared with each other by means of cell composition, culture time, and APP mutations. Therefore, only proteins were considered which were quantified in all 6 replicates of at least one experimental group. After log2 transformation of LFQ intensities, missing log2 LFQ intensities were imputed from a normal distribution using a width of 0.3 standard deviations of the data with a downshift of 1.8 using the software Perseus (Version 1.6.14.00)

 250 . To account for multiple comparison, first a one-way Anova test was used to determine if there are any statistically significant differences between the means of experimental groups. Afterwards, individual Student's T-tests were applied to evaluate proteins with significantly different abundances between the experimental groups. Additionally, a permutation based false discovery rate estimation was used with an FDR of 5% at s0 = 0.1 as threshold to take multiple comparisons into account.

UniProt subcellular location annotations were added based on the protein group accession numbers (download: 2019-06-18).

2.23. Statistical analysis

No statistical methods were used to predetermine sample size and the experiments were not randomized. Experimental data was analyzed for significance using GraphPad Prism 9. Multiplicity-adjusted p < 0.05 was considered statistically significant. Significance was analyzed either by T-tests, if only 2 groups were compared, one-way ANOVA if more than 2 groups were compared with 1 independent variable, two-way ANOVA if more than 2 groups were compared with 2 independent variables, and mixed models if more than 2 groups were compared with 2 independent variables and single missing values. Multiple-comparison post-testing with Dunnett's, Tukey's or Šidák's method was performed as recommended by the software. All graphs are shown as mean + standard deviation (SD). *p < 0.05, **p < 0.01, ***p < 0.001, ****p < 0.0001.

Table 20: Primer IDs, Names and Sequences according to the PaquetLab database

ID	Name	Sequence
OL1206	APPswe 4R DP	ATCCTATAGGCAAGCATTGTATTTTTA
OL1207	APPswe 5F DP	GGGTAGGCTTTGTCTTACAGTGTTAT
OL1208	APP_Intron16_F1 JK	CAACCAGTTGGGCAGAGAAT
OL1109	APP_Intron16_F2 JK	CCAAATGTCCCCTGCATTTA
OL1212	APP_Intron17_R3 JK	CATGGAAGCACACTGATTCG
OL1240	D1S80-F_IW	GAAACTGGCCTCCAAACACTGCCCGCCG
OL1241	D1S80-R_IW	GTCTTGTTGGAGATGCACGTGCCCCTTGC
OL1512	JK_gR58_offtarget_1_F1	ATCGTCAGGCTGTTTCCATC
OL1513	JK_gR58_offtarget_1_R1	CAGCCCTTAATGATCCCAGA
OL1516	JK_gR58_offtarget_3_F1	TTGAAAAGCATGGGGTTCTC
OL1517	JK_gR58_offtarget_3_R1	GCTTCCACAGGAGGACTCAG
OL1518	JK_gR58_offtarget_4_F1	CCAGGAGCAGGAAGTCAGG
OL1519	JK_gR58_offtarget_4_R1	TTGCAGATGTGGCCATAAAA
OL1520	JK_gR58_offtarget_5_F1	TCCTGTCATTTGGAGCACAG
OL1521	JK_gR58_offtarget_5_R1	TGAGGACAGCAGGTCAACAG
OL1522	JK_gR133_offtarget_1_F1	TTGTCCATTTGGGGAAAAA
OL1523	JK_gR133_offtarget_1_R1	TGAGAATGAGACTCAGCAGTAATGT
OL1524	JK_gR133_offtarget_2_F1	ATTGAAGCAAGTGCATGGTG
OL1525	JK_gR133_offtarget_2_R1	GGAAAAGAGAGGAGGAAGAGG
OL1526	JK_gR133_offtarget_3_F1	TGCTCATCAAGAAGGCATTG
OL1527	JK_gR133_offtarget_3_R1	AGTCGCCTTGAGATGAGAGC
OL1528	JK_gR133_offtarget_4_F1	GGTCCCATTGAATCTGCTGT
OL1529	JK_gR133_offtarget_4_R1	CCTGGTAAAAGTTTGGGAGGT
OL1530	JK_gR133_offtarget_5_F1	TGGTTTTCCCAAGGAAGAAG
OL1531	JK_gR133_offtarget_5_R1	GGTTTCTGCTGACAAATCTGC
OL1546	JK_gR58_offtarget_2_F3	CCAGGGAATAGTGGAAGGTG
OL1547	JK_gR58_offtarget_2_R2	CCAGGCATGCATTTGTCTTT

BCL2L1_F	BCL2L1 CNV assay F Set 1	GGTGGTTGACTTTCTCTCCTAC
BCL2L1_R	BCL2L1 CNV assay R Set 1	TCTCCGATTCAGTCCCTTCT

3. Results

3.1. Differentiation of human iPSCs into neurons, astrocytes, and microglia

The first aim of this thesis was the development of a novel iPSC-based cortical tissue model made of multiple human brain cell types in a 3D tissue-like environment. We therefore first established the differentiation of healthy donor iPSCs into cortical neurons, astrocytes, and microglia (Figure 11).

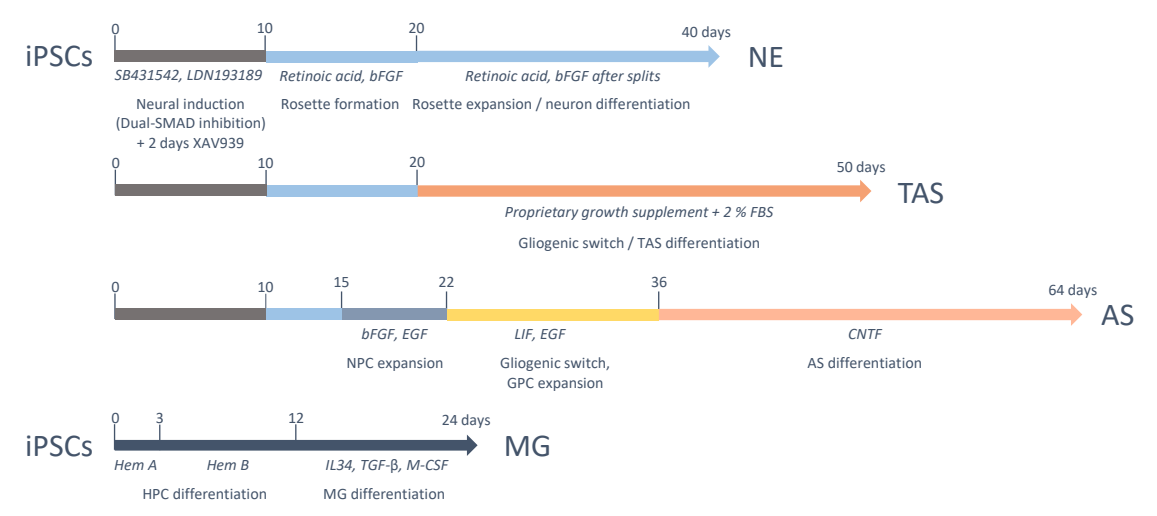


Figure 11: Differentiation protocols for iPSC-derived brain cell types. Cortical neurons (NE) were differentiated by dual-SMAD inhibition and initial Wnt inhibition to push cells into the forebrain lineage. Cells were then kept at high density with supplementation of retinoic acid and bFGF until neural rosettes formed. Rosettes were expanded at high density until early neurons formed in the culture around day 40. Astrocytes were initially differentiated according to the protocol published by TCW et al. 251 (TAS). Cells were treated as for NE differentiation until Day 20, then rosettes were split into single cells and media was changed to commercial Astrocyte Medium (ScienCell) supplemented with the proprietary growth supplement and 2 % FBS to induce the gliogenic switch and astrocyte differentiation for 30 days. As serum exposure has been shown to activate astrocytes 162, and the resulting cells did not survive in the medium used for co-cultures with neurons, the protocol was later changed and astrocytes (AS) were generated as published by Perriot et al. 161. To this end, cells were treated as for NE differentiation until Day 15, then rosettes were split into single cells and treated with bFGF and EGF to expand neural progenitor cells (NPCs). To induce gliogenic switch to glia progenitor cells (GPCs), cells were treated with LIF and EGF for 14 days. The resulting GPCs were treated with CNTF for 28 days to induce astrocyte differentiation and maturation. Microglia (MG) differentiation was adopted and optimized from the protocol by Abud et al. 151, resulting in a protocol very similar to the version of McQuade et al. published shortly thereafter 152 with minor modifications. iPSCs were first differentiated into hematopoietic precursor cells (HPCs) with a commercially available medium kit (StemCell Technologies). Cells were first incubated in Hem A medium for 3 days, followed by Hem B medium for 9 days. The resulting HPCs were collected and treated with a differentiation medium containing IL34, TGF-β and M-CSF to induce MG differentiation for 12 days.

For the differentiation into cortical neurons (NE), we adopted a published protocol 252 that uses initial dual-SMAD inhibition to differentiate iPSCs to neural precursor cells (NPC), and further optimized and modified it as described by Paquet et al. 154 (Figure 11-NE). For the first two days, a WNT antagonist was added additionally to promote cortical forebrain fate 148 . NPCs were then cultured at high density with supplementation of retinoic acid for several weeks to promote expansion of NPCs into neural rosettes and differentiation into excitatory, cortical forebrain neurons. The resulting cells form dense networks (Figure 12A, left) and express typical markers such as CTIP2 for deep-layer cortical neurons, SATB2 for mid-layer cortical neurons, β 3-Tubulin (TuJ1) (Figure 12A, middle), and MAP2 and form synapses as seen by colocalization of Synapsin-1 (Syn) as pre- and PSD95 as post-synaptic marker (Figure 12A, right).

To differentiate cortical astrocytes (AS) from iPSCs, I first established the protocol published by TCW et al. 251 (Figure 11 – TAS). I could implement the protocol and generate cells which expressed typical markers such as excitatory amino acid transporters 1 and 2 (GLAST1 and GLT1, Figure 12B, middle), Aquaporin 4 and GFAP (Figure 12B, right).

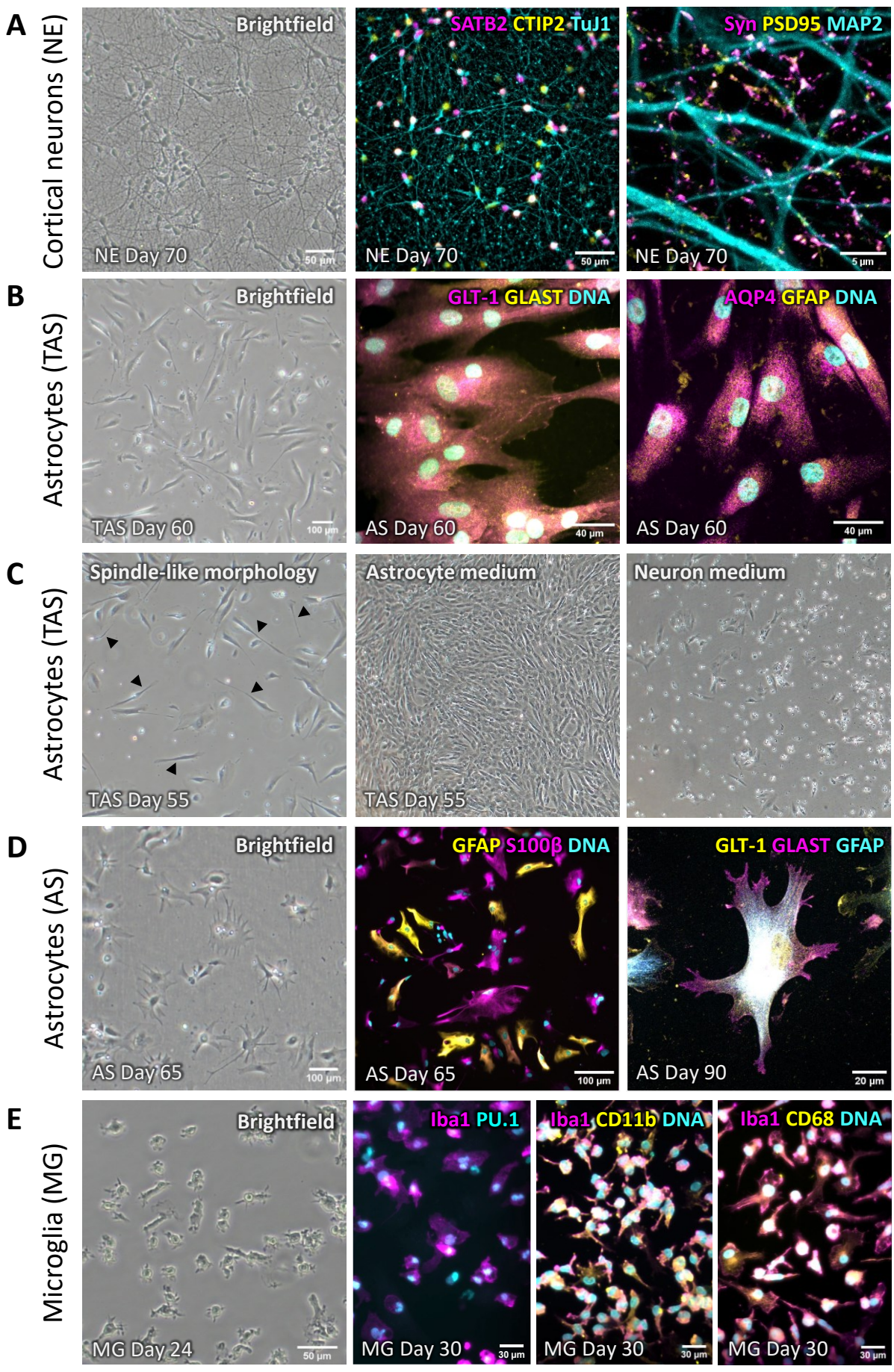


Figure legend next page >

Figure 12: Characterization of iPSC-derived brain cell types. A) Left: Cortical neurons (NE) on Day 70 after iPSC stage display typical morphologies and form dense neuritic networks seen in brightfield image. Middle: NE express cortical markers SATB2 and CTIP2 and neuron-specific beta-III tubulin (stained by TuJ1 antibody) as seen in immunofluorescence (IF) staining. Right: NE form synapses as seen by colocalization of presynaptic Synapsin-1 (Syn) and postsynaptic PSD95 on MAP2-positive neurites. B) Left: Brightfield image showing morphology of TAS (differentiated as in TCW et al. ²⁵¹) on Day 60 after iPSC stage. Middle: TAS express typical astrocyte markers Glutamate transporter 1 (GLT-1) and Glutamate Aspartate Transporter 1 (GLAST). Right: TAS are positive for Aquaporin-4 (AQP4) and glial fibrillary acidic protein (GFAP). C) Left: Spindle-like morphology of TAS indicates reactive state. Middle+right: TAS survive well in astrocyte medium (middle) but die after few days in neuron medium used for co-cultures (right). D) Left: Star-shaped morphology of AS differentiated as in Perriot et al. ¹⁶¹. Middle: AS express heterogeneous levels of S100beta and GFAP. Right: AS express GLT-1 and GLAST. E) Left: Microglia (MG) morphology as seen in brightfield microscope. Middle+right: MG express typical markers Iba1, PU.1, CD11b and CD68.

However, the protocol uses a commercial, proprietary media formulation containing FBS, which has been shown in mouse cells to induce lasting changes in the cells similar to an "activated" cell state, even after FBS was removed ¹⁶². Indeed, our iPSC-TAS partially had an activated appearance as seen by the spindle-like morphology in brightfield pictures (Figure 12C, left). In addition, when establishing NE+TAS co-cultures I noticed that TAS survival was very low. As TAS in monoculture were kept in the commercial, proprietary media compared to the defined neuronal media used for the NE+TAS cocultures, I hypothesized that the media change may cause the cell death. Indeed, when adding neuronal media to TAS 2D monocultures, I could recapitulate the astrocyte degeneration (Figure 12C, middle+right). To avoid these caveats, we decided to switch to a different, more defined protocol 150,161 (Figure 11 – AS) that does not use FBS and a differentiation media closer to the one we use for NE+AS co-cultures. The resulting cells had a more typical, star-shaped morphology (Figure 12D left) and again expressed typical markers such as GFAP, S100β, GLAST and GLT-1 (Figure 12D, middle+right). Interestingly, we found a heterogeneity of GFAP and S100\beta expression levels throughout the cultures (Figure 12D, middle), potentially mimicking the astrocytic heterogeneity found in human brain ²⁵³. In addition, survival and integration into the NE-AS co-cultures was strongly improved. Therefore, we decided to use this protocol for further experiments.

Differentiation of microglia (MG) from human iPSCs was established together with Gernot Kleinberger (AG Haass, DZNE Munich, then ISAR Bioscience GmbH) and Maryam Khojasteh-Fard (AG Haass). Again, we adopted a published approach ¹⁵¹ and optimized it, resulting in a protocol very similar to a simplified and refined version published shortly after by the original group ¹⁵². This version uses a commercially available media kit for the first step – the differentiation into hematopoietic progenitor cells (HPCs) – followed by the differentiation into MG by addition of specific cytokines and growth factors (Figure 11 – MG). The resulting cells had a typical morphology (Figure 12E, left) and expressed typical markers such as Iba1, PU.1, CD11b, and CD68 (Figure 12E, middle+right).

In summary, we could adopt and optimize protocols to differentiate iPSC into highly pure populations of cortical neurons, astrocytes, and microglia in 2D monocultures.

3.2. Generation and optimization of 3D co-cultures of iPSC-derived brain cell types

To generate a more physiological culture system and enable formation of additional AD phenotypes such as extracellular protein aggregation, we next established 3D co-cultures of the different brain cell types. As mentioned above, currently used 3D *in vitro* models such as organoids have several drawbacks that limit their use for mechanistic studies and screens. Therefore, we aimed to develop a novel, more reproducible and controllable model. A main source of variability of organoids is the initial aggregation of iPSCs and subsequent differentiation in a 3D format. Although this more closely mimics the *in vivo* situation, it also leads to heterogeneous, non-controllable access to patterning factors of the aggregated cells, contributing to the large variability within and between different batches of organoids. To avoid this caveat, we decided to differentiate the iPSCs in a more controllable 2D format

as described in 3.1., yielding highly uniform and pure cultures of differentiated brain cells that we then combined to establish a modular 3D culture system. To generate this 3D environment, I initially adopted a method used by Choi et al. 207 by embedding the cells into Matrigel, a hydrogel extracted from the basement-membrane matrix of a mouse tumor ²⁵⁴. I tested different culture formats such as thick-layer cultures in transwell inserts as well as embedding the cells in droplets of Matrigel to yield free-floating cultures to improve nutrient and oxygen supply (Figure 13A). For all approaches, I first embedded NE and AS, that were then treated with DAPT to drive residual NPCs into terminal differentiation into neurons by Notch inhibition, followed by treatment with 5-FU to kill residual dividing cells and yield a postmitotic culture. Microglia were added into the media of the cultures only after this treatment and would migrate into the cultures by themselves (Figure 13A). As the dropletbased cultures were more affordable and could be scaled up more easily, I decided to use this approach for further testing. I characterized the cultures using immunofluorescent stainings and observed successful embedding and survival of the cells and the formation of neuritic and astrocytic processes (Figure 13B, left) and incorporation and distribution of microglia throughout the cultures (Figure 13B, right) as well as formation of synapses (Figure 13C). I thus established a human 3D culture made of iPSC-derived neurons, astrocytes, and microglia.

However, larger experiments with more cultures showed a low reproducibility especially between batches regarding general cell survival and neurite formation (as seen in Figure 13B left vs. right). In addition, due to the large size of the cultures of around 2-3 mm in diameter, I observed necrotic core formation after around 2 months (Figure 13D), similar to organoid models. In addition, the use of Matrigel as a scaffold does have drawbacks, as it introduces a non-human component into the system, contains growth factors by itself that influence cellular processes such as proliferation and maturation and that vary from batch to batch, and is in its composition not similar to human brain ECM. As a basement membrane matrix, it consists of Laminin (~60 %), Collagen IV (~30 %), Nidogen-1 (~8 %) and heparan sulfate proteoglycans ²⁵⁵, while human brain interstitial matrix is mainly build of hyaluronan and chondroitin sulfate proteoglycans with Tenascins as linkage molecules and only small amounts of Laminin, Collagen IV and Fibronectin ¹⁹³.

Based on these results and limitations, we decided to test a different approach based on the selfaggregation of the differentiated cells into smaller spheres, to avoid necrotic core formation, and without any artificial matrix. From here on, most optimizations and characterizations were performed together with Carolina Cardoso Gonçalves, another PhD student in the lab. We hypothesized that similar to iPSC aggregation at the beginning of organoid formation, also differentiated cells should aggregate into a sphere when transferred to an ultra-low attachment (ULA), U-bottom plate that does not allow binding to the plate walls (Figure 13E). Indeed, when adding iPSC-derived NE or NE and AS into ULA plates, we observed sphere formation after around 4-5 days, without addition of any exogenous extracellular matrix. The resulting cultures were very reproducible in size and general morphology (Figure 13F), and IF stainings confirmed cell survival inside the cultures, without formation of a necrotic core (Figure 13G). Both neurons and astrocytes reproducibly grew dense networks, suggesting a mature cell morphology. Again, we could incorporate MG into the cultures by adding the cells into the media of aggregated NE+AS cultures. The cells then migrated into and tiled the cultures and adopted a ramified morphology (Figure 13G). Microglia integration efficiency was even higher than for Matrigel cultures and close to 100 %, as the cells could not bind to the plate and NE and AS likely produce chemokines attracting the MG inside the culture.

Altogether, this approach allowed us to generate large amounts of uniform and reproducible 3D cultures made of human neurons, astrocytes, and microglia, and we thus decided to further characterize these 3D cortical brain tissue models (3BTMs) and use them for modelling AD pathogenesis *in vitro*.

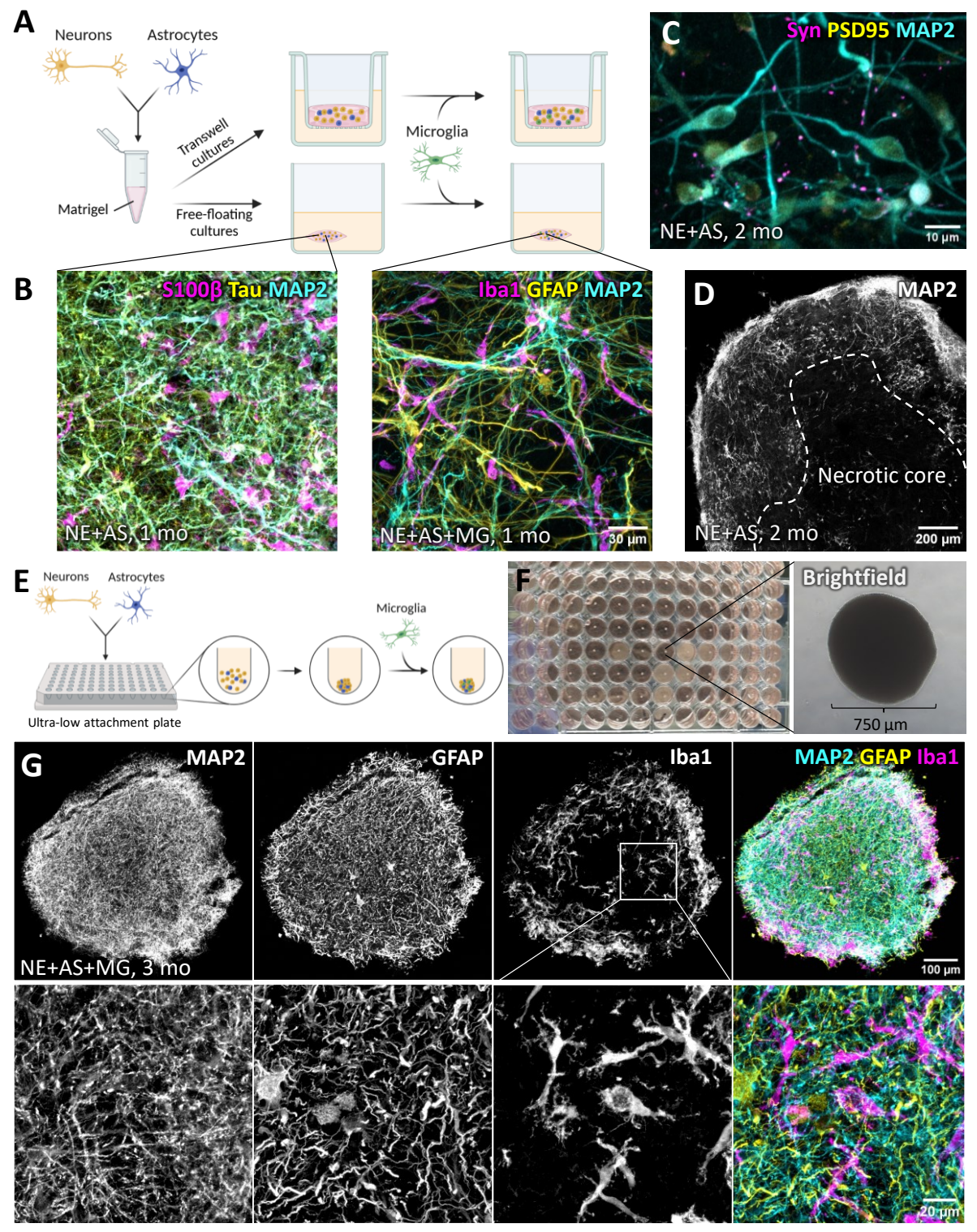


Figure 13: Approaches to generate 3-dimensional (3D) cultures of iPSC-derived brain cell types. A) Generation of 3D cultures by embedding cells into Matrigel. NE and AS were mixed with ice-cold Matrigel and plated into transwell inserts (top) or little droplets to generate free-floating cultures (bottom). MG were added 3 weeks later into the media and migrated into the cultures. B) Left: IF staining of free-floating Matrigel culture with NE and AS after 1 month, cells formed dense networks as seen by Tau and MAP2 staining (NE) and S100β staining (AS). Right: Free-floating culture after incorporation of MG, MG are closely interacting with neuritic (MAP2) and astrocytic (GFAP) processes. C) IF staining shows synapse formation in free-floating cultures at 2 months as seen by colocalization of Synapsin-1 and PSD95. D) Free-floating Matrigel cultures develop a necrotic/dead core at 2 months of age as seen by lack of MAP2 staining. E) Generation of 3BTMs by self-aggregation of NE+AS. Cells are added into ultra-low-attachment wells and aggregate over 4-5 days. MG are added 3 weeks later into the media and migrate into the cultures. F) Left: Overview of a 96-well plate with 3BTMs, note the uniform size and shape of the cultures. Right: Brightfield image of a single 3BTM at 1 month. G) Top: IF staining of a middle slice from a 3BTM at 3 months shows the neuritic (MAP2) and astrocytic (GFAP) network without necrotic core and the distribution of incorporated microglia (Iba1). Bottom: Zoom-in shows fine and dense processes of NE and AS, and ramifications of MG.

3.3. Characterization of 3BTMs

To comprehensively characterize 3BTMs, we performed large time course experiments comparing different combination of cell types – NE only cultures, NE+AS co-cultures, and NE+AS+MG co-cultures. We first analyzed culture size over time to confirm reproducibility and stability of the cultures. Indeed, we found a consistent diameter of around 700-750 µm that was stable over time from 1 week to 6 months of age (Figure 14A), suggesting that the cultures are postmitotic. To confirm this, we performed IF stainings for Ki67, a nuclear protein strictly associated with cellular proliferation ^{256,257}. Although we could detect around 5-15 % Ki67+ cells 3 days after aggregation, the fraction dropped close to 0 % at 1 months and later ages (Figure 14B). This suggests that the DAPT and 5FU treatments worked, leading to largely post-mitotic cultures. Next, we tested for ongoing cell death in the 3BTMs over time. To this end, we performed TUNEL stainings, which marks DNA double-strand breaks ²⁵⁸, a sign of cell death. The percentage of TUNEL-positive and thus apoptotic cells varied depending on the cell types present in the cultures (Figure 14C, E), with the highest percentage in NE cultures (~20 %), followed by NE+AS cultures (~10 %) and NE+AS+MG cultures (~4-5%). In each condition, the values were stable over time from 1 to 6 months of age. This indicates that the additional cell types may create a more physiological environment with more or higher levels of relevant survival factors present, and/or improved clearance of apoptotic and dead cells by astrocytes and microglia. The detected levels were also much lower than in commonly used brain organoids which show around 40 % ²⁵⁹ to 60 % TUNEL-positive cells at 3 months of age ²¹⁶, suggesting strongly improved cell survival in our cultures in comparison.

We next investigated if we could detect increases in maturation markers in the cultures over time. To this end, we first analyzed synapse formation by IF staining for Synapsin-1 and PSD95. We could detect colocalization of both markers, suggesting synapse formation (Figure 14F), that increased over time, showing increased maturation (Figure 14D). In addition, we performed electron microscopy (EM) analysis in collaboration with the Synergy Nanoscale Hub, to analyze synapse formation on an ultrastructural level. In EM, we could detect mature synapses with postsynaptic densities and in some cases also tripartite synapses where pre- and post-synaptic terminals are in touch with an astrocyte (Figure 14K). To assess synapse formation on a more global scale, we performed mass spectrometry experiments (in collaboration with the Synergy Proteome Hub) of 3BTMs at 3 days, 3 months, and 6 months of age. We detected a large variety of synapse-associated proteins in the cultures with a small subset being shown in Figure 14L. Compared to cultures at 3 days, we observed a strong upregulation of almost all synapse markers at 3 months, and a further upregulation of some markers at 6 months of age (Figure 14L), suggesting widespread synapse formation especially during the first months in culture. Besides excitatory synapse markers such as various glutamate receptor subunits (e.g., GRIA1), we could also detect GABA receptor subunits (e.g., GABRA1), suggesting formation of inhibitory synapses in the cultures.

To further look into maturation markers, we analyzed formation of a brain-like ECM in the 3BTMs. The brain ECM is essential for a variety of cellular functions such as network formation and signaling events ²⁶⁰, however, due to its distinct properties, it so far cannot faithfully be recapitulated *in vitro* ²⁶¹. We therefore did not add any exogenous matrix when generating the 3BTMs, but instead hypothesized that we could most closely mimic brain ECM by letting the cells produce their own ECM over time. As indicated above, brain ECM is mainly built of hyaluronan, chondroitin sulphate proteoglycans (CSPGs)

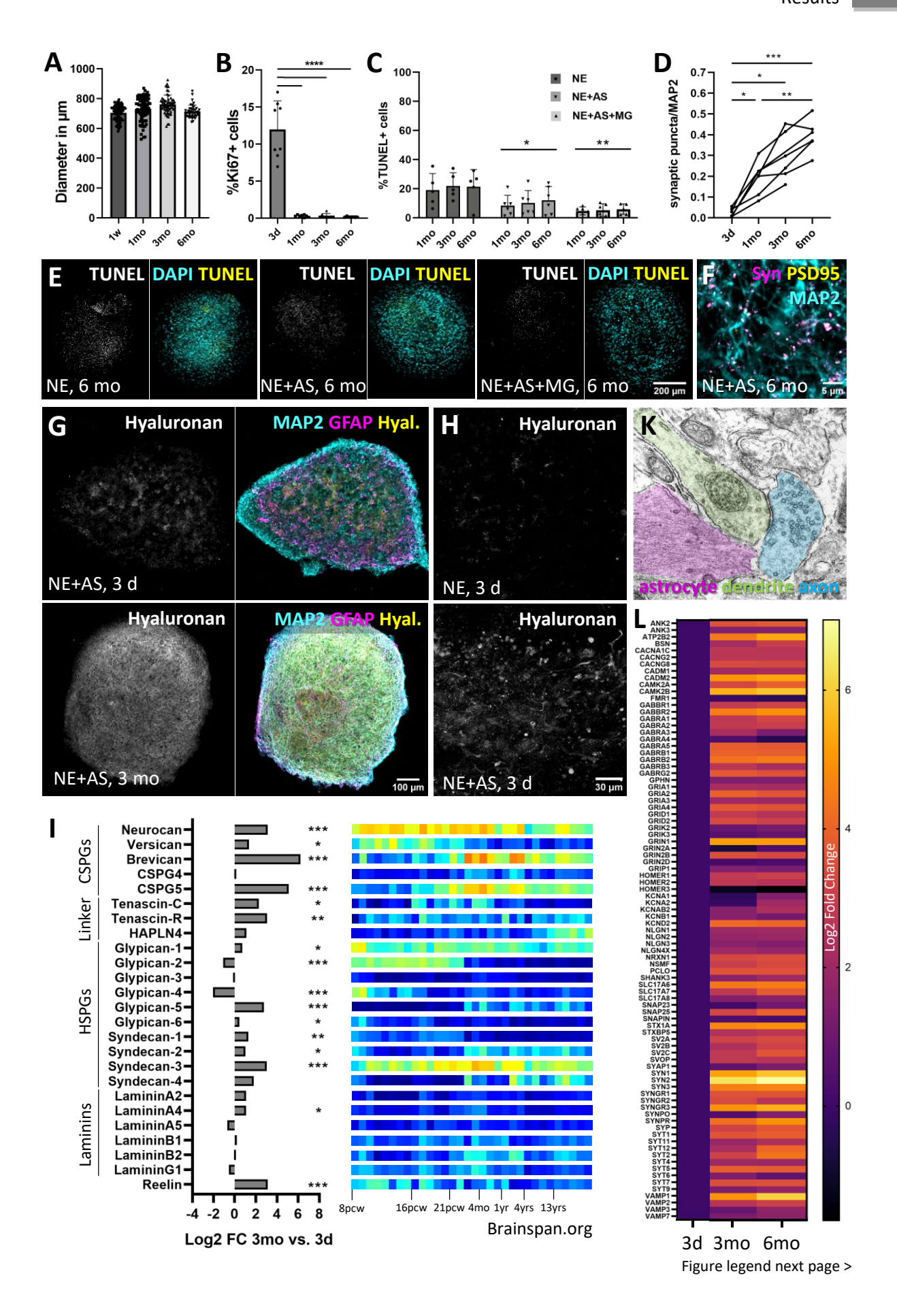


Figure 14: Characterization of 3BTMs. A) Quantification of 3BTM diameter in brightfield images shows reproducible and constant size over time, each dot represents one culture. B) Quantification of Ki67 stainings of 3BTMs shows low levels of dividing cells at 3 days (3d), and almost no dividing cells from 1 month (1mo) onward. Each dot represents one experiment (One-way ANOVA with Dunnett's multiple comparison test). C) Quantification of TUNEL stainings of 3BTMs shows constant rates of cell death over time, and lower rates in co-cultures with AS and MG. Each dot represents one experiment (Mixedeffects model with Geisser-Greenhouse correction to analyze NE+AS vs. NE and NE+AS+MG vs. NE cultures, p = 0.1255 for comparison of NE+AS vs. NE+AS+MG). D) Quantification of synaptic puncta normalized to MAP2 area in NE+AS 3BTMs shows increases in synapses over time. Each line represents one experiment. (Mixed effects model with Tukey's multiple comparison test, p = 0.0767 for comparison 1mo vs. 3mo and p = 0.766 for 3mo vs. 6mo). E) Representative TUNEL and DAPI stainings of 6-month-old NE (left), NE+AS (middle) and NE+AS+MG (right) 3BTMs. F) IF staining of NE+AS culture at 6mo shows colocalization of Synapsin-1 and PSD-95 positive puncta on MAP2-positive neurites. G) IF stainings for Hyaluronan at 3d (top) and 3 mo (bottom) shows strong increase in staining intensity and more homogeneous staining at 3mo. Right pictures show merged images including stainings for NE (MAP2) and AS (GFAP). H) IF stainings for Hyaluronan in NE (top) and NE+AS (bottom) 3BTMs at 3d shows stronger staining in NE+AS cultures. I) Mass spectrometry analysis of NE+AS 3BTMs detected a variety of brain-ECM-associated proteins including chondroitin sulphate proteoglycans (CSPGs), linker proteins, heparan sulphate proteoglycans (HSPGs) and Laminins. Comparison of 3mo vs 3d cultures shows strong increases in most proteins detected (Student's t-tests to compare proteins at 3mo vs. 3d and application of a permutation based false discovery rate (FDR) estimation with FDR = 5 % at s0 = 0.1). Heat maps on the right show corresponding transcriptomic data for each gene over time from human brains, extracted from the BrainSpan database. Note that proteins decreased in 3BTMs at 3mo are also decreased in human brain at older ages, and that genes only expressed around birth are detected in 3BTMs. K) Electron micrograph of a NE+AS+MG 3BTM at 3mo shows formation of tripartite synapses made of presynaptic axon, postsynaptic dendrite, and adjacent astrocyte. L) Heat map showing log2 fold changes in protein levels of a subset of synapse-associated proteins detected in mass spectrometry analysis in 3BTMs over time. Most proteins are strongly upregulated at 3mo compared to 3d, and partially further upregulated at 6mo compared to 3mo. Bar on the right shows color-code.

and heparan sulphate proteoglycans (HPSGs), with Tenascins as linkage molecules and only small amounts of Laminin, Collagen IV, and Fibronectin. We first analyzed deposition of the main component, Hyaluronan, by IF stainings. We could detect small, dispersed amounts already in 3-dayold NE+AS cultures, suggesting that the cells start producing it immediately after aggregation (Figure 14G, top). In comparison, at 3 months of age the staining was stronger and evenly distributed, suggesting deposition in the culture over time (Figure 14G, bottom). Interestingly, we detected much lower levels of Hyaluronan in NE cultures (Figure 14H, top) compared to NE+AS cultures (Figure 14H, bottom) at 3 days, suggesting that Hyaluronan is mainly produced by astrocytes in our cultures. To assess ECM formation and protein levels on a more global scale, we next searched for ECM-related proteins in our mass spectrometry dataset. We detected a variety of brain ECM molecules, including the core proteins of brain-specific CSPGs such as Neurocan, Brevican and CSPG5, typical linkage proteins Tenascin-C, Tenascin-R and HAPLN4, as well as different HSPGs and Laminins. (Figure 14I, left). Comparing 3-month to 3-day-old NE+AS cultures, we could detect large increases in many of the proteins, indicating their deposition as brain-ECM-like structures. We then compared the protein levels and changes to data from the BrainSpan database (Figure 14I, right), which collects data of the human developmental transcriptome ²⁶². In this comparison we could confirm that we cannot only detect continuously high expressed proteins such as Neurocan, but also proteins that are only or more highly expressed after birth in juvenile and adult stages, such as Brevican, CSPG5, HAPLN4, Glypican-5 or Syndecan-4, suggesting that the ECM in the 3BTMs has a postnatal identity. Interestingly, proteins that are increased in 3BTMs at 3 days compared to 3 months, such as Glypican-2 and Glypican-4, are also more highly expressed in the human brain at earlier stages, suggesting a typical remodeling of the ECM in our cultures, with early components being degraded. Overall, the data suggests that a brain-like ECM is formed in the 3BTMs, mimicking changes also seen in human brain development around birth.

After confirming synapse and ECM formation and maturation in the cultures we next analyzed functionality of the neurons. To this end, we first performed wholemount calcium imaging in 3BTMs using Fluo-4. We could detect spontaneous and synchronized calcium waves in NE+AS cultures at 3 months of age (Figure 15A), suggesting functional network formation. To confirm neuronal activity and maturation on a single-cell level, we next performed electrophysiology experiments on acute slices of 3BTMs (in collaboration with Lars Paeger, AG Herms, DZNE Munich). In patch clamp, we could detect

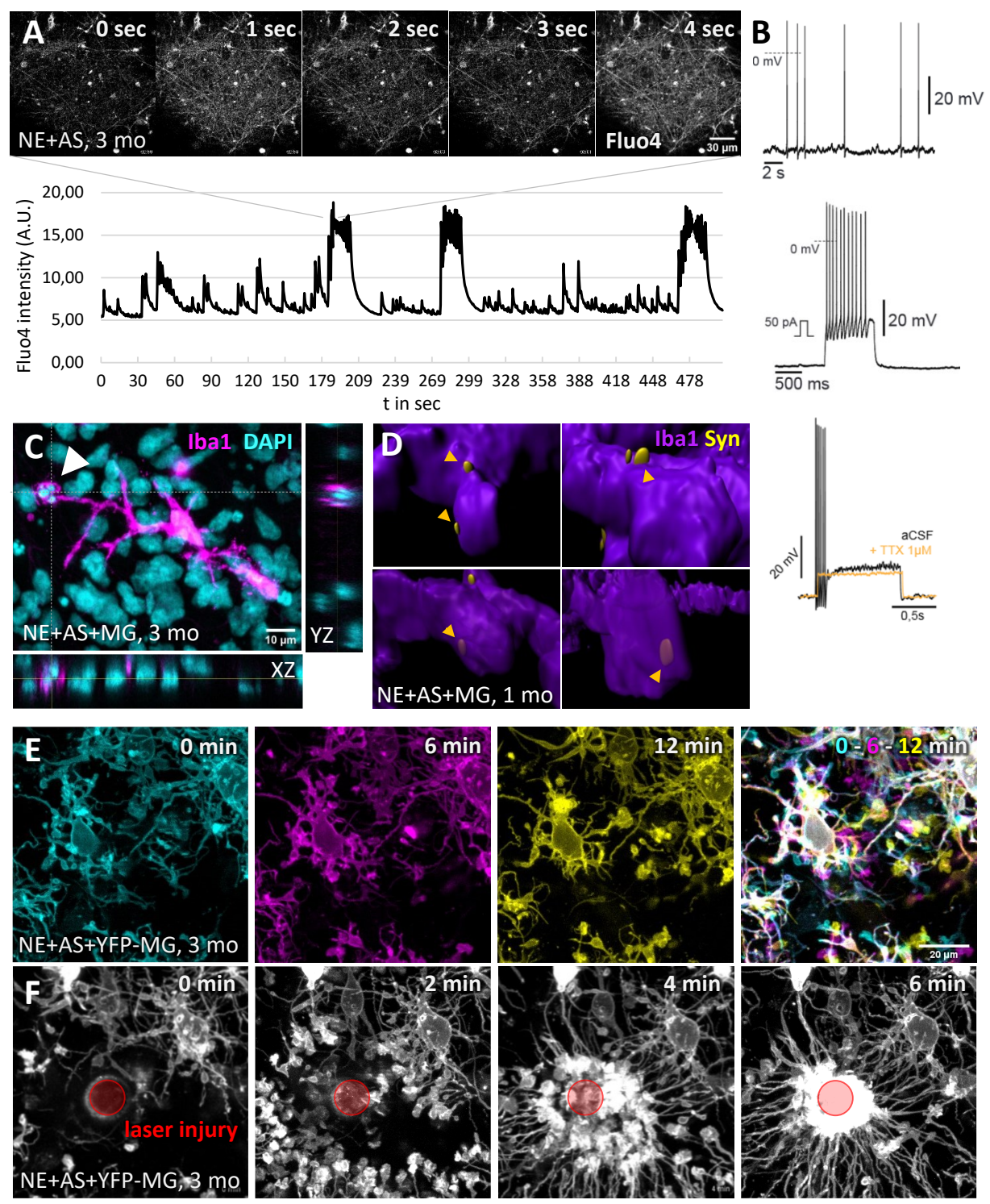


Figure 15: Functional characterization of 3BTMs. A) Top: Live cell calcium imaging using Fluo-4 shows spontaneous and synchronized activity in NE+AS 3BTMs at 3 months. Bottom: Quantification of Fluo-4 intensity over time. B) Patch clamp measurements of single neurons in NE+AS+MG 3BTMs at 6 months shows spontaneous action potentials (top), evoked action potentials (middle) and inhibition of firing after tetrodotoxin (TTX) treatment (bottom). C) IF co-staining for DAPI-positive nuclei and Iba1-positive microglia shows microglial process engulfing a dead cell's nucleus as seen by bright and fragmented DAPI staining, orthogonal projections in YZ and XZ confirm engulfment. D) 3D surface rendering of co-staining for Synapsin-1 (Syn)-positive synaptic material and Iba1-positive microglia shows close association (top) and engulfment (bottom) of synaptic material by microglia. E) 2-Photon live-cell imaging of NE+AS+YFP-MG cultures at 3 months, visible are only YFP-MG. Pictures are shown for different, color-coded timepoints (0, 6, 12 min), merged image on the right shows summary of movements by color-coding as in single timepoints, leading to white staining of stable structures. F) 2-Photon live-cell imaging as in E) shows reaction of microglia to a focal laser injury (red circle), adjacent microglia quickly extend processes towards the lesion site and surround it after 6 minutes.

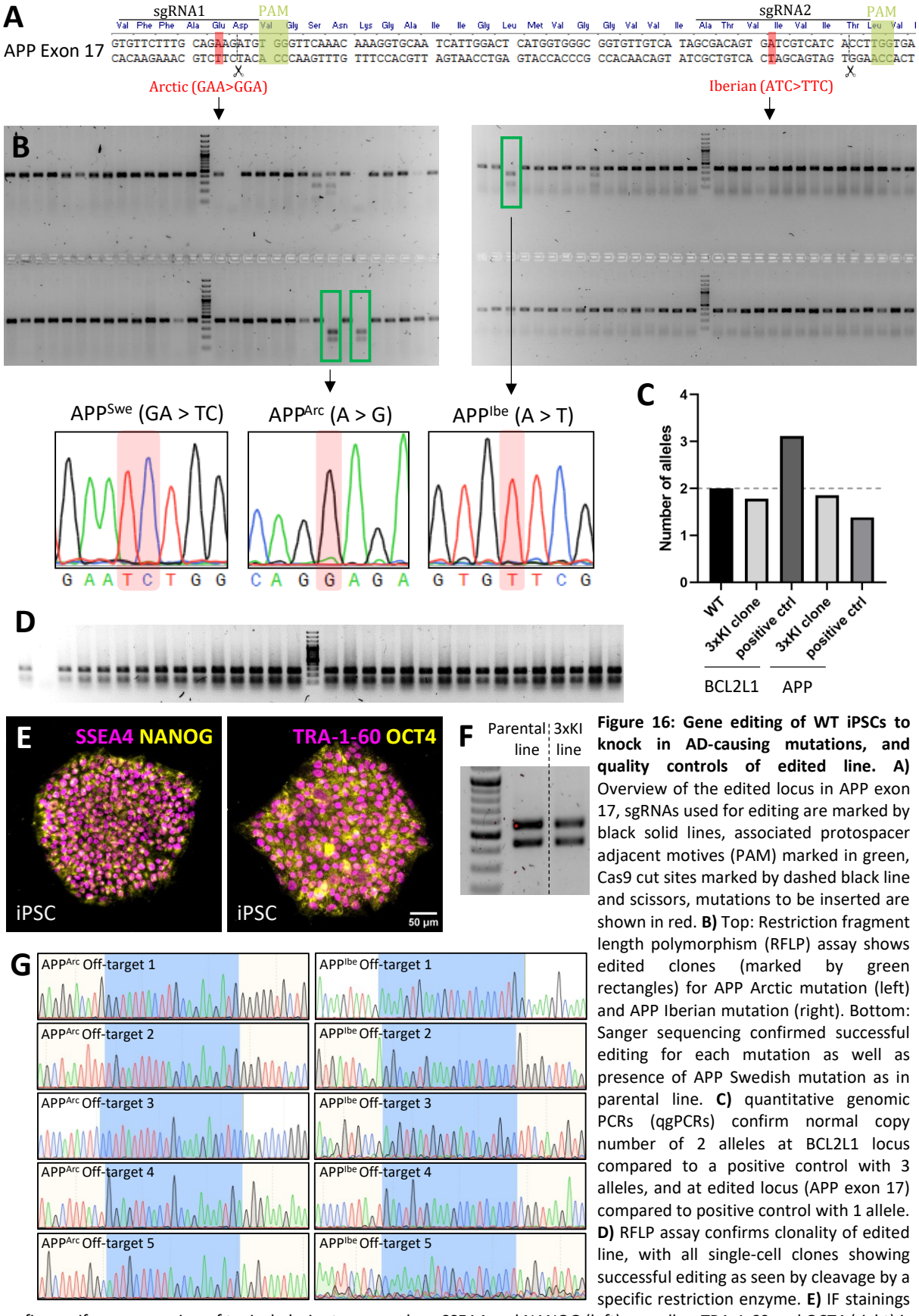
mini EPSPs, mature, spontaneous action potentials (Figure 15B, top), as well as evoked action potentials (Figure 15B, middle), that were sensitive to tetrodotoxin (TTX, Figure 15, bottom), a voltage-gated sodium channel antagonist, suggesting that action potentials are indeed driven by these channels. Altogether these data suggest that the neurons are electrophysiologically mature and functional.

We next investigated microglia functionality. As microglia are phagocytic cells, we first analyzed IF stainings for events that suggested microglial uptake of debris. Indeed, we could detect such events where microglial processes surrounded a likely dead or dying cell as seen by bright and fragmented DAPI staining (Figure 15C). Another essential microglial function is synaptic pruning, where microglia shape neuronal circuits especially during development by engulfment and removal of synapses ²⁶³. In 3BTMs at 1 months of age, we could detect Synapsin-1-positive puncta in direct contact (Figure 15D, top) or inside Iba1-positive microglia (Figure 15D, bottom), suggesting that the cells are indeed able to engulf synaptic material. Finally, we performed live cell 2-photon imaging to visualize microglia behavior in living 3BTMs (in collaboration with Severin Filser, Plesnila Lab, ISD). To this end, we embedded microglia expressing membrane-YFP (YFP-MG, the iPSC line was generated by Liliana Pedro and Carolina Cardoso Gonçalves) into 3BTMs and performed 2-photon imaging 2 months later. Under "resting" conditions, we could detect movements of microglia processes (Figure 15E), suggesting that the cells are surveilling the environment as in the brain. We next inflicted a focal laser injury and monitored the cells reaction. Almost immediately after the injury, all adjacent cell started extending processes towards the lesion site, completely surrounding it after 6-8 minutes (Figure 15F), indicating that the cells did sense danger signals from the injury site and tried to contain the damage.

Together, these data indicate that cells in the 3BTMs do not only express typical markers and mature over time, but also display typical functions found also in brain. Having established and characterized this reproducible, modular, and controllable 3D cortical tissue model, we next applied it to model AD pathology.

3.4. Knock-in of synergistic AD mutations using CRISPR/Cas genome editing

I aimed to knock in (KI) a combination of synergistic, AD-causing APP mutations into WT iPSCs, to induce advanced pathology in experimentally trackable time frames while avoiding overexpression artefacts. I screened the literature for the best combination of mutations and decided on homozygous APP Swedish (APP^{Swe}), APP Arctic (APP^{Arc}), and APP Iberian (APP^{Ibe}) mutations. These mutations have distinct and synergistic effects on AB aggregation by increasing total AB levels, accelerating AB protofibril formation and thus aggregation, and increasing Aβ42:40 ratio, respectively. Confirming the strong effects on Aβ production and metabolism, the NL-G-F mouse model ¹⁰⁰, that carries a knock-in of the same mutations, shows plaque deposition starting at 2 months of age, a well trackable time frame. A KI iPSC line carrying the APP^{Swe} mutation and the isogenic wildtype (WT) line were already established by Dominik Paquet and published earlier ¹⁵⁴. I therefore used this APP^{Swe} line as a basis and additionally knocked in APPArc and APPIbe mutations using the CRISPR/Cas9 gene editing system. First, I searched for sgRNAs close to the mutations using the CRISPOR online tool (http://crispor.tefor.net/) ²³⁶. A panel of sgRNAs was selected, cloned into an expression vector, and tested in HEK293 cells for activity. The best sgRNA for each mutation was chosen based on activity, mutation-to-cut distance as well as efficiency and specificity scores and used for genome editing in iPSCs. Both APP^{Arc} and APP^{lbe} mutations are located in Exon 17 of the APP gene with a distance of 69 base pairs (bp) (Figure 16A). Initially, I tried to insert both mutations at the same time by simultaneously providing both sgRNAs, inducing 2 cuts and providing a large repair template carrying both mutations. This approach was extremely inefficient, yielding only one out of 2500 screened clone that carried both mutations as seen by restriction fragment length polymorphism (RFLP) analysis. This clone however



confirm uniform expression of typical pluripotency markers SSEA4 and NANOG (left) as well as TRA-1-60 and OCT4 (right) in edited line. **F)** Fingerprinting PCR confirms descent of edited line from parental line by same band pattern. **G)** Sanger sequencing around top 5 off target sites for each mutation (as predicted by CRISPOR online tool) shows no off-target editing at these loci.

did not carry the APP^{Swe} mutation when analyzed by Sanger sequencing, suggesting it was derived from a WT cell contamination. Therefore, I changed the approach and aimed to insert the mutations one by one. This method was much more efficient, yielding approximately 6 % positive clones for the APP^{Arc} and 1 % positive clones for the APP^{Ibe} mutation as seen by RFLP analysis (Figure 16B, top) and resulting in a clone carrying both mutations homozygously in addition to the APP^{Swe} mutation (sequencing traces for each mutation in Figure 16B, bottom).

3.4.1. Quality controls of the established APP triple knock-in line

The triple KI (KI) clone was further expanded and subsequently subjected to quality controls. First, a qPCR assay on the genomic DNA (qgPCR) at the BCL2L1 locus was performed to prescreen clones for a local trisomy of this gene, a common genomic variation found in iPS cells ²⁶⁴. BCL2L1 encodes an antiapoptotic protein and a triplication of the locus would thus improve cell survival and give the cells a growth advantage ²⁶⁵, making it detrimental for reliable disease modeling. The assay confirmed that the KI clone has two copies of the BCL2L1 gene (Figure 16C). Next, another qgPCR assay was performed around the edited locus (APP exon 17) to exclude unwanted on-target effects that can occur during editing and are not visible in Sanger sequencing ²⁶⁶. Again, the assay confirmed a normal copy number of the locus of 2 (Figure 16C). To confirm clonality of the new line regarding the inserted mutations, I analyzed 30 colonies derived from single cells of the line by RFLP assay around the edited locus, and all showed the same, correct band pattern (Figure 16D). Next, I performed immunostainings for the presence of common pluripotency factors NANOG, SSEA4, OCT4 and Tra-1-60, to ensure that CRISPR editing did not affect pluripotency of the iPSCs. As expected, NANOG and OCT4 were expressed in the nucleus and colocalized with DAPI, whereas markers SSEA44 and Tra-1-60 were expressed in the cytoplasm and membrane (Figure 16E). To check whether the clone was derived from the correct parental line, a fingerprinting PCR was performed, which confirmed that the edited KI line showed the same band pattern as the parental line (Figure 16F). Next, the edited cell line was screened for the top five off-target editing events according to the CRISPOR online tool by PCRs around the off-target loci followed by Sanger sequencing. All sequencing traces showed clear, single peaks, excluding unwanted editing events at these loci (Figure 16G). Finally, the KI line was subjected to molecular karyotyping ²³⁸, and no additional chromosomal aberrations were found compared to the WT line. Therefore, I could establish a human iPSC line carrying three synergistic APP mutations, APP^{Swe}, APP^{Arc} and APP^{Ibe}, that I next characterized regarding the development of AD-related phenotypes and underlying pathomechanisms in 3BTMs.

3.5. AD phenotypes in knock-in 3D cultures

3.5.1. Aß production and accumulation

As a first step, I analyzed if the inserted mutations indeed caused the desired alterations on APP processing and A β generation. To this end, WT and KI iPSCs were differentiated into NE, AS and MG as described above and aggregated into 3BTMs. After 1, 3 and 6 months, the culture media was conditioned for 5 days, collected, and used for electrochemiluminescence analysis on an MSD A β peptide array to detect secreted A β 38, 40, and 42 in each genotype. As expected from the APP^{Swe} mutation, KI cells showed increased total A β levels compared to WT cells (Figure 17A, left). In addition, the A β 42:40 ratio was about 50-fold increased (Figure 17A, right), confirming the effect of the APP^{Ibe} mutation. There were no differences detected between the different timepoints. Analyzing the single A β species, the increase in the A β 42:40 ratio stems from both an increase in A β 42 as well as a decrease in A β 40 levels (Figure 17B), indicating a shift in processing to longer, more aggregation prone species. However, I could also detect a strong upregulation of A β 38 levels, making A β 38 the dominant A β 5 species secreted by the cells (Figure 17B). I next analyzed if the secreted A β 6 levels are changing upon co-culture with AS and/or MG. To this end, I generated KI 3BTMs of the different cell type combinations

– NE only, NE+AS, and NE+AS+MG, and analyzed A β production in each condition over time. I could not detect any significant changes in the co- compared to mono-cultures (Figure 17C), suggesting that A β production is not significantly influenced by the presence of the other cell types. I could also confirm the strong upregulation in A β 38 levels in this dataset, which has not been described before in the corresponding mouse model. Therefore, to investigate if this increase is caused by the APP^{Arc} or APP^{Ibe} mutation, we analyzed supernatants from cells carrying only one of the two mutations in addition to the APP^{Swe} mutation. This was done by Merle Bublitz, a M.Sc. student in the lab that I supervised. Merle could show that A β 38 was upregulated in cells carrying either mutation, with a stronger effect of APP^{Ibe}, and a synergistic additional increase if both mutations are present (Figure 17D), indicating that both mutations increase A β 38 by independent mechanisms.

I next performed immunofluorescence (IF) stainings to investigate if the produced A β would be deposited in the cultures and if plaque-like structures would be forming over the course of 6 months in KI 3BTMs. I indeed observed progressive accumulation of A β -positive puncta/structures (Figure 17E) specifically in KI cultures over time (Figure 17F), indicating focal accumulations which may represent early stages of plaque formation. Interestingly, this effect did depend on the cell types present in the cultures. In NE cultures I only found a small increase from 1 month to 3 months followed by a plateau up to 6 months (Figure 17G, left), while in NE+AS cultures, and to a greater extent in NE+AS+MG cultures, I could detect an accumulation over time (Figure 17G, left). This led to significant increases in the number of A β -positive puncta/structures in co-cultures compared to NE monocultures at 6 months of age (Figure 17G, right). However, I did not observe dense A β aggregates or the formation of mature plaques, which would be characterized by a larger size and aggregated core, in KI 3BTMs in the time frame studied.

To analyze if we could detect any insoluble/aggregated A β in 3BTMs biochemically, I next performed sequential protein extractions from 3BTMs over time. I extracted soluble and extracellular protein in a DEA-based buffer (DEA fraction), followed by extraction with RIPA buffer (RIPA fraction) to break residual membranes and organelles, as described ²⁶⁷, leaving only insoluble proteins that were further extracted with a Guanidine thiocyanate buffer (Gua fraction) ²⁶⁸. Indeed, using the MSD assay described above, I could detect insoluble A β 42 in the Gua fraction of NE+AS+MG KI cultures at 1 month and larger amounts at 6 months, and significantly more in KI compared to WT cultures (Figure 17H). This suggests that insoluble A β 42 accumulates, especially in the KI cultures, over time. Interestingly I could not reliably detect A β 38 in the insoluble fraction, despite the larger secreted levels compared to A β 42. This can be explained by the higher aggregation potential of A β 42 and its subsequent faster accumulation into insoluble forms.

3.5.2. Effect of APP triple KI on phospho-Tau levels

To analyze downstream pathology of the increased A β production and accumulation, we performed western blot analysis of 3BTM lysates at different timepoints. As according to the amyloid cascade, A β accumulation or aggregation is inducing Tau hyperphosphorylation, we first used the AT270 antibody to examine levels of phospho-Thr181 (pThr181), an epitope also used as biomarker for early AD pathology in humans. At 3 months of age, we could detect a significant increase in pThr181 in KI NE+AS+MG cultures compared to WT (Figure 17I, left). This effect was not visible in NE+AS cultures at the same age (Figure 17I, middle), potentially hinting towards microglial involvement in increasing pTau levels, or a connection with the slightly higher levels of A β accumulation in cultures with MG seen in Figure 17G. We also analyzed NE+AS+MG cultures at 6 months of age and found a similar increase as at 3 months (Figure 17I, right). This could indicate that the progressing A β accumulation does not induce further Tau phosphorylation at this epitope. Alternatively, this could be explained by a reduction in microglia numbers within the cultures that we observed in some experiments between 3

and 6 months of age, as microglia may be needed to increase pTau levels, as described above. As an additional tauopathy marker, we used the PHF1 antibody, which recognizes misfolded, paired-helical filament Tau. We found an upward trend for PHF1 at 3 months and at 6 months in KI NE+AS+MG cultures, but the increase did not reach significance in the small sample size analyzed (Figure 17K).

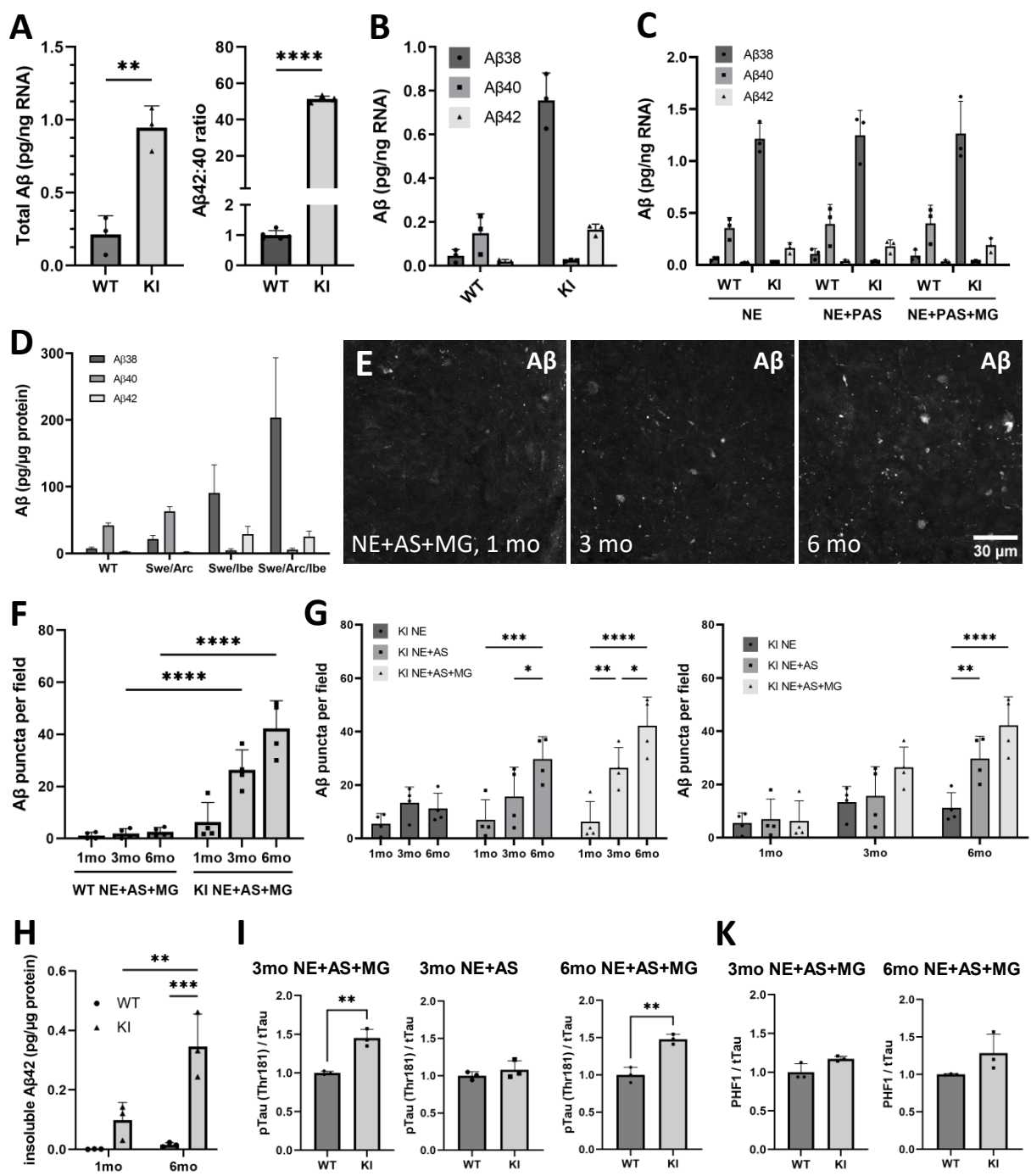


Figure 17: AD phenotypes observed in triple KI (KI) cultures. A) Electrochemiluminescence immunoassay (ECL-IA) of culture supernatants at 1 month to measure secretion of Aβ38/40/42 shows increased total Aβ levels (left, sum of all 3 species) and increased Aβ42:40 ratio (right) in KI cultures (unpaired t-tests). B) ECL-IA as in A) showing individual Aβ species in supernatant of 1-month-old WT vs. KI cultures. Note strong upregulation of Aβ38, downregulation of Aβ40 and upregulation of Aβ42 in KI cultures. C) ECL-IA to detect Aβ38/40/42 in supernatant of 1-month-old WT and KI cultures containing different cell types shows no significant difference. D) ECL-IA of supernatants from WT cultures and cultures carrying different combinations of AD-causing mutations indicate an increase in Aβ38 in cells with either APP^{Arc} or APP^{Ibe} mutation in addition to the APP^{Swe} mutation, and a synergistic further increase when all mutations are present. Aβ40 slightly increases with APP^{Arc} mutation and decrease with APP^{Ibe}. Aβ42 increases with APP^{Ibe}. Data from Merle Bublitz. E) IF staining of KI NE+AS+MG cultures over time shows accumulation of Aβ. F) Quantification of IF stainings in D) and comparison to WT 3BTMs shows accumulation in KI cultures (Two-way ANOVA with Šidák's multiple comparisons test).

Figure legend continued: G) Quantification of IF stainings as shown in D) of KI cultures with different cell type combinations (NE vs. NE+AS vs. NE+AS+MG). Left) Comparison of each cell type combination over time shows significant increase in A β accumulation in NE+AS and NE+AS+MG cultures, but not in cultures containing only NE. Right: Comparison of different cell type combinations at the same timepoints shows significantly more A β accumulation in NE+AS and NE+AS+MG cultures compared to NE cultures at 6 months of age and increasing trends in NE+AS+MG compared to NE+AS cultures at 3 and 6 months (Two-way ANOVA with Tukey's multiple comparisons test, p = 0,148 for NE+AS vs. NE+AS+MG at 3mo and p = 0,082 at 6mo). H) ECL-IA of insoluble fractions extracted from WT and KI 3BTMs shows insoluble A β 42 in KI cultures at 1 month and further accumulation at 6 months (Two-way ANOVA followed by Tukey's multiple comparisons test). I) Western blot analysis of WT and KI cultures shows increased Tau phosphorylation at Thr181 using the AT270 antibody at 3 months of age in NE+AS+MG (left), but not NE+AS cultures (middle). pThr181 is also increased at 6 months in NE+AS+MG cultures (unpaired t-tests). K) Western Blot analysis of WT and KI cultures using the PHF1 antibody to detect paired helical filament (PHF) tau. No significant differences were found at 3 or 6 months in NE+AS+MG cultures. (Unpaired t-tests, p= 0,056 at 3 months and p = 0.121 at 6 months). For all graphs, each dot represents one experiment.

Altogether, the model recapitulates increased pTau levels at an epitope affected early in AD (Thr181), specifically in cultures containing all three cell types, while only a trend is visible for changes in PHF1-Tau as a later marker of AD tauopathy, which correlates with the observed early amyloidosis phenotypes.

3.5.3. Analysis of global disease-associated alterations using transcriptomics

I next aimed to assess the cellular changes in KI compared to WT cultures on a more global scale using transcriptomics. Transcriptomics allows for the analysis of all RNA transcripts in a cell population (bulk RNA sequencing) or in single cells (single-cell RNA sequencing). It can thus elucidate changes in expression patterns in a more unbiased way compared to classical techniques such as qPCRs which are limited to predefined sets of genes. For this project, I wanted to assess the effect of increased AB production and accumulation on the cell's transcriptomes and especially on microglia in KI compared to WT cultures. As we only detected spatially limited amyloid pathology, we decided to use single-cell RNA sequencing, as potentially subtle changes in single microglia close to the pathology may be masked in bulk RNA sequencing. We performed a first, preliminary single-cell RNA sequencing experiment comparing WT and KI NE+AS+MG cultures in collaboration with the Synergy Transcriptome Hub at AG Beltrán (Biomedical Center, LMU Munich). Although the number of cells retrieved and analyzed from the cultures was relatively low, we found all 3 cell types represented in the dataset (Figure 18A), albeit in different proportions compared to the ratio we added to the cultures. Neurons and especially astrocytes were underrepresented, with 34 % and 3 % of the cells, respectively, while microglia were overrepresented with 63 % of the cells. This is likely due to cell death or incomplete dissociation especially of NE and AS which are part of a dense network, while MG are not incorporated into a network and thus more easily extracted from the cultures. In our preliminary experiment, we could detect one astrocyte cluster, two different clusters of NE and five different clusters of microglia, suggesting that there is a variety of microglial states even in this small sample. When comparing the distribution of MG per cluster between WT and KI, we found that cluster 4 almost exclusively contained cells derived from KI cultures (Figure 18B), indicating that these may be cells that react to the amyloid pathology. We next analyzed which transcripts define this cluster compared to the other MG clusters, and found a number of genes that overlapped with the human-specific, AD-related signature found by Mathys et al., including CD14 and C1QB ¹²⁴ (Figure 18C). If this finding holds true in a larger experiment, it may indicate that although the 3BTMs display only mild amyloid pathology, we can recapitulate microglial reactivity and that this induces a signature that partially overlaps and may be the precursor state of the MG signature found in post-mortem human AD brains.

Together, we could detect all cell types present in the cultures in this preliminary scRNA sequencing experiment and found a variety of microglial clusters, one of which seems to be strongly enriched in KI cultures, although there is no mature amyloid plaque pathology present. Therefore, the microglial reaction we observed, if confirmed in larger experiments, is likely an early event in pathogenesis.

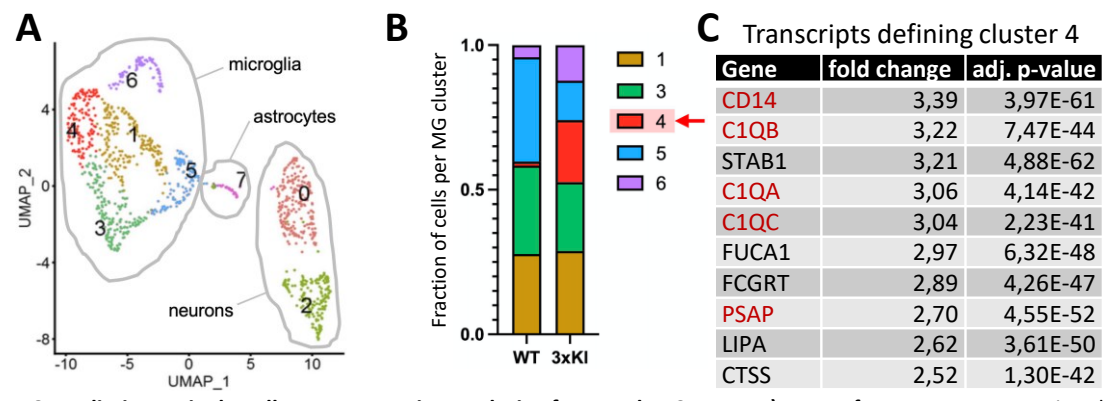


Figure 18: Preliminary single-cell RNA sequencing analysis of WT and KI 3BTMs. A) UMAP from scRNA sequencing data of 3BTMs shows different cell types and subclusters, especially of microglia, indicating successful application of the method and different cell states found in the cultures. **B)** Distribution of cells in each microglia-annotated cluster in WT vs. isogenic KI AD cultures, note increase of cluster 4 in KI. **C)** Top 10 differentially expressed genes defining cluster 4 with fold change increase and adjusted p-value, red genes overlap with human AD signature described by Mathys et al. ¹²⁴ and are absent in mouse DAM signature.

In a last set of experiments, I then aimed to elicit advanced amyloid pathology and mature Aß plaque formation, to promote possible downstream events, including widespread neuroinflammation, advanced tauopathy phenotypes and synaptic and neuritic degeneration.

3.5.4. Effect of disease-modifying and external factors on AB plaque formation

As mentioned above, the NL-G-F mouse model, which carries the same mutations as our cells, forms diffuse A β plaques starting at 2 months of age ¹⁰⁰. In comparison, we detected focal A β accumulations starting at 3 months, but no large, diffuse plaques as in the mice. We therefore first aimed to elucidate the possible causes for this discrepancy in A β deposition in the *in vivo* versus *in vitro* system, to be able to improve our system accordingly. We reasoned that, as our 3BTMs are not a closed system, a lot of the produced AB may diffuse out of the culture, resulting in a concentration within the culture that is not reaching the threshold to start the aggregation process. I therefore did a test experiment to compare total AB amounts in the supernatant to amounts within the cultures used to condition the supernatant. I found that there is indeed 50 to 150-fold more A β in the supernatant than within the cultures (Figure 19A). The numbers varied between the different species, with longer species Aβ40 and especially Aβ42 having a lower ratio of Aβ(supernatant):Aβ(culture), implying that they are being more retained within the culture. In addition, there may be a time-dependent effect for Aβ42, with more of the peptide being retained in the culture with increasing age, again indicating that it accumulates within the cultures over time as described above. By estimating the culture volume, I could also approximate the Aβ concentration in supernatant versus lysate and found a 5 (for Aβ38 at 1month) to 15-fold (for Aβ 42 at 6 month) higher concentration within the cultures, suggesting that there is a strong concentration gradient driving the diffusion of the peptide out of the culture. Although the data should be reproduced in independent experiments, this suggests that diffusion of Aß into the supernatant and thus too low peptide concentrations within the culture may be a major caveat that prevents large-scale aggregation in the 3BTMs compared to the mouse model. The data also indicated a time-dependent effect, with more Aβ42 accumulating in the cultures with increasing age.

Therefore, to induce $A\beta$ plaque formation in 3BTMs, I first tested extended culture periods of up to 11 months. As there was an accumulation of $A\beta$ visible over time, we hypothesized that the amount may not be enough at 6 months to reach the concentration needed for dense aggregation, but may further increase over time. At 11 months we could detect a possible further increase in $A\beta$ -positive puncta and neurite-like structures (Figure 19B, left), suggesting progressive amyloid pathology, and a continuously dense neural network (Figure 19B, right). However, the observed structures were still smaller than classical $A\beta$ plaques and lacked concomitant phenotypes such as dendritic damage or degeneration.

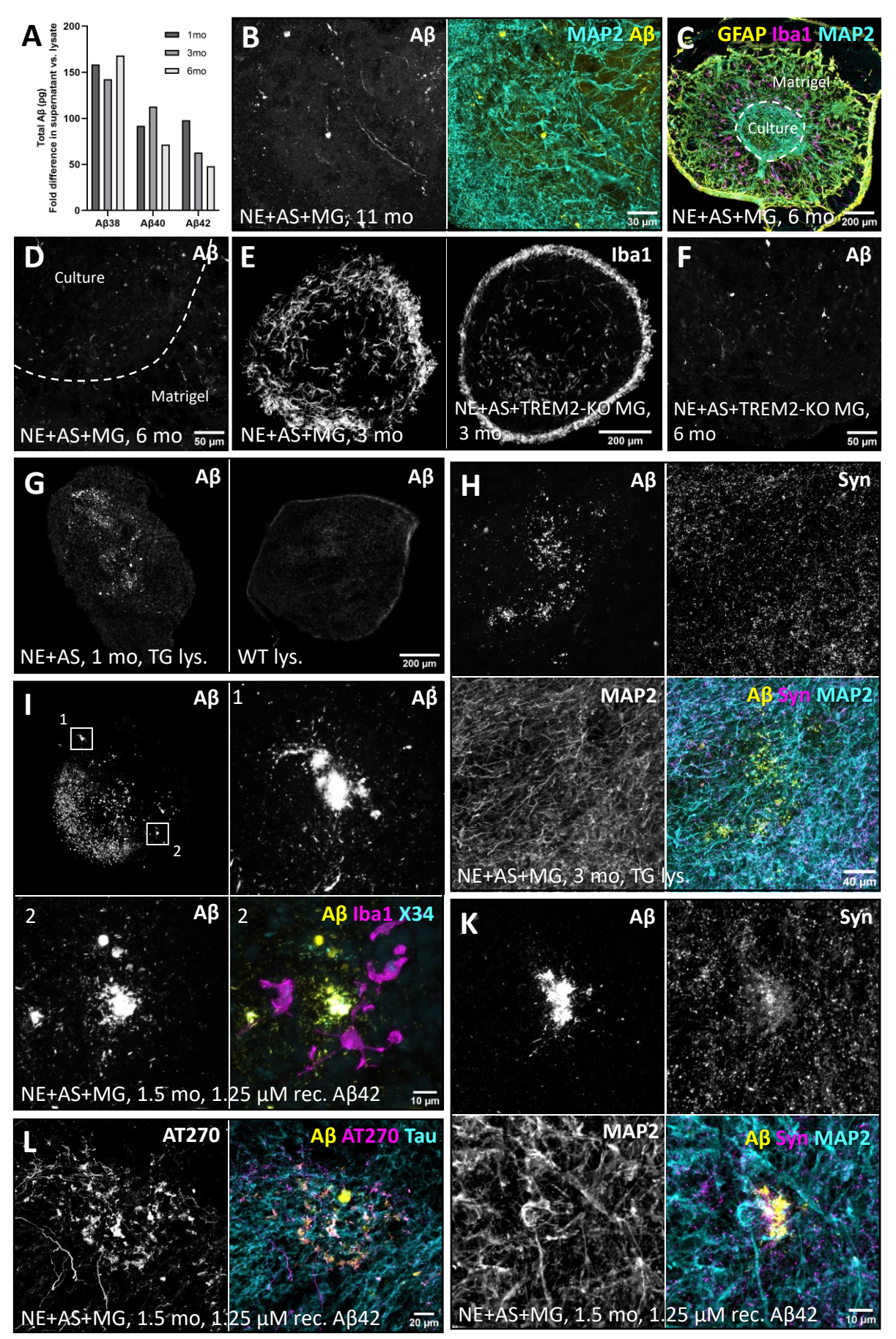


Figure legend next page >

Figure 19: Approaches to induce plaque formation in 3BTMs. A) Preliminary ECL-IA comparing total Aβ levels in supernatant and lysate of cultures used to condition supernatant shows higher levels in supernatants, suggesting most of the produced Aβ is diffusing out of the cultures. B) IF stainings of KI 3BTMs at 11 months shows Aβ accumulation in puncta and neurite-like structures (left) and a dense neural network at this advanced age, but no plaque-like structures or neuritic damage. C) IF staining of KI 3BTM embedded into Matrigel for 5 months. Original culture area indicated by dashed line. Note the outgrowth of NE and AS from the original culture into the Matrigel and almost complete migration of MG from the culture into the Matrigel. D) IF staining of KI 3BTM embedded into Matrigel for 5 months shows Aβ accumulations inside the culture area, but no plaque-like structures. E) IF staining of KI NE+AS+MG cultures (left) and NE+AS+TREM2-knockout (KO) MG (right) shows altered distribution of TREM2-KO MG. F) IF staining for Aβ in NE+AS+TREM2-KO MG KI cultures at 6 months of age shows Aβ accumulations but no plaque-like structures. G) IF staining of NE+AS KI cultures seeded with APP/PS1 transgenic (TG) mouse brain lysate (left) or WT mouse brain lysate (right). Note bright Aß staining in 3BTMs seeded with TG lysate, indicating successful incorporation of the material. H) IF staining of KI culture seeded with TG mouse brain lysate at 3 months shows Aβ-positive, seeded material (top left), but no effect on synapses (top right) or neurites (bottom left). I) IF staining of KI cultures seeded with recombinant, human Aβ42 shows successful incorporation of seeded, strongly Aβ-positive material and formation of plaque-like structures after 1 month (small squares 1 and 2 - zoom-in on top right and bottom left). Plaque-like structures are positive for X34 and partially surrounded by microglia (bottom right). K) IF stainings of seeded cultures as in H) shows possible accumulation of synaptic material (top right) within plaque-like structures (top left), but no dendritic degeneration (bottom left). L) IF stainings of seeded cultures as in H) shows accumulation of pTau and increased pTau levels around aggregated $A\beta$, indicating axonal dystrophy.

Next, I tried to limit diffusion of produced A β out of the 3BTMs and promote aggregation of the peptide by embedding the cultures into droplets of Matrigel. To this end, I embedded 3BTMs at 1mo of age into Matrigel, and analyzed the cultures at 6 months of age using IF stainings. Most strikingly, staining for the different cell types present in the culture showed that the cells grew into the Matrigel over time (Figure 19C). This was apparent especially for astrocytes and microglia, with almost no microglia being left in the original culture, but all of them distributed in the Matrigel portion. This may be due to the growth factors present in the Matrigel which attracted outgrowth of neurons and astrocytes and potentially migration of microglia. Stainings for A β did not show any significant difference to cultures not embedded into Matrigel and no mature plaque-like structures (Figure 19D). I therefore did not follow this approach further.

I then examined the effect of AD risk factor TREM2 on plaque formation, as a recent study showed an increase in amyloid seeding upon loss of TREM2 240 . I therefore focused on the study of TREM2-KO cells and especially TREM2-KO microglia, as neurons and astrocytes do not express the protein. TREM2-KO iPSCs were generated by Sophie Robinson, another PhD student in the group. I differentiated the iPSCs into microglia and incorporated the cells into KI 3BTMs. In IF stainings, I could observe an altered distribution of the cells, with TREM2-KO more localized at the edge of the cultures (Figure 19E, right) compared to an even distribution of KI microglia (Figure 19E, left). This may hint towards an impaired migration and/or chemotaxis of the cells into the cultures, similar to previously observed phenotypes in TREM2-KO microglia 269,270 . However, again no effect on A β deposition was visible at 6 months of age (Figure 19F).

Finally, I tested seeding approaches to accelerate plaque formation by providing pre-aggregated peptides to which endogenously produced A β could bind. As we did not have access to human AD-brain-derived A β , I first tested seeding with brain extract from a transgenic AD mouse model (APPPS1 mice 240). As the material was whole-brain lysate, I compared it to exposure to wildtype mouse brain lysate produced the same way. The cultures seeded with transgenic (TG) AD mouse brain lysate showed strong, punctate staining for A β (Figure 19G, left) compared to cultures treated with WT brain lysate (Figure 19G, right), suggesting that the treatment itself worked and the lysate was incorporated into the 3BTMs. However, we did not observe progressive accumulation of endogenous A β on/around these seeded aggregates (Figure 19H, top left) nor any synaptic (Figure 19H, top right) or neuritic pathologies (Figure 19H, bottom left) around aggregates compared to other areas. In addition, the extract did not only contain A β , but all other factors present in the mouse brain, introducing a lot of exogenous, mouse-derived material into the cultures. To test a more clean and defined approach, I

next tested seeding with commercially available, human recombinant A β 42. A recent publication showed that this leads to rapid aggregation of A β and subsequent synapse and neuron degeneration in 2D cultures ²⁷¹. After addition of the recombinant A β 42 into the media of our 3BTMs, we indeed observed a concentration-dependent aggregation into fibrillar material after 1 month. In cultures treated with 1.25 μ M A β 42, we observed not only large amounts of A β inside the cultures (Figure 19I, top left), but also the formation of plaque-like structures (Figure 19I, top right and bottom left). These structures had a dense core positive for X34, a dye binding to aggregated β -sheet structures found in amyloid plaques, and were surrounded by a halo of A β and in some cases potentially by microglia (Figure 19I, bottom right). This was however observed not only in KI, but also WT cultures. Co-stainings with synaptic marker Synapsin-1 showed potential accumulation in or around plaque-like structures (Figure 19K, top left and top right), but no synaptic or dendritic degeneration (Figure 19K, top right and bottom left) at this early timepoint. However, when we analyzed downstream tau pathology by staining for pThr181 in seeded cultures, we could observe increased pTau levels and pTau accumulations around aggregated, A β -positive structures (Figure 19L), indicating effects of the aggregates on surrounding neurons and possibly axonal dystrophies.

In summary, we could elicit the formation of plaque-like structures in the 3BTM after seeding with recombinant human A β 42. However, the used approach also leads to A β aggregation in WT cultures, suggesting that mainly exogenous material aggregates at this point. Therefore, more optimizations are necessary to find an A β concentration or experimental paradigm that elicits aggregation and plaque formation specifically in KI cultures by incorporation of endogenous A β . Further analysis is also needed to assess the development of downstream pathologies, such as advanced tau pathology, synapse and neurite degeneration, over time.

4. Discussion

Alzheimer's disease is the most common cause of dementia affecting millions of people around the world, but development of mechanism-based treatments has been highly difficult and fundamental pathomechanisms remain poorly understood. iPSC-based AD models enable investigation of these mechanisms in human, disease-relevant brain cell types and thus offer great potential for mechanistic and translational studies. However, current iPSC-AD models often show low reproducibility and are hardly controllable, such as organoids, lack cell types crucial in AD pathogenesis, such as microglia, or miss physiological human cell-cell and cell-matrix contacts, as for 2D cultures.

Therefore, the overall objective of this thesis was the generation of a reproducible and controllable, human iPSC-based cortical tissue model, its characterization, and the analysis of its potential for modelling AD.

We first adopted and optimized protocols to differentiate disease-relevant brain cell types from iPSCs, including cortical neurons, astrocytes, and microglia. We then developed an approach to generate modular 3D cortical brain tissue models (3BTMs) by aggregation of the differentiated cell types into 3D spheres using ultra-low attachment plates. Our 3BTMs have several advantages compared to currently used iPSC 3D models such as organoids. These include:

- 1) high reproducibility regarding size, overall morphology, and cell type composition
- 2) high efficiency of culture generation with almost 100% of generated cultures available for experiments
- 3) modularity, allowing for the analysis of cell-type-specific disease contributions by including or omitting cell types or using only specific cell types carrying a mutation or risk allele
- 4) a post-mitotic state without proliferative rosettes, leading to a uniform cell age and constant culture size over long periods of time, avoiding formation of a necrotic core in the center of the cultures
- 5) fully brain-parenchyma-like cultures, mimicking mature cortical tissue
- 6) efficient incorporation of ramified microglia that tile the cultures, and the possibility to include additional cell types such as oligodendrocytes and vascular cell types, making the model more physiological
- 7) low levels of cell death, especially in co-cultures of neurons, astrocytes, and microglia, enabling studies on neurodegenerative phenotypes
- 8) fully human model without exogenous or animal-derived components, minimizing the number of variables that may influence cell function and phenotype formation.

Together, these properties make the 3BTMs more physiological, controllable, and reproducible compared to other models and thus increase their suitability for the analysis of cellular functions and interactions in health and disease and potential drug screening approaches.

We show that NE and AS in our cultures form a morphologically dense network that is tiled by ramified microglia. The cells produce their own, brain-like ECM over time, following human brain development as seen by comparison with the BrainSpan database. This comparison also indicated that the ECM in mature 3BTMs resembles that of juvenile to adult stages, which may be relevant for recapitulating extracellular disease pathologies, such as protein aggregation. Neurons form functional synapses over time, as seen by colocalization of pre- and post-synaptic markers, spontaneous calcium waves and electrophysiological measurements. Integrated microglia remove cellular debris from the cultures, engulf synaptic material, are actively surveilling the environment under resting conditions and react to stimuli such as a focal laser injury by directed extension of processes towards the lesion site.

We further established an AD model by knock-in of three synergistic, homozygous mutations into WT iPSCs, differentiation of the resulting KI iPSCs into the different brain cell types and subsequent generation of KI 3BTMs. With this approach we were able to directly compare the genetically modified KI cultures to isogenic WT cultures and follow phenotype formation over time. We could show that KI cultures secrete more Aβ in total and have a strongly increased Aβ42:40 ratio, producing more of the longer, more aggregation-prone species. We could further detect a time-dependent increase in insoluble AB42 specifically in the KI cultures as well as deposition of AB in the KI cultures seen in immunostainings. This deposition was increased by incorporation of AS and MG into the cultures, possibly hinting towards involvement of both cell types in Aβ accumulation. We also found an effect on Tau phosphorylation in the KI cultures, specifically when MG were present, with the Thr181 epitope showing higher phosphorylation levels compared to WT cultures. A later tauopathy marker, PHF1, showed a modest increase that was not (yet) statistically significant. Finally, using seeding approaches with recombinant Aβ42 we could elicit the formation of plaque-like structures in the 3BTMs 1 month after treatment. This aggregation further induced downstream tau pathology as seen by increased levels and accumulation of tau phosphorylated at the Thr181 epitope indicating axonal dystrophies, while no obvious synapse or dendrite degeneration or microglial barrier formation was visible. Taken together, we generated a reproducible and controllable, human iPSC-based cortical tissue model, showed the maturity and functionality of the incorporated cell types, and confirmed its potential for modelling early stages of AD pathogenesis. In a next step, additional experiments should be performed to further characterize the cultures.

4.1. Additional characterization of 3BTMs

To further characterize the 3BTMs and ensure reproducibility, additional experiments should determine if the ratio of NE:AS:MG is constant within and between experiments and over time, for example by staining for nuclear markers of the different cell types in sections of 3BTMs. A constant ratio would be highly beneficial as it reduces the number of variables which may influence cell function and maturation and disease phenotype formation. In addition, to confirm reproducibility over various iPSC lines, we already generated 3BTMs from 2 independent wildtype cell lines and several gene-edited cell lines derived from those, demonstrating that the protocol is robust. Confirming this with a broader range of wildtype cell lines or embryonic stem cells would further corroborate broad applicability of the protocol. However, we expect that 3BTM generation from different cell lines is likely less of a problem compared to organoids, as differences between cell lines mostly affect differentiation potential into the different brain cell types. In our experience these issues usually emerge in early stages of differentiation when they can still be alleviated by protocol optimizations.

Further experiments could also elucidate morphologies of single cells for all cell types to confirm a typical and mature morphology, and analyze potential changes over time. This could be done for example by sparse labelling using adeno-associated viruses or incorporation of fluorescently labelled cells at a small percentage. These approaches could show if neurons have typical morphology for example similar to pyramidal cells in the human cortex, or if we can observe different astrocyte subtypes such as protoplasmic or interlaminar astrocytes, as described after transplantation of human iPSC-derived astrocytes into mouse brains ²²⁰. Such approaches could also be used to investigate microglial ramification and overall morphology in the cultures, for example to analyze changes in presence or absence of astrocytes and over time, as preliminary observations indicate that MG may become more ramified at 3 months compared to 1 month of age, suggesting a more "homeostatic" phenotype.

To further characterize maturation of neurons in the 3BTMs, the expression of tau isoforms could be analyzed using western blot. As described earlier, iPSC-derived neurons have a fetal character and thus

initially express only 3R tau, while 4R Tau expression is only detectable after extended culture periods of around 4 months of age, increasing to around 10% at 6 months ¹⁸⁹. Even after 1 year, the adult 1:1 ratio of 3R to 4R tau is not achieved in 2D cultured neurons ²⁷². As both 3R and 4R tau isoforms are aggregating in AD, both likely need to be present to elicit AD-typical tauopathy phenotypes such as tangle formation. Therefore, a time course analysis of 3BTMs would indicate when and to what extent 4R tau is expressed. This would not only give insights into maturation and allow comparisons with published data from 2D cultured neurons and organoids, but could also be correlated with emerging tauopathy phenotypes such as misfolding or aggregation.

More in-depth characterization of the cultures could also be done by additional and larger scRNA sequencing experiments. The enriched data would further strengthen identification of different cell type identities, cell subtypes, and cell states as well as maturation stages and their reproducibility between experiments, and allow for a comparison with *in vivo* cells, organoid models and xenotransplanted cells from mouse brains. This could for example give insights into microglia behavior in the cultures and if they are overall in a "resting" or "activated" state in comparison to *in vivo* cells, and if or how signatures change when astrocytes are present. It would also clarify if cells in 3BTMs also display a specific stress-induced signature found in organoids due to lack of oxygen supply ^{273,274}, or if the small size and homogeneous cell distribution prevents this. Furthermore, time-course experiments could show maturation of the cells in 3BTMs over time and allow comparisons for example to human brain development.

In addition to further characterizations, several points could be addressed in the future to make 3BTMs more physiological and thus increase translatability especially in long-term cultures.

4.2. Further improvement of 3BTMs

As a first point, microglial survival/retainment in 3BTMs should be improved, as we observed a slow, continuous decrease in MG number in 3BTMs over time, at least in some experiments. This was evident especially in WT, and to a lower extent in KI cultures. The uneven decline in WT vs. KI cultures also impairs direct comparisons of groups at later timepoints, which is the main reason why many experiments described in this thesis were performed at 3 months, when microglia numbers are still comparable. Although AB pathology is further increasing up to 6 months, there were often more microglia found in KI than WT cultures at this timepoint, preventing faithful comparisons of the two genotypes. The cause for this decline in MG numbers is not fully known, but likely due to either migration of the microglia out of the cultures or continuous cell death. Observations of the culture media indicate that migration out of the culture is contributing, as single MG or small clumps of the cells were seen in the supernatants during extended cultures. Another observation we made is the improved survival/retainment of TREM2-KO microglia, which could further explain both mechanisms of MG loss in 3BTMs. On the one hand, TREM2-KO microglia show reduced motility, possibly resulting in lower migration out of the cultures. On the other hand, TREM2-KO MG are locked in a homeostatic state 128,129,269, which could suggest that WT and KI microglia are continuously overactivated leading to senescence and cell death over time. The slower decline in MG numbers in KI cultures would however speak against this hypothesis, as we expect MG to be more activated in KI cultures as seen in the preliminary scRNAseq experiment. Another observation speaking for the migration hypothesis is the accumulation of MG outside 3BTMs that were embedded into Matrigel. As shown in Figure 19B, MG are almost exclusively located in surrounding Matrigel and not in the culture at 6 months of age, indicating that the cells are alive but migrate out of the culture over time. One reason for the migration may be the continuous addition of the MG cytokines (IL34, TGF-β, MCSF) into the media at feeds. As the concentration of these pro-survival and "homeostatic" cytokines is higher in the supernatant compared to the cultures after feeding, MG may migrate towards the gradient and thus out of the cultures. One approach to circumvent this problem may thus be to stop addition or add lower amounts of the cytokines after a certain timepoint. As NE, AS, and microglia produce these cytokines as well ^{275–277}, microglia may be able to survive in the cultures with lower to no exogenous factors.

Another important milestone to improve 3BTMs and 3D in vitro models in general is incorporation of additional brain cell types, thus creating an even more physiological, brain-like environment. A first step may be addition of oligodendrocytes (OLGs). OLGs are the third major glial cell type in the brain and important both for modulation of action potential propagation by myelination of axons as well as trophic and metabolic support of neurons ²⁷⁸. OLGs may therefore improve survival especially of neurons in the cultures. Additionally, white matter abnormalities and oligodendroglial alterations are among the first signs of AD ²⁷⁹ and OLGs can produce Aβ, at least in rat ²⁸⁰, suggesting that they play a relevant role in AD pathogenesis. This is further corroborated by a recent preprint that proposes ageing-associated myelin dysfunction as a central driver of amyloid deposition ²⁸¹. The incorporation of OLGs into in vitro models may thus enable mechanistic studies of both early oligodendroglial reactions to amyloid pathology and modulation of pathology by OLGs. However, mature OLGs are not present in classical organoid differentiation protocols within trackable time frames ^{181,185}. Therefore, more recent studies used combinations of specific growth factors to generate organoids that contain oligodendrocytes ^{282–284}. However, myelination events in these models were sparse and formation of compact myelin and mature cell organization, e.g. by formation of nodes of Ranvier, were not convincingly shown. This may be due to too short culture periods, as it has been shown that myelination in the human cortex during development only starts after 24 gestational weeks ²⁸⁵ and is in general a lengthy process over many years ²⁸⁶. Indeed, the only study showing evidence of dense myelination and node formation uses spinal cord organoids ²⁸⁷, a region where myelination starts already at around 14 gestational weeks in human embryos ²⁸⁸. Our 3BTMs may be a more suitable system to induce myelination, as we can directly add oligodendrocyte precursor cells to the cultures, saving weeks to months compared to organoid protocols where they first need to develop. In addition, the microglia incorporated into the 3BTMs, and absent in the published models, may promote OLG differentiation and myelin formation ^{289,290}.

Another aim currently investigated in the field is vascularization of 3D cultures. A vascular network made of endothelial cells and associated pericytes or smooth muscle cells would likely improve oxygen and nutrient supply throughout the culture and create a more brain-like environment. The improved supply may also allow to produce larger cultures without formation of a necrotic core, which in turn may increase protein aggregation for example into A β plaques, as diffusion of A β out of the culture would be limited. Some studies showed first steps towards vascularization, for example by the generation of vascular organoids ^{291,292} or the development of microfluidic systems with vascular cells (e.g. ²⁹³), vascular cells and astrocytes (e.g. ²⁹⁴) or vascular cells, neurons, astrocytes, and microglia (e.g. ²⁹⁵). However, these systems are not fully based on human iPSC-derived cells, but partially on primary animal cells or immortalized cell lines, and can only be kept for days or few weeks. This limits their use in long-term disease modelling. Another approach to induce vascularization is the transplantation of organoids into mouse brain, which strongly reduces cell death compared to non-transplanted organoids ²⁵⁹. However, this very elaborate and low-throughput approach is difficult to apply for mechanistic studies and especially drug screenings. Our modular system may allow a different approach, by co-aggregating neural and vascular cells and subsequent co-development of neuritic and vascular networks.

Another general caveat of using hiPSCs for age-related, neurodegenerative disease research is the inherent rejuvenation of the cells during reprogramming, as shown by an increase in telomere length ²⁹⁶ and mitochondrial fitness ^{297,298}, loss of epigenetic marks associated with aging ^{299,300} as well as reduced nuclear morphology abnormalities and increased heterochromatin ³⁰¹. This rejuvenation

renders the resulting iPSC "fetal" and very comparable to embryonic stem cells, and greatly increases the proliferation potential of the cells. This fetal character of the cells is also kept during differentiation ³⁰¹, yielding for example fetal human brain cell types. However, as AD affects mostly elderly patients and thus aged cells, this rejuvenation may slow down or inhibit phenotype formation. To circumvent this problem, a study on Parkinson's disease used short-term overexpression of progerin, a mutated form of the nuclear envelope protein lamin A that causes a premature aging disease 301. iPSC-derived dopaminergic neurons exposed to progerin showed enhanced dendrite degeneration, progressive loss of marker expression and enlarged mitochondria or Lewy-body-precursor inclusions compared to untreated patient-derived neurons. However, this approach induced an artificial and pathological aging phenotype that differs from natural aging. An alternative way may be the acceleration of neuronal maturation with small molecules, as suggested in a recent preprint ³⁰². One way to avoid cell rejuvenation in the first place is direct conversion of fibroblasts or blood cells into induced neurons (iNs), without a stem cell intermediate, thereby keeping the aging signature of the donor cell. This transdifferentiation can be done by expression of specific transcription factors 303, a combination of transcription factors and small molecules ^{304–306}, or only small molecules ^{307,308}. Indeed, it has been shown that these iNs retain the aging-associated transcriptomic signature of the donor cell and agingspecific nucleocytoplasmic compartmentalization defects 306. Directly converted neurons from AD patients showed transcriptional and cellular defects hinting towards a partial de-differentiation and hypo-mature state due to epigenetic changes. These pathogenic changes were only very mildly recapitulated in iPSC-derived neurons from the same patients, suggesting age-specific defects in the transdifferentiated cells that are lost during reprogramming 309. A disadvantage of direct conversion may be the different cell identities of donor and converted cell. As the aging signature is retained, the resulting neurons do show skin- or blood, but not necessarily brain-specific, age-related changes which may interfere with AD-induced alterations. In addition, by skipping the stem cell stage and directly generating post-mitotic cells such as neurons, the proliferation potential is lower, thereby limiting the cell number that can be obtained for mechanistic studies and drug screens. This may be improved by direct conversion of fibroblasts into NPCs instead of differentiated neurons. This approach could also yield additional cell types such as astrocytes and oligodendrocytes ³¹⁰, while still retaining the aging signature of the donor cell ³¹¹. Current studies using transdifferentiated cells for AD research however only used neurons, limiting mechanistic studies to this cell type. Finally, by skipping the stem cell stage, genetic manipulations are much more laborious and would need to be repeated for each batch of cells, restricting studies to patient-derived cells which may not be readily available. Therefore, a combination of the different approaches may yield best results in the future. This could be achieved by inhibiting rejuvenation upon reprogramming of somatic cell types to iPSCs, which may however again restrict proliferation potential, or by developing novel approaches to age iPSC-derived brain cell types in vitro.

4.3. Discussion of AD-related phenotypes

Comparing KI and WT cultures, future experiments should elucidate the mechanisms behind the increased accumulation of $A\beta$ in the presence of AS or MG compared to cultures containing only NE. I did not detect any differences in levels of secreted $A\beta$ in the different cultures, suggesting that the additional cell types do not increase $A\beta$ production itself but enhance accumulation of $A\beta$ produced by the neurons. The effect of AS may be due to ApoE production and secretion by the cells, as it has been shown that ApoE can promote $A\beta$ accumulation 312 . This could be tested by incorporation of ApoE-KO AS instead of ApoE-WT AS into the cultures, which can easily be investigated in our modular model. The potential additional effect of MG could be due to the cells taking up soluble $A\beta$ which may then not be degraded 313 , but instead accumulated or aggregated inside the acidic milieu of endosomes or lysosomes 314 and secreted again by the cells or by cell death, similar to mechanisms observed in mouse

brains 33,37 . This could be tested by incorporation of TREM2-KO MG, which phagocytose less A β 50,270 . Alternatively, MG are known to increase ApoE expression in a "reactive" state, therefore if the cells get activated by amyloid pathology, the additional microglial ApoE may further increase A β accumulation. However, we did not detect an increased ApoE expression in MG in KI cultures in our preliminary scRNA seq dataset.

In a similar way, it would be interesting to further investigate the mechanisms behind the increased pTau levels we observed in NE+AS+MG but not NE+AS cultures. The difference may be due to the increased A β accumulation in cultures containing microglia at 3 months of age, but this effect did not reach statistical significance with the current data and would need to be confirmed in a larger dataset. Alternatively, the nature of the accumulations in MG-containing cultures may be different, making them more toxic to surrounding neurons. One study for example proposed that microglia can promote conversion of A β into more neurotoxic forms by shedding of microvesicles ³¹⁵. To further investigate the underlying mechanisms, co-stainings for pTau, A β and microglia could show if pTau is specifically increased around A β accumulations and if there are any interactions with surrounding microglia. Alternatively, incorporation of TREM2-KO microglia could clarify if microglial "activation" is necessary to elicit the effect.

Moreover, additional scRNA sequencing experiments should confirm the results found in the preliminary dataset, such as the additional microglia cluster found in the KI compared to WT cultures. If the results hold true, a closer analysis of the different clusters may give insights into the earliest changes found in human microglial states upon amyloid pathology, compared to most other studies that only analyze microglial reactions to plaque pathology. Several of the genes defining the KIenriched cluster we found have been associated with synaptic pruning (C1QA/B/C) 316, and aberrantly increased synapse pruning, leading to synapse loss, has been proposed as an early mechanism in AD pathogenesis before plaque formation ³¹⁷. Future experiments may therefore compare overall synapse numbers in WT compared to KI cultures over time, and use high resolution imaging or flow cytometry to quantify uptake of synaptic material by microglia in the different cultures to show functional consequences of the increased expression levels. CD14, the top hit in the list defining KI-specific cluster 4, has also been associated with AD before and was described as a receptor for A β phagocytosis 318 whose deletion attenuates AD pathology by altering microglial inflammatory responses 319. Other proteins in the list hint towards possible alterations in lysosomal function and lipid metabolism. For example, STAB1 has been identified as an LDL receptor 320,321, LIPA encodes lysosomal acid lipase, a lipid degrading enzyme in the lysosome ³²², FUCA1 and CTSS are lysosomal enzymes ^{323–325} and PSAP is present in the lysosome as well, giving rise to different saposins that facilitate glycosphingolipid catabolism ³²⁶. Lipid accumulations and lipid dyshomeostasis have emerged as key pathogenic factors in AD ³²⁷, and impaired lysosomal function may be a general player of protein accumulation disorders such as AD ³²⁸. Therefore, if confirmed on a protein level, investigation of lipid metabolism and lipid composition as well as lysosomal function in the 3BTMs could give further insights into underlying mechanisms and downstream effects at the early disease state modeled in the cultures. Another scRNA sequencing experiment with more cells would likely also allow more powerful comparisons of neuronal and astrocytic clusters between the genotypes, potentially elucidating disease-associated clusters of the cells or general differences in gene expression or cell states. Finally, when microglia numbers and survival have been optimized as mentioned above, also later timepoints could be analyzed. This would allow time course analyses of disease-associated changes in the single cells and their correlation with progressing amyloid or tau pathology.

In addition, proteomic analysis of WT and KI 3BTMs could be performed to confirm transcriptomic results on a protein level and potentially identify additional important factors, as studies showed that RNA and protein levels and AD-associated changes therein can differ in brain tissue ^{329–331}. Proteomic

analysis could thus provide more insights into functional changes in KI cultures compared to transcriptomic studies. However, this would require prior confirmation of constant cell type ratios between experiments and genotypes to ensure that detected changes are due to AD mutations and not due to altered cell type composition. Otherwise, alterations in cell numbers may introduce artificial effects, as only overall protein levels and not proteins inside single cells are quantified in traditional mass spectrometry analysis.

Finally, it should be confirmed that observed phenotypes are due to increased A β secretion induced by the inserted mutations, and not by unnoticed off-target effects. To this end, A β production in the KI cultures could be suppressed by treatment with beta- or gamma-secretase inhibitors, or shifted back to a normal A β 42:40 ratio with gamma-secretase modulators, which should rescue or reduce the observed pathological phenotypes. This would also illustrate suitability of the model for pharmacological screenings.

4.4. Induction of Aβ plaque pathology in 3BTMs

One of the aims of this thesis was the generation of a human in vitro model that recapitulates mature Aβ plaque pathology, which may be sufficient to induce further pathologies such as tau aggregation and neurodegeneration in human cells ²¹⁹. Using our triple APP KI line, we could elicit the formation of focal accumulations which may represent early stages of plaque formation. This amyloid pathology was progressing over time but even after extended culture periods of almost one year we did not detect mature diffuse or dense core plaques. In contrast, the corresponding NL-G-F knock-in mouse model forms diffuse plaques after 2-3 months, and dense-core plaques after around 12 months ¹⁰⁰. The reasons for this discrepancy could include the lack of an essential cell type, such as oligodendrocytes as suggested in a recent preprint ²⁸¹, or another factor in our *in vitro* model compared to the brain, or lower AB levels in our cultures that therefore do not reach a certain threshold needed for widespread and dense aggregation. The latter point is supported by our preliminary measurements of A β concentration and total A β amounts in the cultures compared to the conditioned supernatant. Our data suggests that there is a diffusion gradient from the culture into the media, as the concentration is on average about 10-fold higher within the cultures. As the cells continuously produce Aβ and the culture volume is much smaller than the media volume, this gradient is never balanced, leading to approximately 75x higher total Aβ levels in the supernatant, meaning that around 98-99 % of the produced Aβ is diffusing out of the culture. Interestingly, our preliminary data suggests that the ratio is dependent on the Aβ species investigated, with Aβ38 having the lowest and Aβ42 the highest culture:supernatant ratio, suggesting that more A\(\beta 42 \) is retained in the culture, possibly as it is accumulating more easily before diffusing out. This is in line with the higher amount of Aβ42 in the insoluble protein fraction from the cultures, which also increases over time. Nevertheless, the concentration does not seem sufficient to initiate widespread aggregation.

Based on these results, the first approach we tested to facilitate plaque formation was to limit diffusion and promote retention of $A\beta$ within the culture by embedding 3BTMs into Matrigel. However, this approach did not significantly alter $A\beta$ accumulation nor induce plaque formation. This may be improved by increasing the amount of Matrigel used for embedding and thus further reducing diffusion. This would however affect not only $A\beta$, but also nutrients and oxygen, thus possibly leading to necrotic core formation. In addition, Matrigel is a mouse-tumor-derived matrix with almost no resemblance to human brain ECM and contains growth factors with batch-to-batch variation. These growth factors likely also led to the outgrowth of neurons and astrocytes and migration of microglia into the Matrigel, resulting in the disintegration of the original culture. Altogether, there was no significant benefit from this approach.

Another caveat impairing aggregation may be the high levels of Aβ38 that are produced by our KI cells. Recent studies suggest that shorter Aβ species such as Aβ37/38/40 inhibit aggregation of Aβ42 *in vitro* 332,333 , and that higher A β_{38} levels are associated with slower cognitive decline in patients 334 . Therefore, the high levels of Aβ38 produced by the cells, even though it is mostly diffusing out of the culture, may inhibit or slow down aggregation of Aβ42 and thus plaque formation. To circumvent this problem, a different set of mutations could be used. By comparing iPSC lines with only APP^{Arc} or APP^{Ibe} or both mutations, we found that each mutation increased Aβ38 levels independently, with APP^{lbe} having a stronger effect, and both acting synergistically when combined. Therefore, both mutations should be replaced if possible. The Iberian mutation could for example be replaced by a PSEN1 mutation such as PSEN1 L166P, that causes a similarly strong increase in A β 42:40 ratio while reducing levels of A β 38 ²³⁵. However, as PSEN1 is part of γ -secretase, mutations in the protein do not only cause changes in A β levels, but also other physiological substrates. It has been shown for example that the L166P mutation impairs Notch cleavage and signaling 335. As Notch is an important factor also in neuronal differentiation, with Notch inhibition promoting NPC formation and neuron differentiation 336,337, the effect of PSEN1 mutations on iPSC differentiation needs to be closely analyzed to avoid any unwanted off-target effects on neuronal fate and maturity that could produce misleading results. The APPArc mutation has unique effects on Aß fibrillization and can therefore not easily be replaced, but only omitted. This may delay aggregation as shown by the comparison of NL-F (without APPArc) and NL-G-F (with APP^{Arc}) mouse models, with the former starting plaque formation only after 12 months, compared to 2-3 months in the latter. However, as mentioned above, the plaques first forming in NL-G-F mice are diffuse, similar to what has been described in patients carrying the APP^{Arc} mutation ^{338,339}. Only after around 12 months dense-core plaques form ³³¹, similar to NL-F mice ¹⁰⁰, and this also coincides with increased microglial recruitment ³³¹. Nevertheless, the mouse models show that the used mutations can induce mature plaque formation within few months, suggesting that they are not the main hurdle to elicit widespread aggregation. We thus hypothesized that the Aβ concentration in the 3BTMs is not high enough to start the aggregation process due to the factors mentioned above.

I therefore tested the effect of seeding Aβ into the culture, to provide pre-formed oligomers and fibrils and thus facilitate or skip the initial and likely rate-limiting step of aggregation. Seeding with mouse brain extract from APP/PS1 mice did not induce mature plaque development up to 6 months after seeding, while the use of recombinant human Aβ42 induced the formation of structures resembling amyloid plaques 1 months after addition. In immunofluorescence stainings, the structures were positive for both Aβ and dyes binding fibrillar amyloids such as X34 and pFTAA, and induced increased pTau levels and accumulation, suggesting biological activity and effects on neighboring neurons with possible axonal dystrophies. However, this was observed not only in KI, but also WT cultures, suggesting that the plaque-like structures are built of the exogenously added material at this point, not endogenous Aβ. Therefore, further optimizations are necessary to elucidate if it is possible to induce plaque formation specifically in KI cultures by only adding the initial aggregation seed, which is then expanded by endogenous Aβ by templated aggregation. In addition, I did not observe any obvious synaptic or dendritic degeneration around the aggregated material, and only in some cases microglia associated with it, but no clear microglial barrier or interaction. This could be due to the early timepoint investigated or the addition of exogenous, and likely excess, TGFB into the culture media at feeds, as TGFβ is known to promote a "homeostatic" microglial state 340,341 and can inhibit microglia-induced synapse loss ³⁴². Alternatively, it could indicate that although aggregation into plaque-like structures occurs, these structures are rather inert, as it has been shown in human brain that microglia do not cluster around inert plaques 343. However, these inert human plaques were characterized by the lack of an Aβ-positive halo, while we could detect such a halo around our plaque-like structures (Figure 191). Another reason for the development of partial, but not full-blown pathology around the plaquelike structures could lie in the nature of the recombinant Aβ. It has been shown for example, that synthetic Aβ has lower seeding potential than AD brain-derived extracts from mouse or human ^{344,345} and that when seeding is successful, biological activity of the synthetic seeds, as measured by astrogliosis, is lower ³⁴⁵. Another study showed that seeding potential is increased with synthetic Aβ43 compared to Aβ42, although plaque-inducing activity was still much lower compared to brain-derived seeds ³⁴⁶. This lower activity may be due to the lack of certain modifications of the synthetic material. It has been shown that brain-derived Aβ can for example be phosphorylated, promoting oligomerization and subsequent fibril formation and increasing toxicity of the peptide ³⁴⁷. Other studies showed that Aβ in the brain can be N-terminally truncated and subsequently pyroglutamylated, and that the resulting pyro-Glu-Aβ is a major component of plaques ³⁴⁸. Pyro-Glu-Aβ has also been proposed as a seeding peptide species ³⁴⁹ by co-aggregating with Aβ42 into distinct oligomers ³⁵⁰. The lack of these modification in the synthetic AB may thus impair brain-like aggregation and toxicity. Besides differences in posttranslational modifications, a recent study found that recombinant Aβ42 adopts a slightly different structure compared to Aβ42 extracted from AD brains ³⁵¹. This altered conformation may thus not be as competent in seeding, as endogenous Aβ, which likely has a brainlike structure, may not be able to readily adopt this conformation, for example due to the posttranslational modifications mentioned above. The APP^{Arc} mutation may further complicate the process, as it is located in the middle of the $A\beta$ peptide and could therefore alter its structure. Finally, the low seeding efficiency in 3BTMs may be due to the lack of a brain-specific factor. It has been shown for example that seeding with brain lysate that is effective in mouse brains 344 does not induce plaque formation in acute mouse brain slices. Instead, only after initial seeding with brain lysate and subsequent, constant application of synthetic Aβ over weeks, formation of plaques could be observed, which elicited neuritic pathology and microgliosis ³⁵². However, this again was observed not only in transgenic amyloidosis mouse models, but also WT mice, indicating aggregation of mostly exogenous material similar to our model. In general, the authors did also not observe endogenous plaque formation in the brain slices in contrast to the in vivo model. This could again be explained by increased diffusion of Aβ into the media in the slices compared to the brain, strengthening the hypothesis that this may be the limiting factor to induce plaque formation in vitro. Future experiments on our 3BTMs could still test similar seeding approaches with an initial application of human AD brain extract, and subsequent continuous treatment with low levels of synthetic Aβ42 or Aβ43. This continuous treatment may compensate for the loss of endogenous Aβ into the media or counteract the diffusion gradient of the endogenous peptides out of the culture. Finally, seeding approaches could be combined with the incorporation of TREM2-KO microglia as this has been shown to increase seeding in a mouse model ²⁴⁰.

Another approach to induce plaque formation in 3BTMs could be increased production of A β by overexpression of APP, to raise peptide levels to the threshold needed for aggregation before it can diffuse out of the culture. Overexpression of APP and PSEN1 containing AD-causing mutations has been shown to induce potential formation of plaque-like structures in 3D *in vitro* models made of neuronal cells embedded in Matrigel ²⁰⁷, confirming the feasibility of the method. However, this approach may also lead to artificial phenotypes due to the overexpression of APP itself and all its cleavage products, not only A β , and subsequent aberrant interactions with other cellular proteins.

Finally, as an additional pro-aggregation factor, the ApoE genotype of the cells may be altered. The cells used in this thesis have an ApoE3/E3 genotype. Using CRISPR/Cas9, this could be altered to the AD risk allele ApoE4/E4, as ApoE4 has been shown to enhance amyloid deposition at early stages and increases half-life of A β ³⁵³, potentially by altering A β clearance ³⁵⁴. In addition, due to the modularity of our system we could investigate cell-type specific effects of ApoE4 expression, as both astrocytic and microglial ApoE4 may have distinct, disease-modifying roles ²⁶⁷.

In summary, we established an approach to elicit formation of plaque-like structures by seeding with human recombinant A β 42, but further optimizations and potentially longer time frames are needed to increase biological activity of protein aggregates and induce co-aggregation of endogenous material.

4.5. Summary and Outlook

Altogether, we established a controllable and reproducible, human stem-cell based 3D in vitro model that can be used to study cell interactions and functionality as well as neurological diseases such as AD. The model is a promising complementary system to current AD models such as transgenic mice and post-mortem brain tissue, as it combines the advantages of human systems with the possibility to study early and intermediate disease processes, and increasingly easy genomic access to study effects of disease-causing variants and risk factors. In addition, the controllability and reproducibility of the model, the possibility to include additional cell types, and the absence of a necrotic core improve its suitability to investigate cell-type interactions in physiological and pathological contexts and its use for mechanistic studies and drug screening approaches, compared to currently used 3D in vitro models. After introducing AD-causing mutations, we observed the formation of AD phenotypes such as progressive, extracellular Aß accumulation and aggregation into insoluble material, increased pTau levels and possibly microglial activation. The model thus enables the systematic study of processes underlying these changes, which could identify novel therapeutic targets at this early disease stage. By applying seeding approaches, we could further elicit formation of plaque-like structures and concomitant tau pathology. On this basis, future experiments can elucidate the conditions and factors necessary to elicit widespread aggregation into mature Aβ plaques and possible subsequent effects such as tau misfolding and aggregation, synapse and neurite damage, and finally neurodegeneration. The resulting fully human in vitro model would be the first of its kind to recapitulate central AD hallmarks and would thus strongly advance the field of AD research. It would enable the analysis of potentially human-specific mechanisms leading to protein aggregation and neurodegeneration, interactions between different pathologies such as the Aβ-tau axis, and the role of different glial cells in disease over time.

5. References

- 1. Gustavsson, A. *et al.* Global estimates on the number of persons across the Alzheimer's disease continuum. *Alzheimer's Dement.* (2022). doi:10.1002/ALZ.12694
- 2. Alzheimer, A. Ueber eine eigenartige Erkrankung der Hirnrinde. *Allg Z Psychiat Psych-Gerichtl Med* 146–148. (1907).
- 3. Salloway, S. *et al.* Amyloid-Related Imaging Abnormalities in 2 Phase 3 Studies Evaluating Aducanumab in Patients With Early Alzheimer Disease. *JAMA Neurol.* **79**, 13–21 (2022).
- 4. Walker, L. C. & Jucker, M. The Exceptional Vulnerability of Humans to Alzheimer's Disease. *Trends Mol. Med.* **23**, 534–545 (2017).
- 5. Bateman, R. J. *et al.* Clinical and biomarker changes in dominantly inherited Alzheimer's disease. *N. Engl. J. Med.* **367**, 795–804 (2012).
- 6. Fagan, A. M. *et al.* Longitudinal change in CSF biomarkers in autosomal-dominant Alzheimer's disease. *Sci. Transl. Med.* **6**, (2014).
- 7. Berr, C., Wancata, J. & Ritchie, K. Prevalence of dementia in the elderly in Europe. *Eur. Neuropsychopharmacol.* **15**, 463–471 (2005).
- 8. Van Der Flier, W. M. & Scheltens, P. Epidemiology and risk factors of dementia. *J. Neurol. Neurosurg. Psychiatry* **76**, v2–v7 (2005).
- 9. Bateman, R. J. *et al.* Autosomal-dominant Alzheimer's disease: a review and proposal for the prevention of Alzheimer's disease. *Alzheimers. Res. Ther.* **3**, 1 (2011).
- 10. Morris, J. C. *et al.* Autosomal dominant and sporadic late onset Alzheimer disease share a common in vivo pathophysiology. *Brain* **139**, 16–17 (2022).
- 11. Kuhn, P. H. *et al.* ADAM10 is the physiologically relevant, constitutive α -secretase of the amyloid precursor protein in primary neurons. *EMBO J.* **29**, 3020–3032 (2010).
- 12. Vassar, R. *et al.* β-Secretase cleavage of Alzheimer's amyloid precursor protein by the transmembrane aspartic protease BACE. *Science* (80-.). **286**, 735–741 (1999).
- 13. Willem, M. et al. η -Secretase processing of APP inhibits neuronal activity in the hippocampus. *Nat. 2015* 5267573 **526**, 443–447 (2015).
- 14. Sasaguri, H. *et al.* APP mouse models for Alzheimer's disease preclinical studies. *EMBO J.* e201797397 (2017). doi:10.15252/embj.201797397
- 15. Wolfe, M. S. *et al.* Two transmembrane aspartates in presentiin-1 required for presentiin endoproteolysis and gamma-secretase activity. *Nature* **398**, 513–517 (1999).
- 16. Li, Y. M. *et al.* Photoactivated gamma-secretase inhibitors directed to the active site covalently label presenilin 1. *Nature* **405**, 689–694 (2000).
- 17. Hardy, J. A. & Higgins, G. A. Alzheimer's disease: The amyloid cascade hypothesis. *Science (80-.).* **256**, 184–185 (1992).
- 18. Selkoe, D. J. & Hardy, J. The amyloid hypothesis of Alzheimer's disease at 25 years. *EMBO Mol. Med.* **8**, 595–608 (2016).
- 19. Seubert, P. *et al.* Isolation and quantification of soluble Alzheimer's beta-peptide from biological fluids. *Nature* **359**, 325–327 (1992).
- 20. Shoji, M. *et al.* Production of the Alzheimer amyloid beta protein by normal proteolytic processing. *Science* **258**, 126–129 (1992).
- 21. Furukawa, K., Barger, S. W., Blalock, E. M. & Mattson, M. P. Activation of K+ channels and suppression of neuronal activity by secreted beta-amyloid-precursor protein. *Nature* **379**, 74–78 (1996).
- 22. Taylor, C. J. *et al.* Endogenous secreted amyloid precursor protein-alpha regulates hippocampal NMDA receptor function, long-term potentiation and spatial memory. *Neurobiol. Dis.* **31**, 250–260 (2008).

- 23. Puzzo, D. *et al.* Picomolar amyloid-beta positively modulates synaptic plasticity and memory in hippocampus. *J. Neurosci.* **28**, 14537–14545 (2008).
- 24. Puzzo, D. *et al.* Endogenous Amyloid-β is Necessary for Hippocampal Synaptic Plasticity and Memory. *Ann. Neurol.* **69**, 819 (2011).
- 25. Soscia, S. J. *et al.* The Alzheimer's disease-associated amyloid beta-protein is an antimicrobial peptide. *PLoS One* **5**, (2010).
- 26. Kumar, D. K. V. *et al.* Amyloid-β peptide protects against microbial infection in mouse and worm models of Alzheimer's disease. *Sci. Transl. Med.* **8**, (2016).
- 27. Querol-Vilaseca, M. *et al.* Nanoscale structure of amyloid-β plaques in Alzheimer's disease. *Sci. Reports* 2019 91 9, 1–10 (2019).
- 28. Sanchez-Varo, R. *et al.* Plaque-Associated Oligomeric Amyloid-Beta Drives Early Synaptotoxicity in APP/PS1 Mice Hippocampus: Ultrastructural Pathology Analysis. *Front. Neurosci.* **15**, 1424 (2021).
- 29. Fleisher, A. S. *et al.* Florbetapir PET analysis of amyloid-β deposition in the presenilin 1 E280A autosomal dominant Alzheimer's disease kindred: a cross-sectional study. *Lancet. Neurol.* **11**, 1057–1065 (2012).
- 30. Nelson, P. T. *et al.* Correlation of Alzheimer Disease Neuropathologic Changes With Cognitive Status: A Review of the Literature. *J. Neuropathol. Exp. Neurol.* **71**, 362 (2012).
- 31. Kayed, R. & Lasagna-Reeves, C. A. Molecular mechanisms of amyloid oligomers toxicity. *J. Alzheimers. Dis.* **33 Suppl 1**, (2013).
- 32. Huang, Y. *et al.* Microglia use TAM receptors to detect and engulf amyloid β plaques. *Nat. Immunol.* (2021). doi:10.1038/s41590-021-00913-5
- 33. Baik, S. H., Kang, S., Son, S. M. & Mook-Jung, I. Microglia contributes to plaque growth by cell death due to uptake of amyloid β in the brain of Alzheimer's disease mouse model. *Glia* **64**, 2274–2290 (2016).
- 34. Itagaki, S., Mcgeer, P. L., Akiyama, H., Zhu, S. & Selkoe, D. *Relationship of microglia and astrocytes to amyloid deposits of Alzheimer disease. Journal of Neuroimmunology* **24**, (1989).
- 35. Condello, C., Yuan, P., Schain, A. & Grutzendler, J. Microglia constitute a barrier that prevents neurotoxic protofibrillar Aβ42 hotspots around plaques. *Nat. Commun. 2015 61* **6**, 1–14 (2015).
- 36. Yuan, P. *et al.* TREM2 Haplodeficiency in Mice and Humans Impairs the Microglia Barrier Function Leading to Decreased Amyloid Compaction and Severe Axonal Dystrophy. *Neuron* **90**, 724–739 (2016).
- 37. d'Errico, P. *et al.* Microglia contribute to the propagation of Aβ into unaffected brain tissue. *Nat. Neurosci.* (2021). doi:10.1038/s41593-021-00951-0
- 38. Streit, W. J., Walter, S. A. & Pennell, N. A. Reactive microgliosis. *Prog. Neurobiol.* 57, 563–581 (1999).
- 39. Glass, C. K., Saijo, K., Winner, B., Marchetto, M. C. & Gage, F. H. Mechanisms Underlying Inflammation in Neurodegeneration. *Cell* **140**, 918–934 (2010).
- 40. Liddelow, S. A. *et al.* Neurotoxic reactive astrocytes are induced by activated microglia. *Nature* **541**, 481–487 (2017).
- 41. Guttenplan, K. A. *et al.* Neurotoxic reactive astrocytes induce cell death via saturated lipids. *Nature* (2021). doi:10.1038/s41586-021-03960-y
- 42. Krabbe, G. *et al.* Functional Impairment of Microglia Coincides with Beta-Amyloid Deposition in Mice with Alzheimer-Like Pathology. *PLoS One* **8**, e60921 (2013).
- 43. Hellwig, S. *et al.* Forebrain microglia from wild-type but not adult 5xFAD mice prevent amyloid-β plaque formation in organotypic hippocampal slice cultures. *Sci. Reports 2015 51 5*, 1–9 (2015).
- 44. Hansen, D. V., Hanson, J. E. & Sheng, M. Microglia in Alzheimer's disease. J. Cell Biol. 217, 459 (2018).
- 45. Jansen, I. E. *et al.* Genome-wide meta-analysis identifies new loci and functional pathways influencing Alzheimer's disease risk. *Nat. Genet. 2019 513* **51**, 404–413 (2019).
- 46. Jonsson, T. *et al.* Variant of TREM2 Associated with the Risk of Alzheimer's Disease . *N. Engl. J. Med.* **368**, 107–116 (2013).

- 47. Guerreiro, R. et al. TREM2 Variants in Alzheimer's Disease . N. Engl. J. Med. 368, 117-127 (2013).
- 48. Hall-Roberts, H. *et al.* TREM2 Alzheimer's variant R47H causes similar transcriptional dysregulation to knockout, yet only subtle functional phenotypes in human iPSC-derived macrophages. *Alzheimer's Res. Ther.* **12**, (2020).
- 49. Piers, T. M. *et al.* A locked immunometabolic switch underlies TREM2 R47H loss of function in human iPSC-derived microglia. *FASEB J.* **34**, 2436 (2020).
- 50. Kleinberger, G. *et al.* TREM2 mutations implicated in neurodegeneration impair cell surface transport and phagocytosis. *Sci. Transl. Med.* **6**, (2014).
- 51. Goedert, M., Wischik, C. M., Crowther, R. A., Walker, J. E. & Klug, A. Cloning and sequencing of the cDNA encoding a core protein of the paired helical filament of Alzheimer disease: identification as the microtubule-associated protein tau. *Proc. Natl. Acad. Sci. U. S. A.* **85**, 4051 (1988).
- 52. Ksiezak-Reding, H. & Yen, S. H. Structural stability of paired helical filaments requires microtubule-binding domains of tau: a model for self-association. *Neuron* **6**, 717–728 (1991).
- 53. Goedert, M., Spillantini, M. G., Jakes, R., Rutherford, D. & Crowther, R. A. Multiple isoforms of human microtubule-associated protein tau: sequences and localization in neurofibrillary tangles of Alzheimer's disease. *Neuron* **3**, 519–526 (1989).
- 54. Hefti, M. M. *et al.* High-resolution temporal and regional mapping of MAPT expression and splicing in human brain development. *PLoS One* **13**, e0195771 (2018).
- 55. Cleveland, D. W., Hwo, S. Y. & Kirschner, M. W. Physical and chemical properties of purified tau factor and the role of tau in microtubule assembly. *J. Mol. Biol.* **116**, 227–247 (1977).
- 56. Schweers, O., Schonbrunn-Hanebeck, E., Man, A. & Mandelkows, E. *Structural studies of tau protein and Alzheimer paired helical filaments show no evidence for beta-structure.* **269**, (1994).
- 57. Witman, G. B., Cleveland, D. W., Weingarten, M. D. & Kirschner, M. W. Tubulin requires tau for growth onto microtubule initiating sites. *Proc. Natl. Acad. Sci. U. S. A.* **73**, 4070–4074 (1976).
- 58. Knops, J. *et al.* Overexpression of tau in a nonneuronal cell induces long cellular processes. *J. Cell Biol.* **114**, 725–733 (1991).
- 59. Caceres, A. & Kosik, K. S. Inhibition of neurite polarity by tau antisense oligonucleotides in primary cerebellar neurons. *Nature* **343**, 461–463 (1990).
- 60. Violet, M. *et al.* A major role for Tau in neuronal DNA and RNA protection in vivo under physiological and hyperthermic conditions. *Front. Cell. Neurosci.* **8**, (2014).
- 61. Sultan, A. *et al.* Nuclear tau, a key player in neuronal DNA protection. *J. Biol. Chem.* **286**, 4566–4575 (2011).
- 62. Marciniak, E. et al. Tau deletion promotes brain insulin resistance. J. Exp. Med. 214, 2257–2269 (2017).
- 63. Grundke-Iqbal, I. *et al.* Abnormal phosphorylation of the microtubule-associated protein tau (tau) in Alzheimer cytoskeletal pathology. *Proc. Natl. Acad. Sci. U. S. A.* **83**, 4913–7 (1986).
- 64. Ashton, N. J. *et al.* Plasma p-tau231: a new biomarker for incipient Alzheimer's disease pathology. *Acta Neuropathol.* **141**, 709–724 (2021).
- 65. Thijssen, E. H. *et al.* Diagnostic value of plasma phosphorylated tau181 in Alzheimer's disease and frontotemporal lobar degeneration. *Nat. Med.* **26**, 387–397 (2020).
- 66. Palmqvist, S. *et al.* Discriminative Accuracy of Plasma Phospho-tau217 for Alzheimer Disease vs Other Neurodegenerative Disorders. *JAMA* **324**, 772–781 (2020).
- 67. Kohnken, R. *et al.* Detection of tau phosphorylated at threonine 231 in cerebrospinal fluid of Alzheimer's disease patients. *Neurosci. Lett.* **287**, 187–190 (2000).
- 68. Arai, H. *et al.* CSF phosphorylated tau protein and mild cognitive impairment: a prospective study. *Exp. Neurol.* **166**, 201–203 (2000).
- 69. Suárez-Calvet, M. *et al.* Novel tau biomarkers phosphorylated at T181, T217 or T231 rise in the initial stages of the preclinical Alzheimer's continuum when only subtle changes in Aβ pathology are detected.

- EMBO Mol. Med. 12, (2020).
- 70. Konzack, S., Thies, E., Marx, A., Mandelkow, E. M. & Mandelkow, E. Swimming against the Tide: Mobility of the Microtubule-Associated Protein Tau in Neurons. *J. Neurosci.* **27**, 9916–9927 (2007).
- 71. Zempel, H., Thies, E., Mandelkow, E. & Mandelkow, E. M. Aβ Oligomers Cause Localized Ca2+ Elevation, Missorting of Endogenous Tau into Dendrites, Tau Phosphorylation, and Destruction of Microtubules and Spines. *J. Neurosci.* **30**, 11938 (2010).
- 72. Jicha, G., Bowser, R., Kazam, I. & Davies, P. Alz-50 and MC-1, a new monoclonal antibody raised to paired helical filaments, recognize conformational epitopes on recombinant tau Jicha 1997 Journal of Neuroscience Research Wiley Online Library. *J. Neurosci. Res.* 128–132 (1997).
- 73. Carmel, G., Mager, E. M., Binder, L. I. & Kuret, J. The structural basis of monoclonal antibody Alz50's selectivity for Alzheimer's disease pathology. *J. Biol. Chem.* **271**, 32789–32795 (1996).
- 74. Scheres, S. H., Zhang, W., Falcon, B. & Goedert, M. Cryo-EM structures of tau filaments. *Curr. Opin. Struct. Biol.* **64**, 17–25 (2020).
- 75. Tian, H. *et al.* Trimeric tau is toxic to human neuronal cells at low nanomolar concentrations. *Int. J. Cell Biol.* **2013**, (2013).
- 76. Khlistunova, I. *et al.* Inducible expression of Tau repeat domain in cell models of tauopathy: aggregation is toxic to cells but can be reversed by inhibitor drugs. *J. Biol. Chem.* **281**, 1205–1214 (2006).
- 77. Xia, C. *et al.* Association of In Vivo [18F]AV-1451 Tau PET Imaging Results With Cortical Atrophy and Symptoms in Typical and Atypical Alzheimer Disease. *JAMA Neurol.* **74**, 427–436 (2017).
- 78. Arriagada, P. V., Growdon, J. H., Hedley-Whyte, E. T. & Hyman, B. T. Neurofibrillary tangles but not senile plaques parallel duration and severity of Alzheimer's disease. *Neurology* **42**, 631–639 (1992).
- 79. Peters, F. *et al.* Tau deletion reduces plaque-associated BACE1 accumulation and decelerates plaque formation in a mouse model of Alzheimer's disease. *EMBO J.* **38**, (2019).
- 80. Leroy, K. *et al.* Lack of tau proteins rescues neuronal cell death and decreases amyloidogenic processing of APP in APP/PS1 mice. *Am. J. Pathol.* **181**, 1928–1940 (2012).
- 81. Götz, J., Chen, F., Van Dorpe, J. & Nitsch, R. M. Formation of Neurofibrillary Tangles in P301L Tau Transgenic Mice Induced by Aβ42 Fibrils. *Science* (80-.). **293**, 1491–1495 (2001).
- 82. Lewis, J. *et al.* Enhanced neurofibrillary degeneration in transgenic mice expressing mutant tau and APP. *Science* (80-.). **293**, 1487–1491 (2001).
- 83. Bennett, R. E. *et al.* Enhanced Tau Aggregation in the Presence of Amyloid β. *Am. J. Pathol.* **187**, 1601–1612 (2017).
- 84. Pooler, A. M. *et al.* Amyloid accelerates tau propagation and toxicity in a model of early Alzheimer's disease. *Acta Neuropathol. Commun.* **3**, 14 (2015).
- 85. Jin, M. *et al.* Soluble amyloid beta-protein dimers isolated from Alzheimer cortex directly induce Tau hyperphosphorylation and neuritic degeneration. *Proc. Natl. Acad. Sci. U. S. A.* **108**, 5819–5824 (2011).
- 86. Li, C. & Götz, J. Somatodendritic accumulation of Tau in Alzheimer's disease is promoted by Fyn-mediated local protein translation. *EMBO J.* **36**, 3120–3138 (2017).
- 87. Sperling, R. A. *et al.* The impact of amyloid-beta and tau on prospective cognitive decline in older individuals. *Ann. Neurol.* **85**, 181–193 (2019).
- 88. Hoenig, M. C. et al. Networks of tau distribution in Alzheimer's disease. Brain 141, 568–581 (2018).
- 89. Franzmeier, N. *et al.* Functional brain architecture is associated with the rate of tau accumulation in Alzheimer's disease. *Nat. Commun. 2020 111* **11**, 1–17 (2020).
- 90. Braak, H. & Braak, E. Neuropathological stageing of Alzheimer-related changes. *Acta Neuropathol.* 1991 824 82, 239–259 (1991).
- 91. Thal, D. R. *et al.* Sequence of Aβ-Protein Deposition in the Human Medial Temporal Lobe. *J. Neuropathol. Exp. Neurol.* **59**, 733–748 (2000).

- 92. Grothe, M. J. et al. In vivo staging of regional amyloid deposition. Neurology 89, 2031–2038 (2017).
- 93. Lee, W. J. *et al.* Regional Aβ-tau interactions promote onset and acceleration of Alzheimer's disease tau spreading. *Neuron* **0**, (2022).
- 94. van der Kant, R., Goldstein, L. S. B. & Ossenkoppele, R. Amyloid-β-independent regulators of tau pathology in Alzheimer disease. *Nat. Rev. Neurosci.* **21**, 21–35 (2020).
- 95. Esquerda-Canals, G., Montoliu-Gaya, L., Güell-Bosch, J. & Villegas, S. Mouse Models of Alzheimer's Disease. *J. Alzheimers. Dis.* **57**, 1171–1183 (2017).
- 96. Radde, R. *et al.* Aβ42-driven cerebral amyloidosis in transgenic mice reveals early and robust pathology. *EMBO Rep.* **7**, 940 (2006).
- 97. Oakley, H. *et al.* Intraneuronal beta-amyloid aggregates, neurodegeneration, and neuron loss in transgenic mice with five familial Alzheimer's disease mutations: potential factors in amyloid plaque formation. *J. Neurosci.* **26**, 10129–10140 (2006).
- 98. Bacioglu, M. *et al.* Neurofilament Light Chain in Blood and CSF as Marker of Disease Progression in Mouse Models and in Neurodegenerative Diseases. *Neuron* **91**, 56–66 (2016).
- 99. Gamache, J. *et al.* Factors other than hTau overexpression that contribute to tauopathy-like phenotype in rTg4510 mice. *Nat. Commun.* **10**, (2019).
- 100. Saito, T. et al. Single App knock-in mouse models of Alzheimer's disease. Nat. Neurosci. 17, 661–3 (2014).
- 101. Sato, K. et al. New App knock-in mice that accumulate wild-type human Aß as rapidly as AppNL-G-F mice exhibit intensive cored plaque pathology and neuroinflammation. (2021). doi:10.1101/2021.04.30.442122
- 102. Xia, D. *et al.* Fibrillar Aβ causes profound microglial metabolic perturbations in a novel APP knock-in mouse model. *bioRxiv* 2021.01.19.426731 (2021). doi:10.1101/2021.01.19.426731
- 103. Citron, M. *et al.* Mutation of the beta-amyloid precursor protein in familial Alzheimer's disease increases beta-protein production. *Nature* **360**, 672–674 (1992).
- 104. Haass, C. *et al.* The Swedish mutation causes early-onset Alzheimer's disease by β -secretase cleavage within the secretory pathway. *Nat. Med.* **1**, 1291–1296 (1995).
- 105. Citron, M., Teplow, D. B. & Selkoe, D. J. Generation of Amyloid Protein from Its Precursor Is Sequence Specific. *Neuron* **14**, 661–670 (1995).
- 106. Rabe, S. *et al.* The Swedish APP mutation alters the effect of genetically reduced BACE1 expression on the APP processing. *J. Neurochem.* **119**, 231–239 (2011).
- 107. Nilsberth, C. *et al.* The 'Arctic' APP mutation (E693G) causes Alzheimer's disease by enhanced Abeta protofibril formation. *Nat. Neurosci.* **4**, 887–893 (2001).
- 108. Johansson, A. S. *et al.* Physiochemical characterization of the Alzheimer's disease-related peptides A β 1–42Arctic and A β 1–42wt. *FEBS J.* **273**, 2618–2630 (2006).
- 109. Takami, M. *et al.* γ-Secretase: Successive Tripeptide and Tetrapeptide Release from the Transmembrane Domain of β-Carboxyl Terminal Fragment. *J. Neurosci.* **29**, 13042–13052 (2009).
- 110. Vigo-Pelfrey, C., Lee, D., Keim, P., Lieberburg, I. & Schenk, D. B. Rapid Communication: Characterization of β-Amyloid Peptide from Human Cerebrospinal Fluid. *J. Neurochem.* **61**, 1965–1968 (1993).
- Dovey, H. F., Suomensaari-Chrysler, S., Lieberburg, I., Sinha, S. & Keim, P. S. Cells with a familial Alzheimer's disease mutation produce authentic beta-peptide. *Neuroreport* **4**, 1039–1042 (1993).
- 112. Halverson, K., Fraser, P. E., Kirschner, D. A. & Lansbury, P. T. Molecular determinants of amyloid deposition in Alzheimer's disease: conformational studies of synthetic beta-protein fragments. *Biochemistry* **29**, 2639–2644 (1990).
- 113. Iwatsubo, T. *et al.* Visualization of A beta 42(43) and A beta 40 in senile plaques with end-specific A beta monoclonals: evidence that an initially deposited species is A beta 42(43). *Neuron* **13**, 45–53 (1994).
- 114. Jarrett, J. T., Berger, E. P. & Lansbury, P. T. The carboxy terminus of the beta amyloid protein is critical for the seeding of amyloid formation: implications for the pathogenesis of Alzheimer's disease.

- Biochemistry 32, 4693-4697 (1993).
- 115. Szaruga, M. *et al.* Alzheimer's-Causing Mutations Shift Aβ Length by Destabilizing γ-Secretase-Aβn Interactions. *Cell* **170**, 443-456.e14 (2017).
- 116. Lichtenthaler, S. F. *et al.* Mechanism of the cleavage specificity of Alzheimer's disease gamma-secretase identified by phenylalanine-scanning mutagenesis of the transmembrane domain of the amyloid precursor protein. *Proc. Natl. Acad. Sci. U. S. A.* **96**, 3053–3058 (1999).
- 117. Masuda, A. *et al.* Cognitive deficits in single App knock-in mouse models. *Neurobiol. Learn. Mem.* **135**, 73–82 (2016).
- 118. Janke, C. *et al.* Phylogenetic diversity of the expression of the microtubule-associated protein tau: implications for neurodegenerative disorders. *Mol. Brain Res.* **68**, 119–128 (1999).
- 119. Stanford, P. M. *et al.* Mutations in the tau gene that cause an increase in three repeat tau and frontotemporal dementia. *Brain* **126**, 814–826 (2003).
- 120. Delisle, M. B. *et al.* A mutation at codon 279 (N279K) in exon 10 of the Tau gene causes a tauopathy with dementia and supranuclear palsy. *Acta Neuropathol.* 1999 981 98, 62–77 (1999).
- 121. Goedert, M., Spillantini, M. G., Cairns, N. J. & Crowther, R. A. Tau proteins of Alzheimer paired helical filaments: abnormal phosphorylation of all six brain isoforms. *Neuron* **8**, 159–168 (1992).
- 122. Balusu, S. *et al.* Long noncoding RNA MEG3 activates neuronal necroptosis in Alzheimer's disease. *bioRxiv* 2022.02.18.480849 (2022). doi:10.1101/2022.02.18.480849
- 123. Espuny-Camacho, I. *et al.* Hallmarks of Alzheimer's Disease in Stem-Cell-Derived Human Neurons Transplanted into Mouse Brain. *Neuron* **93**, 1066-1081.e8 (2017).
- 124. Mathys, H. et al. Single-cell transcriptomic analysis of Alzheimer's disease. Nature 570, 332–337 (2019).
- 125. Zhou, Y. *et al.* Human and mouse single-nucleus transcriptomics reveal TREM2-dependent and TREM2-independent cellular responses in Alzheimer's disease. *Nat. Med.* **26**, 131–142 (2020).
- 126. Mancuso, R. *et al.* Stem-cell-derived human microglia transplanted in mouse brain to study human disease. *Nat. Neurosci.* **22**, 2111–2116 (2019).
- 127. Grubman, A. *et al.* A single-cell atlas of entorhinal cortex from individuals with Alzheimer's disease reveals cell-type-specific gene expression regulation. *Nat. Neurosci.* **22**, 2087–2097 (2019).
- 128. Keren-Shaul, H. *et al.* A Unique Microglia Type Associated with Restricting Development of Alzheimer's Disease. *Cell* **169**, 1276-1290.e17 (2017).
- 129. Krasemann, S. *et al.* The TREM2-APOE Pathway Drives the Transcriptional Phenotype of Dysfunctional Microglia in Neurodegenerative Diseases. *Immunity* **47**, 566-581.e9 (2017).
- 130. Srinivasan, K. *et al.* Alzheimer's Patient Microglia Exhibit Enhanced Aging and Unique Transcriptional Activation. *Cell Rep.* **31**, 107843 (2020).
- 131. Lau, S.-F., Cao, H., Fu, A. & Ip, N. Single-nucleus transcriptome analysis reveals dysregulation of angiogenic endothelial cells and neuroprotective glia in Alzheimer's disease. **117**, 25800–25809 (2020).
- 132. Takahashi, K. & Yamanaka, S. Induction of Pluripotent Stem Cells from Mouse Embryonic and Adult Fibroblast Cultures by Defined Factors. *Cell* **126**, 663–676 (2006).
- 133. Takahashi, K. *et al.* Induction of Pluripotent Stem Cells from Adult Human Fibroblasts by Defined Factors. *Cell* **131**, 861–872 (2007).
- 134. Stadtfeld, M., Nagaya, M., Utikal, J., Weir, G. & Hochedlinger, K. Induced pluripotent stem cells generated without viral integration. *Science (80-.).* **322**, 945–949 (2008).
- 135. Fusaki, N., Ban, H., Nishiyama, A., Saeki, K. & Hasegawa, M. Efficient induction of transgene-free human pluripotent stem cells using a vector based on Sendai virus, an RNA virus that does not integrate into the host genome. *Proc. Japan Acad. Ser. B* **85**, 348–362 (2009).
- 136. Okita, K., Nakagawa, M., Hyenjong, H., Ichisaka, T. & Yamanaka, S. Generation of mouse induced pluripotent stem cells without viral vectors. *Science* (80-.). **322**, 949–953 (2008).

- 137. Junying, Y. *et al.* Human induced pluripotent stem cells free of vector and transgene sequences. *Science* (80-.). **324**, 797–801 (2009).
- 138. Kim, D. *et al.* Generation of Human Induced Pluripotent Stem Cells by Direct Delivery of Reprogramming Proteins. *Cell Stem Cell* **4**, 472–476 (2009).
- 139. Warren, L. *et al.* Highly efficient reprogramming to pluripotency and directed differentiation of human cells with synthetic modified mRNA. *Cell Stem Cell* **7**, 618–630 (2010).
- 140. Anokye-Danso, F. *et al.* Highly efficient miRNA-mediated reprogramming of mouse and human somatic cells to pluripotency. *Cell Stem Cell* **8**, 376–388 (2011).
- 141. Loh, Y. H. *et al.* Generation of induced pluripotent stem cells from human blood. *Blood* **113**, 5476–5479 (2009).
- 142. Loh, Y. H. et al. Reprogramming of T cells from human peripheral blood. Cell Stem Cell 7, 15–19 (2010).
- 143. Staerk, J. *et al.* Reprogramming of human peripheral blood cells to induced pluripotent stem cells. *Cell Stem Cell* **7**, 20–24 (2010).
- 144. Seki, T. *et al.* Generation of induced pluripotent stem cells from human terminally differentiated circulating T cells. *Cell Stem Cell* **7**, 11–14 (2010).
- 145. Aasen, T. *et al.* Efficient and rapid generation of induced pluripotent stem cells from human keratinocytes. *Nat. Biotechnol. 2008 2611* **26**, 1276–1284 (2008).
- 146. Zhou, T. *et al.* Generation of Induced Pluripotent Stem Cells from Urine. *J. Am. Soc. Nephrol.* **22**, 1221 (2011).
- 147. Shi, Y., Kirwan, P., Smith, J., Robinson, H. P. C. & Livesey, F. J. Human cerebral cortex development from pluripotent stem cells to functional excitatory synapses. *Nat. Neurosci.* **15**, 477–486 (2012).
- 148. Qi, Y. *et al.* Combined small-molecule inhibition accelerates the derivation of functional cortical neurons from human pluripotent stem cells. *Nat. Biotechnol.* **35**, 154–163 (2017).
- 149. Krencik, R., Weick, J. P., Liu, Y., Zhang, Z. J. & Zhang, S. C. Specification of transplantable astroglial subtypes from human pluripotent stem cells. *Nat. Biotechnol.* **29**, 528–534 (2011).
- 150. Perriot, S. *et al.* Human Induced Pluripotent Stem Cell-Derived Astrocytes Are Differentially Activated by Multiple Sclerosis-Associated Cytokines. *Stem Cell Reports* **11**, 1199–1210 (2018).
- 151. Abud, E. M. *et al.* iPSC-Derived Human Microglia-like Cells to Study Neurological Diseases. *Neuron* **94**, 278-293.e9 (2017).
- 152. McQuade, A. *et al.* Development and validation of a simplified method to generate human microglia from pluripotent stem cells. *Mol. Neurodegener.* **13**, 1–13 (2018).
- 153. Chambers, S. M. *et al.* Highly efficient neural conversion of human ES and iPS cells by dual inhibition of SMAD signaling. *Nat. Biotechnol. 2009 273* **27**, 275–280 (2009).
- 154. Paquet, D. *et al.* Efficient introduction of specific homozygous and heterozygous mutations using CRISPR/Cas9. *Nature* **533**, 125–129 (2016).
- 155. Zhang, Y. *et al.* Rapid Single-Step Induction of Functional Neurons from Human Pluripotent Stem Cells. *Neuron* **78**, 785 (2013).
- 156. Lin, H. C. *et al.* NGN2 induces diverse neuron types from human pluripotency. *Stem Cell Reports* **16**, 2118–2127 (2021).
- 157. Luskin, M. B., Pearlman, A. L. & Sanes, J. R. Cell lineage in the cerebral cortex of the mouse studied in vivo and in vitro with a recombinant retrovirus. *Neuron* **1**, 635–647 (1988).
- 158. Bonni, A. *et al.* Regulation of gliogenesis in the central nervous system by the JAK-STAT signaling pathway. *Science* **278**, 477–483 (1997).
- 159. Johe, K. K., Hazel, T. G., Muller, T., Dugich-Djordjevic, M. M. & McKay, R. D. G. Single factors direct the differentiation of stem cells from the fetal and adult central nervous system. *Genes Dev.* **10**, 3129–3140 (1996).

- 160. Nakashima, K. *et al.* Synergistic Signaling in Fetal Brain by STAT3-Smad1 Complex Bridged by p300. *Science* (80-.). **284**, 479–482 (1999).
- 161. Perriot, S., Canales, M., Mathias, A. & Du Pasquier, R. Differentiation of functional astrocytes from human-induced pluripotent stem cells in chemically defined media. *STAR Protoc.* **2**, 100902 (2021).
- 162. Foo, L. C. *et al.* Development of a Method for the Purification and Culture of Rodent Astrocytes. *Neuron* **71**, 799–811 (2011).
- 163. Li, X. et al. Fast Generation of Functional Subtype Astrocytes from Human Pluripotent Stem Cells. Stem cell reports 11, 998–1008 (2018).
- 164. Tchieu, J. *et al.* NFIA is a gliogenic switch enabling rapid derivation of functional human astrocytes from pluripotent stem cells. *Nat. Biotechnol.* **37**, 267–275 (2019).
- 165. Canals, I. *et al.* Rapid and efficient induction of functional astrocytes from human pluripotent stem cells. *Nat. Methods* **15**, 693–696 (2018).
- 166. Neyrinck, K. *et al.* SOX9-induced Generation of Functional Astrocytes Supporting Neuronal Maturation in an All-human System. *Stem Cell Rev. Reports* **17**, 1855–1873 (2021).
- 167. Ginhoux, F. *et al.* Fate mapping analysis reveals that adult microglia derive from primitive macrophages. *Science* (80-.). **330**, 841–845 (2010).
- 168. Schulz, C. *et al.* A lineage of myeloid cells independent of myb and hematopoietic stem cells. *Science (80-.).* **335**, 86–90 (2012).
- 169. Haenseler, W. *et al.* A Highly Efficient Human Pluripotent Stem Cell Microglia Model Displays a Neuronal-Co-culture-Specific Expression Profile and Inflammatory Response. *Stem Cell Reports* **8**, 1727–1742 (2017).
- 170. Muffat, J. *et al.* Efficient derivation of microglia-like cells from human pluripotent stem cells. *Nat. Med.* **22**, 1358–1367 (2016).
- 171. Douvaras, P. et al. Directed Differentiation of Human Pluripotent Stem Cells to Microglia. Stem Cell Reports 8, 1516–1524 (2017).
- 172. Pandya, H. *et al.* Differentiation of human and murine induced pluripotent stem cells to microglia-like cells. *Nat. Neurosci.* **20**, 753–759 (2017).
- 173. McQuade, A. & Blurton-Jones, M. Microglia in Alzheimer's Disease: Exploring How Genetics and Phenotype Influence Risk. *Journal of Molecular Biology* **431**, 1805–1817 (2019).
- 174. Chen, S. W. *et al.* Efficient conversion of human induced pluripotent stem cells into microglia by defined transcription factors. *Stem Cell Reports* **16**, 1363–1380 (2021).
- 175. Kuijlaars, J. *et al.* Sustained synchronized neuronal network activity in a human astrocyte co-culture system. *Sci. Rep.* **6**, (2016).
- 176. Klapper, S. D. *et al.* Astrocyte lineage cells are essential for functional neuronal differentiation and synapse maturation in human iPSC-derived neural networks. *Glia* (2019). doi:10.1002/glia.23666
- 177. Hedegaard, A. *et al.* Pro-maturational Effects of Human iPSC-Derived Cortical Astrocytes upon iPSC-Derived Cortical Neurons. *Stem Cell Reports* **4**, 632–644 (2020).
- 178. Antoni, D., Burckel, H., Josset, E. & Noel, G. Three-Dimensional Cell Culture: A Breakthrough in Vivo. *Int. J. Mol. Sci.* **16**, 5517 (2015).
- 179. Gaspard, N. et al. An intrinsic mechanism of corticogenesis from embryonic stem cells. *Nat. 2008* 4557211 **455**, 351–357 (2008).
- 180. Chiaradia, I. & Lancaster, M. A. Brain organoids for the study of human neurobiology at the interface of in vitro and in vivo. *Nature Neuroscience* **23**, 1496–1508 (2020).
- 181. Lancaster, M. A. *et al.* Cerebral organoids model human brain development and microcephaly. *Nat. 2013* 5017467 **501**, 373–379 (2013).
- 182. Quadrato, G. *et al.* Cell diversity and network dynamics in photosensitive human brain organoids. *Nature* **545**, 48–53 (2017).

- 183. Eiraku, M. *et al.* Self-Organized Formation of Polarized Cortical Tissues from ESCs and Its Active Manipulation by Extrinsic Signals. *Cell Stem Cell* **3**, 519–532 (2008).
- 184. Kadoshima, T. *et al.* Self-organization of axial polarity, inside-out layer pattern, and species-specific progenitor dynamics in human ES cell-derived neocortex. *Proc. Natl. Acad. Sci. U. S. A.* **110**, 20284–20289 (2013).
- 185. Pasca, A. M. *et al.* Functional cortical neurons and astrocytes from human pluripotent stem cells in 3D culture. *Nat. Methods 2015 127* **12**, 671–678 (2015).
- 186. Simão, D. *et al.* Recapitulation of Human Neural Microenvironment Signatures in iPSC-Derived NPC 3D Differentiation. *Stem Cell Reports* **11**, 552–564 (2018).
- 187. Jorfi, M., D'Avanzo, C., Tanzi, R. E., Kim, D. Y. & Irimia, D. Human Neurospheroid Arrays for In Vitro Studies of Alzheimer's Disease. *Sci. Rep.* **8**, 2450 (2018).
- 188. Krencik, R. *et al.* Systematic Three-Dimensional Coculture Rapidly Recapitulates Interactions between Human Neurons and Astrocytes. *Stem Cell Reports* **9**, 1745–1753 (2017).
- 189. Miguel, L. *et al.* Detection of all adult Tau isoforms in a 3D culture model of iPSC-derived neurons. *Stem Cell Res.* **40**, 101541 (2019).
- 190. Hernández-Sapiéns, M. A. *et al.* A Three-Dimensional Alzheimer's Disease Cell Culture Model Using iPSC-Derived Neurons Carrying A246E Mutation in PSEN1. *Front. Cell. Neurosci.* **14**, (2020).
- 191. de Leeuw, S. M. *et al.* Increased maturation of iPSC-derived neurons in a hydrogel-based 3D culture. *J. Neurosci. Methods* **360**, 109254 (2021).
- 192. Zhang, D. *et al.* A 3D Alzheimer's disease culture model and the induction of P21-activated kinase mediated sensing in iPSC derived neurons. *Biomaterials* **35**, 1420–1428 (2014).
- 193. Lau, L. W., Cua, R., Keough, M. B., Haylock-Jacobs, S. & Yong, V. W. Pathophysiology of the brain extracellular matrix: a new target for remyelination. *Nat. Rev. Neurosci.* **14**, 722–729 (2013).
- 194. Yagi, T. *et al.* Modeling familial Alzheimer's disease with induced pluripotent stem cells. *Hum. Mol. Genet.* **20**, 4530–4539 (2011).
- 195. Kondo, T. *et al.* Modeling Alzheimer's disease with iPSCs reveals stress phenotypes associated with intracellular Aβ and differential drug responsiveness. *Cell Stem Cell* **12**, 487–496 (2013).
- 196. Israel, M. A. *et al.* Probing sporadic and familial Alzheimer's disease using induced pluripotent stem cells. *Nature* **482**, 216–220 (2012).
- 197. Woodruff, G. *et al.* The Presenilin-1 δ E9 Mutation Results in Reduced γ -Secretase Activity, but Not Total Loss of PS1 Function, in Isogenic Human Stem Cells. *Cell Rep.* **5**, 974–985 (2013).
- 198. Birnbaum, J. H. *et al.* Oxidative stress and altered mitochondrial protein expression in the absence of amyloid-β and tau pathology in iPSC-derived neurons from sporadic Alzheimer's disease patients. *Stem Cell Res.* **27**, 121–130 (2018).
- 199. Jones, V. C., Atkinson-Dell, R., Verkhratsky, A. & Mohamet, L. Aberrant iPSC-derived human astrocytes in Alzheimer's disease. *Cell Death Dis.* **8**, (2017).
- 200. Oksanen, M. *et al.* PSEN1 Mutant iPSC-Derived Model Reveals Severe Astrocyte Pathology in Alzheimer's Disease. *Stem Cell Reports* **9**, 1885–1897 (2017).
- 201. Corder, E. H. *et al.* Gene dose of apolipoprotein E type 4 allele and the risk of Alzheimer's disease in late onset families. *Science* (80-.). **261**, 921–923 (1993).
- 202. Coon, K. D. *et al.* A high-density whole-genome association study reveals that APOE is the major susceptibility gene for sporadic late-onset Alzheimer's disease. *J. Clin. Psychiatry* **68**, 613–618 (2007).
- 203. Lin, Y. T. *et al.* APOE4 Causes Widespread Molecular and Cellular Alterations Associated with Alzheimer's Disease Phenotypes in Human iPSC-Derived Brain Cell Types. *Neuron* **98**, 1141-1154.e7 (2018).
- 204. Konttinen, H. *et al.* PSEN1ΔE9, APPswe, and APOE4 Confer Disparate Phenotypes in Human iPSC-Derived Microglia. *Stem Cell Reports* **13**, 669–683 (2019).
- 205. Guttikonda, S. & Studer, L. Fully defined hPSC-derived microglia and tri-culture system model C3

- production in AD. Nat. Neurosci. 343–354 (2021).
- 206. Klimmt, J., Dannert, A. & Paquet, D. Neurodegeneration in a dish: advancing human stem-cell-based models of Alzheimer's disease. *Curr. Opin. Neurobiol.* **61**, 96–104 (2020).
- 207. Choi, S. H. *et al.* A three-dimensional human neural cell culture model of Alzheimer's disease. *Nature* **515**, 274–278 (2014).
- 208. Cole, G., Neal, J. W., Singhrao, S. K., Jasani, B. & Newman, G. R. The distribution of amyloid plaques in the cerebellum and brain stem in Down's syndrome and Alzheimer's disease: a light microscopical analysis. *Acta Neuropathol.* **85**, 542–552 (1993).
- 209. Raja, W. K. *et al.* Self-Organizing 3D Human Neural Tissue Derived from Induced Pluripotent Stem Cells Recapitulate Alzheimer's Disease Phenotypes. *PLoS One* **11**, e0161969 (2016).
- 210. Gonzalez, C. *et al.* Modeling amyloid beta and tau pathology in human cerebral organoids. *Mol. Psychiatry* **23**, 2363–2374 (2018).
- 211. Zhao, J. *et al.* APOE4 exacerbates synapse loss and neurodegeneration in Alzheimer's disease patient iPSC-derived cerebral organoids. *Nat. Commun.* **11**, 5540 (2020).
- 212. Velasco, S. *et al.* Individual brain organoids reproducibly form cell diversity of the human cerebral cortex. *Nature* **570**, 523–527 (2019).
- 213. Tanaka, Y., Cakir, B., Xiang, Y., Sullivan, G. J. & Park, I. H. Synthetic Analyses of Single-Cell Transcriptomes from Multiple Brain Organoids and Fetal Brain. *Cell Rep.* **30**, 1682-1689.e3 (2020).
- 214. Renner, M. *et al.* Self-organized developmental patterning and differentiation in cerebral organoids. *EMBO J.* **36**, 1316–1329 (2017).
- 215. Qian, X. *et al.* Sliced Human Cortical Organoids for Modeling Distinct Cortical Layer Formation. *Cell Stem Cell* **26**, 766-781.e9 (2020).
- 216. Giandomenico, S. L. *et al.* Cerebral organoids at the air–liquid interface generate diverse nerve tracts with functional output. *Nat. Neurosci.* **22**, 669–679 (2019).
- 217. Kanton, S. *et al.* Organoid single-cell genomic atlas uncovers human-specific features of brain development. *Nat. 2019 5747778* **574**, 418–422 (2019).
- 218. Benito-Kwiecinski, S. *et al.* An early cell shape transition drives evolutionary expansion of the human forebrain. *Cell* **184**, 2084-2102.e19 (2021).
- 219. Balusu, S. *et al.* Long noncoding RNA MEG3 activates neuronal necroptosis in Alzheimer's disease. *bioRxiv* 2022.02.18.480849 (2022). doi:10.1101/2022.02.18.480849
- 220. Preman, P. *et al.* Human iPSC-derived astrocytes transplanted into the mouse brain undergo morphological changes in response to amyloid-β plaques. *Mol. Neurodegener.* **16**, 1–18 (2021).
- 221. Hasselmann, J. *et al.* Development of a Chimeric Model to Study and Manipulate Human Microglia In Vivo. *Neuron* (2019). doi:10.1016/j.neuron.2019.07.002
- 222. Claes, C. *et al.* Plaque-associated human microglia accumulate lipid droplets in a chimeric model of Alzheimer's disease. *Mol. Neurodegener.* **16**, 50 (2021).
- 223. Bettcher, B. M., Tansey, M. G., Dorothée, G. & Heneka, M. T. Peripheral and central immune system crosstalk in Alzheimer disease a research prospectus. *Nat. Rev. Neurol.* 2021 1711 17, 689–701 (2021).
- 224. Parajuli, B. *et al.* Transnasal transplantation of human induced pluripotent stem cell-derived microglia to the brain of immunocompetent mice. *Glia* **69**, 2332–2348 (2021).
- 225. Barrangou, R. *et al.* CRISPR provides acquired resistance against viruses in prokaryotes. *Science (80-.).* **315**, 1709–1712 (2007).
- 226. Brouns, S. J. J. et al. Small CRISPR RNAs Guide Antiviral Defense in Prokaryotes. Science 321, 960 (2008).
- 227. Cong, L. et al. Multiplex genome engineering using CRISPR/Cas systems. Science 339, 819–823 (2013).
- 228. Mali, P. et al. RNA-guided human genome engineering via Cas9. Science (80-.). 339, 823–826 (2013).
- 229. Gasiunas, G., Barrangou, R., Horvath, P. & Siksnys, V. Cas9-crRNA ribonucleoprotein complex mediates

- specific DNA cleavage for adaptive immunity in bacteria. *Proc. Natl. Acad. Sci. U. S. A.* **109**, E2579–E2586 (2012).
- 230. Jinek, M. *et al.* A programmable dual-RNA-guided DNA endonuclease in adaptive bacterial immunity. *Science* **337**, 816–821 (2012).
- 231. Mojica, F. J. M., Díez-Villaseñor, C., García-Martínez, J. & Almendros, C. Short motif sequences determine the targets of the prokaryotic CRISPR defence system. *Microbiology* **155**, 733–740 (2009).
- 232. Zuris, J. A. *et al.* Efficient Delivery of Genome-Editing Proteins In Vitro and In Vivo. *Nat. Biotechnol.* **33**, 73 (2015).
- 233. Roth, D. B., Wilson, J. H. & McLean, M. Nonhomologous recombination in mammalian cells: role for short sequence homologies in the joining reaction. *Mol. Cell. Biol.* **6**, 4295 (1986).
- 234. Wood, A. J. *et al.* Targeted genome editing across species using ZFNs and TALENs. *Science (80-.).* **333**, 307 (2011).
- 235. Kwart, D. *et al.* A Large Panel of Isogenic APP and PSEN1 Mutant Human iPSC Neurons Reveals Shared Endosomal Abnormalities Mediated by APP β-CTFs, Not Aβ. *Neuron* (2019). doi:10.1016/j.neuron.2019.07.010
- 236. Concordet, J. P. & Haeussler, M. CRISPOR: Intuitive guide selection for CRISPR/Cas9 genome editing experiments and screens. *Nucleic Acids Res.* **46**, W242–W245 (2018).
- 237. Brinkman, E. K., Chen, T., Amendola, M. & Van Steensel, B. Easy quantitative assessment of genome editing by sequence trace decomposition. *Nucleic Acids Res.* **42**, 1–8 (2014).
- 238. Weisheit, I. *et al.* Simple and reliable detection of CRISPR-induced on-target effects by qgPCR and SNP genotyping. *Nat. Protoc.* (2021). doi:10.1038/s41596-020-00481-2
- 239. Reifschneider, A. *et al.* Loss of TREM2 rescues hyperactivation of microglia, but not lysosomal deficits and neurotoxicity in models of progranulin deficiency. *EMBO J.* **41**, e109108 (2022).
- 240. Parhizkar, S. *et al.* Loss of TREM2 function increases amyloid seeding but reduces plaque-associated ApoE. *Nat. Neurosci.* **22**, 191–204 (2019).
- 241. Schindelin, J. *et al.* Fiji: an open-source platform for biological-image analysis. *Nat. Methods 2012 97* **9**, 676–682 (2012).
- 242. Wang, Y. *et al.* SynQuant: an automatic tool to quantify synapses from microscopy images. *Bioinformatics* **36**, 1599–1606 (2020).
- 243. Karlsson, J. O., Ostwald, K., Kåbjörn, C. & Andersson, M. A Method for Protein Assay in Laemmli Buffer. *Anal. Biochem.* **219**, 144–146 (1994).
- 244. Schägger, H. & Von Jagow, G. *Tricine-Sodium Dodecyl Sulfate-Polyacrylamide Gel Electrophoresis for the Separation of Proteins in the Range from 1 to 100 kDa*. (1987).
- 245. Schägger, H. Tricine–SDS-PAGE. *Nat. Protoc. 2006 11* **1**, 16–22 (2006).
- 246. Satija, R., Farrell, J. A., Gennert, D., Schier, A. F. & Regev, A. Spatial reconstruction of single-cell gene expression data. *Nat. Biotechnol.* 2015 335 **33**, 495–502 (2015).
- 247. Sielaff, M. *et al.* Evaluation of FASP, SP3, and iST Protocols for Proteomic Sample Preparation in the Low Microgram Range. *J. Proteome Res.* **16**, 4060–4072 (2017).
- 248. Meier, F. *et al.* diaPASEF: parallel accumulation—serial fragmentation combined with data-independent acquisition. *Nat. Methods 2020 1712* **17**, 1229–1236 (2020).
- 249. Demichev, V., Messner, C. B., Vernardis, S. I., Lilley, K. S. & Ralser, M. DIA-NN: neural networks and interference correction enable deep proteome coverage in high throughput. *Nat. Methods* 2019 171 17, 41–44 (2019).
- 250. Tyanova, S. *et al.* The Perseus computational platform for comprehensive analysis of (prote)omics data. *Nat. Methods 2016 139* **13**, 731–740 (2016).
- 251. TCW, J. *et al.* An Efficient Platform for Astrocyte Differentiation from Human Induced Pluripotent Stem Cells. *Stem Cell Reports* **9**, 600–614 (2017).

- 252. Shi, Y., Kirwan, P. & Livesey, F. J. Directed differentiation of human pluripotent stem cells to cerebral cortex neurons and neural networks. *Nat. Protoc.* **7**, 1836–1846 (2012).
- 253. Schitine, C., Nogaroli, L., Costa, M. R. & Hedin-Pereira, C. Astrocyte heterogeneity in the brain: From development to disease. *Front. Cell. Neurosci.* **9**, 76 (2015).
- 254. Kleinman, H. K. *et al.* Isolation and characterization of type IV procollagen, laminin, and heparan sulfate proteoglycan from the EHS sarcoma. *Biochemistry* **21**, 6188–6193 (1982).
- 255. Corning. Corning ® Matrigel® Matrix Frequently Asked Questions. https://www.corning.com/catalog/cls/documents/faqs
- 256. Gerdes, J., Schwab, U., Lemke, H. & Stein, H. Production of a mouse monoclonal antibody reactive with a human nuclear antigen associated with cell proliferation. *Int. J. Cancer* **31**, 13–20 (1983).
- 257. Gerdes, J. *et al.* Cell cycle analysis of a cell proliferation-associated human nuclear antigen defined by the monoclonal antibody Ki-67. *J. Immunol.* **133**, (1984).
- 258. Gorczyca, W., Traganos, F., Jesionowska, H. & Darzynkiewicz, Z. Presence of DNA Strand Breaks and Increased Sensitivity of DNA in Situ to Denaturation in Abnormal Human Sperm Cells: Analogy to Apoptosis of Somatic Cells. *Exp. Cell Res.* **207**, 202–205 (1993).
- 259. Mansour, A. A. *et al.* An in vivo model of functional and vascularized human brain organoids. *Nat. Biotechnol.* **36**, 432–441 (2018).
- 260. Barros, C. S., Franco, S. J. & Müller, U. Extracellular Matrix: Functions in the nervous system. *Cold Spring Harb. Perspect. Biol.* **3**, 1–24 (2011).
- 261. Rauti, R., Renous, N. & Maoz, B. M. Mimicking the Brain Extracellular Matrix in Vitro: A Review of Current Methodologies and Challenges. *Isr. J. Chem.* **60**, 1141–1151 (2020).
- 262. Miller, J. A. *et al.* Transcriptional landscape of the prenatal human brain. *Nat. 2014 5087495* **508**, 199–206 (2014).
- 263. Paolicelli, R. C. *et al.* Synaptic pruning by microglia is necessary for normal brain development. *Science* (80-.). **333**, 1456–1458 (2011).
- 264. Amps, K. *et al.* Screening a large, ethnically diverse population of human embryonic stem cells identifies a chromosome 20 minimal amplicon that confers a growth advantage. *Nat. Biotechnol.* **29**, 1132 (2011).
- 265. Bai, H. *et al.* Bcl-xL enhances single-cell survival and expansion of human embryonic stem cells without affecting self-renewal. *Stem Cell Res.* **8**, 26–37 (2012).
- Weisheit, I. *et al.* Detection of Deleterious On-Target Effects after HDR-Mediated CRISPR Editing. *Cell Rep.* **31**, 107689 (2020).
- 267. Parhizkar, S. & Holtzman, D. M. APOE mediated neuroinflammation and neurodegeneration in Alzheimer's disease. *Semin. Immunol.* 101594 (2022). doi:10.1016/J.SMIM.2022.101594
- 268. Iwata, N. *et al.* Presynaptic Localization of Neprilysin Contributes to Efficient Clearance of Amyloid-β Peptide in Mouse Brain. *J. Neurosci.* **24**, 991–998 (2004).
- 269. Mazaheri, F. *et al.* TREM2 deficiency impairs chemotaxis and microglial responses to neuronal injury. *EMBO Rep.* **18**, 1186–1198 (2017).
- 270. McQuade, A. *et al.* Gene expression and functional deficits underlie TREM2-knockout microglia responses in human models of Alzheimer's disease. *Nat. Commun.* **11**, 5370 (2020).
- 271. Bassil, R. *et al.* Improved modeling of human AD with an automated culturing platform for iPSC neurons, astrocytes and microglia. *Nat. Commun.* **12**, 5220 (2021).
- 272. Sposito, T. *et al.* Developmental regulation of tau splicing is disrupted in stem cell-derived neurons from frontotemporal dementia patients with the 10 + 16 splice-site mutation in MAPT. *Hum. Mol. Genet.* **24**, 5260–5269 (2015).
- 273. Bhaduri, A. *et al.* Cell stress in cortical organoids impairs molecular subtype specification. *Nature* **578**, 142–148 (2020).
- 274. Vértesy, Á. et al. Cellular stress in brain organoids is limited to a distinct and bioinformatically removable

- subpopulation. bioRxiv 2022.03.11.483643 (2022). doi:10.1101/2022.03.11.483643
- 275. Mizuno, T. *et al.* Interleukin-34 Selectively Enhances the Neuroprotective Effects of Microglia to Attenuate Oligomeric Amyloid-β Neurotoxicity. *Am. J. Pathol.* **179**, 2016 (2011).
- 276. Leite de Sampaio e Spohr, T. C., Martinez, R., Da Silva, E. F., Moura Neto, V. & Alcantara Gomes, F. C. Neuro–glia interaction effects on GFAP gene: a novel role for transforming growth factor-β1. *Eur. J. Neurosci.* **16**, 2059–2069 (2002).
- 277. Hao, C., Guilbert, L. J. & Fedoroff, S. Production of colony-stimulating factor-1 (CSF-1) by mouse astroglia in vitro. *J. Neurosci. Res.* **27**, 314–323 (1990).
- 278. Nave, K. A. Myelination and the trophic support of long axons. *Nat. Rev. Neurosci. 2010 114* **11**, 275–283 (2010).
- 279. Nasrabady, S. E., Rizvi, B., Goldman, J. E. & Brickman, A. M. White matter changes in Alzheimer's disease: a focus on myelin and oligodendrocytes. *Acta Neuropathol. Commun.* **6**, (2018).
- 280. Skaper, S. D. *et al.* Oligodendrocytes are a novel source of amyloid peptide generation. *Neurochem. Res.* **34**, 2243–2250 (2009).
- 281. Depp, C. *et al.* Ageing-associated myelin dysfunction drives amyloid deposition in mouse models of Alzheimer's disease. *bioRxiv* 2021.07.31.454562 (2021). doi:10.1101/2021.07.31.454562
- 282. Marton, R. M. *et al.* Differentiation and maturation of oligodendrocytes in human three-dimensional neural cultures. *Nat. Neurosci.* **22**, 484–491 (2019).
- 283. Madhavan, M. *et al.* Induction of myelinating oligodendrocytes in human cortical spheroids. *Nat. Methods 2018 159* **15**, 700–706 (2018).
- 284. Kim, H. *et al.* Pluripotent Stem Cell-Derived Cerebral Organoids Reveal Human Oligodendrogenesis with Dorsal and Ventral Origins. *Stem Cell Reports* **12**, 890–905 (2019).
- 285. Jakovcevski, I., Filipovic, R., Mo, Z., Rakic, S. & Zecevic, N. Oligodendrocyte Development and the Onset of Myelination in the Human Fetal Brain. *Front. Neuroanat.* **3**, (2009).
- 286. Miller, D. J. *et al.* Prolonged myelination in human neocortical evolution. *Proc. Natl. Acad. Sci. U. S. A.* **109**, 16480–16485 (2012).
- 287. James, O. G. *et al.* iPSC-derived myelinoids to study myelin biology of humans. *Dev. Cell* **56**, 1346–1358 (2021).
- 288. Weidenheim, K. M., Epshteyn, I., Rashbaum, W. K. & Lyman, W. D. Neuroanatomical localization of myelin basic protein in the late first and early second trimester human foetal spinal cord and brainstem. *J. Neurocytol.* 1993 227 22, 507–516 (1993).
- 289. Hagemeyer, N. *et al.* Microglia contribute to normal myelinogenesis and to oligodendrocyte progenitor maintenance during adulthood. *Acta Neuropathol.* **134**, 441–458 (2017).
- 290. Wlodarczyk, A. *et al.* A novel microglial subset plays a key role in myelinogenesis in developing brain. *EMBO J.* **36**, 3292–3308 (2017).
- 291. Wimmer, R. A. *et al.* Human blood vessel organoids as a model of diabetic vasculopathy. *Nature* **565**, 505–510 (2019).
- 292. Wimmer, R. A., Leopoldi, A., Aichinger, M., Kerjaschki, D. & Penninger, J. M. Generation of blood vessel organoids from human pluripotent stem cells. *Nat. Protoc.* **14**, 3082–3100 (2019).
- 293. Vila Cuenca, M. *et al.* Engineered 3D vessel-on-chip using hiPSC-derived endothelial- and vascular smooth muscle cells. *Stem Cell Reports* **16**, 2159–2168 (2021).
- 294. Campisi, M. *et al.* 3D self-organized microvascular model of the human blood-brain barrier with endothelial cells, pericytes and astrocytes. *Biomaterials* **180**, 117–129 (2018).
- 295. Lyu, Z. *et al.* A neurovascular-unit-on-a-chip for the evaluation of the restorative potential of stem cell therapies for ischaemic stroke. *Nat. Biomed. Eng. 2021 58* **5**, 847–863 (2021).
- 296. Marion, R. M. *et al.* Telomeres Acquire Embryonic Stem Cell Characteristics in Induced Pluripotent Stem Cells. *Cell Stem Cell* **4**, 141–154 (2009).

- 297. Suhr, S. T. et al. Mitochondrial Rejuvenation After Induced Pluripotency. PLoS One 5, e14095 (2010).
- 298. Prigione, A., Fauler, B., Lurz, R., Lehrach, H. & Adjaye, J. The Senescence-Related Mitochondrial/Oxidative Stress Pathway is Repressed in Human Induced Pluripotent Stem Cells. *Stem Cells* 28, 721–733 (2010).
- 299. Horvath, S. DNA methylation age of human tissues and cell types. Genome Biol. 14, (2013).
- 300. Weidner, C. I. *et al.* Aging of blood can be tracked by DNA methylation changes at just three CpG sites. *Genome Biol.* **15**, (2014).
- 301. Miller, J. D. *et al.* Human iPSC-based modeling of late-onset disease via progerin-induced aging. *Cell Stem Cell* **13**, 691–705 (2013).
- 302. Hergenreder, E. *et al.* Combined small molecule treatment accelerates timing of maturation in human pluripotent stem cell-derived neurons. *bioRxiv* 2022.06.02.494616 (2022). doi:10.1101/2022.06.02.494616
- 303. Vierbuchen, T. *et al.* Direct conversion of fibroblasts to functional neurons by defined factors. *Nature* **463**, 1035–1041 (2010).
- 304. Ladewig, J. *et al.* Small molecules enable highly efficient neuronal conversion of human fibroblasts. *Nat. Methods* **9**, 575–578 (2012).
- 305. Liu, M. L. *et al.* Small molecules enable neurogenin 2 to efficiently convert human fibroblasts into cholinergic neurons. *Nat. Commun.* **4**, (2013).
- 306. Mertens, J. *et al.* Directly Reprogrammed Human Neurons Retain Aging-Associated Transcriptomic Signatures and Reveal Age-Related Nucleocytoplasmic Defects. *Cell Stem Cell* **17**, 705–718 (2015).
- 307. Hu, W. *et al.* Direct Conversion of Normal and Alzheimer's Disease Human Fibroblasts into Neuronal Cells by Small Molecules. *Cell Stem Cell* **17**, 204–212 (2015).
- 308. Ohgidani, M. *et al.* Direct induction of ramified microglia-like cells from human monocytes: Dynamic microglial dysfunction in Nasu-Hakola disease. *Sci. Rep.* **4**, (2014).
- 309. Mertens, J. *et al.* Age-dependent instability of mature neuronal fate in induced neurons from Alzheimer's patients. *Cell Stem Cell* 1533–1548 (2021). doi:10.1016/j.stem.2021.04.004
- 310. Meyer, K. *et al.* Direct conversion of patient fibroblasts demonstrates non-cell autonomous toxicity of astrocytes to motor neurons in familial and sporadic ALS. *Proc. Natl. Acad. Sci. U. S. A.* **111**, 829–832 (2014).
- 311. Gatto, N. *et al.* Directly converted astrocytes retain the ageing features of the donor fibroblasts and elucidate the astrocytic contribution to human CNS health and disease. *Aging Cell* **20**, e13281 (2021).
- 312. Wisniewski, T. & Drummond, E. APOE-amyloid interaction: Therapeutic targets. *Neurobiol. Dis.* **138**, (2020).
- 313. Chung, H., Brazil, M. I., Soe, T. T. & Maxfield, F. R. Uptake, degradation, and release of fibrillar and soluble forms of Alzheimer's amyloid beta-peptide by microglial cells. *J. Biol. Chem.* **274**, 32301–32308 (1999).
- 314. Su, Y. & Chang, P. T. Acidic pH promotes the formation of toxic fibrils from β-amyloid peptide. *Brain Res.* **893**, 287–291 (2001).
- 315. Joshi, P. *et al.* Microglia convert aggregated amyloid-β into neurotoxic forms through the shedding of microvesicles. *Cell Death Differ. 2014 214 21*, 582–593 (2013).
- 316. Stevens, B. *et al.* The Classical Complement Cascade Mediates CNS Synapse Elimination. *Cell* **131**, 1164–1178 (2007).
- 317. Hong, S. *et al.* Complement and microglia mediate early synapse loss in Alzheimer mouse models. *Science* (80-.). **352**, 712–716 (2016).
- 318. Liu, Y. *et al.* LPS receptor (CD14): a receptor for phagocytosis of Alzheimer's amyloid peptide. *Brain* **128**, 1778–1789 (2005).
- 319. Reed-Geaghan, E. G., Reed, Q. W., Cramer, P. E. & Landreth, G. E. Deletion of CD14 Attenuates Alzheimer's Disease Pathology by Influencing the Brain's Inflammatory Milieu. *J. Neurosci.* **30**, 15369–15373 (2010).

- 320. Adachi, H. & Tsujimoto, M. FEEL-1, a Novel Scavenger Receptor with in Vitro Bacteria-binding and Angiogenesis-modulating Activities. *J. Biol. Chem.* **277**, 34264–34270 (2002).
- 321. Tamura, Y. *et al.* FEEL-1 and FEEL-2 Are Endocytic Receptors for Advanced Glycation End Products. *J. Biol. Chem.* **278**, 12613–12617 (2003).
- 322. Li, F. & Zhang, H. Lysosomal Acid Lipase in Lipid Metabolism and beyond. *Arterioscler. Thromb. Vasc. Biol.* **39**, 850–856 (2019).
- 323. Alhadeff, J. A., Miller, A. L., Wenaas, H., Vedvick, T. & O'Brien, J. S. Human liver alpha-L-fucosidase. Purification, characterization, and immunochemical studies. *J. Biol. Chem.* **250**, 7106–7113 (1975).
- 324. Fukushima, H., De Wet, J. R. & O'Brien, J. S. Molecular cloning of a cDNA for human α-L-fucosidase. *Proc. Natl. Acad. Sci. U. S. A.* **82**, 1262–1265 (1985).
- 325. Yadati, T., Houben, T., Bitorina, A. & Shiri-Sverdlov, R. The Ins and Outs of Cathepsins: Physiological Function and Role in Disease Management. *Cells* **9**, (2020).
- 326. Morimoto, S., Yamamotot, Y., O'brient, J. S. & Kishimoto, Y. Distribution of saposin proteins (sphingolipid activator proteins) in lysosomal storage and other diseases. *Proc. Nati. Acad. Sci. USA* **87**, 3493–3497 (1990).
- 327. Yin, F. Lipid metabolism and Alzheimer's disease: clinical evidence, mechanistic link and therapeutic promise. *FEBS J.* (2022). doi:10.1111/FEBS.16344
- 328. Wang, C., Telpoukhovskaia, M. A., Bahr, B. A., Chen, X. & Gan, L. Endo-lysosomal dysfunction: a converging mechanism in neurodegenerative diseases. *Curr. Opin. Neurobiol.* **48**, 52–58 (2018).
- 329. Johnson, E. C. B. *et al.* Large-scale deep multi-layer analysis of Alzheimer's disease brain reveals strong proteomic disease-related changes not observed at the RNA level. *Nat. Neurosci. 2022 252* **25**, 213–225 (2022).
- 330. Carlyle, B. C. *et al.* A multiregional proteomic survey of the postnatal human brain. *Nat. Neurosci. 2017 2012* **20**, 1787–1795 (2017).
- 331. Monasor, L. S. *et al.* Fibrillar aβ triggers microglial proteome alterations and dysfunction in alzheimer mouse models. *Elife* **9**, 1–33 (2020).
- 332. Quartey, M. O. *et al.* The A β (1–38) peptide is a negative regulator of the A β (1–42) peptide implicated in Alzheimer disease progression. *Sci. Reports 2021 111* **11**, 1–17 (2021).
- 333. Braun, G. A., Dear, A. J., Sanagavarapu, K., Zetterberg, H. & Linse, S. Amyloid-β peptide 37, 38 and 40 individually and cooperatively inhibit amyloid-β 42 aggregation. *Chem. Sci.* (2022). doi:10.1039/D1SC02990H
- 334. Cullen, N. *et al.* Association of CSF Aβ 38 Levels With Risk of Alzheimer Disease-Related Decline. *Neurology* **98**, E958–E967 (2022).
- 335. Moehlmann, T. *et al.* Presenilin-1 mutations of leucine 166 equally affect the generation of the Notch and APP intracellular domains independent of their effect on Aβ42 production. *Proc. Natl. Acad. Sci. U. S. A.* **99**, 8025–8030 (2002).
- 336. Chen, C. Y. *et al.* Inhibition of Notch signaling facilitates the differentiation of human-induced pluripotent stem cells into neural stem cells. *Mol. Cell. Biochem.* **395**, 291–298 (2014).
- 337. Woo, S. M. *et al.* Notch signaling is required for maintaining stem-cell features of neuroprogenitor cells derived from human embryonic stem cells. *BMC Neurosci.* **10**, 97 (2009).
- 338. Basun, H. *et al.* Clinical and Neuropathological Features of the Arctic APP Gene Mutation Causing Early-Onset Alzheimer Disease. *Arch. Neurol.* **65**, 499 (2008).
- 339. Kalimo, H. *et al.* The Arctic AβPP mutation leads to Alzheimer's disease pathology with highly variable topographic deposition of differentially truncated Aβ. *Acta Neuropathol. Commun.* **2**, 1–19 (2014).
- 340. Abutbul, S. *et al.* TGF-β signaling through SMAD2/3 induces the quiescent microglial phenotype within the CNS environment. *Glia* **60**, 1160–1171 (2012).
- 341. Suzumura, A., Sawada, M., Yamamoto, H. & Marunouchi, T. Transforming growth factor-beta suppresses

- activation and proliferation of microglia in vitro. J. Immunol. 151, (1993).
- 342. Diniz, L. P. *et al.* Astrocyte Transforming Growth Factor Beta 1 Protects Synapses against Aβ Oligomers in Alzheimer's Disease Model. *J. Neurosci.* **37**, 6797–6809 (2017).
- 343. Yuan, P. *et al.* TREM2 Haplodeficiency in Mice and Humans Impairs the Microglia Barrier Function Leading to Decreased Amyloid Compaction and Severe Axonal Dystrophy. *Neuron* **90**, 724–739 (2016).
- 344. Meyer-Luehmann, M. *et al.* Exogenous induction of cerebral β-amyloidogenesis is governed bf agent and host. *Science* (80-.). **313**, 1781–1784 (2006).
- 345. Stöhr, J. *et al.* Purified and synthetic Alzheimer's amyloid beta (Aβ) prions. *Proc. Natl. Acad. Sci. U. S. A.* **109**, 11025–11030 (2012).
- 346. Ruiz-Riquelme, A. *et al.* Aβ43 aggregates exhibit enhanced prion-like seeding activity in mice. *Acta Neuropathol. Commun. 2021 91* **9**, 1–19 (2021).
- 347. Kumar, S. *et al.* Extracellular phosphorylation of the amyloid β -peptide promotes formation of toxic aggregates during the pathogenesis of Alzheimer's disease. *EMBO J.* **30**, 2255–2265 (2011).
- 348. Saido, T. C. *et al.* Dominant and differential deposition of distinct β-amyloid peptide species, AβN3(pE), in senile plaques. *Neuron* **14**, 457–466 (1995).
- 349. Schilling, S. *et al.* Glutaminyl cyclase inhibition attenuates pyroglutamate Aβ and Alzheimer's disease–like pathology. *Nat. Med.* 2008 1410 **14**, 1106–1111 (2008).
- 350. Nussbaum, J. M. *et al.* Prion-like behaviour and tau-dependent cytotoxicity of pyroglutamylated amyloid-β. *Nat. 2012 4857400* **485**, 651–655 (2012).
- 351. Yang, Y. *et al.* Cryo-EM structures of amyloid-b 42 filaments from human brains. *Science (80-.).* **375**, 167–172 (2022).
- 352. Novotny, R. *et al.* Conversion of synthetic Aβ to In Vivo active seeds and amyloid plaque formation in a hippocampal slice culture model. *J. Neurosci.* **36**, 5084–5093 (2016).
- 353. Liu, C. C. et al. ApoE4 accelerates early seeding of amyloid pathology. Neuron 96, 1024 (2017).
- 354. Castellano, J. M. *et al.* Human apoE isoforms differentially regulate brain amyloid-β peptide clearance. *Sci. Transl. Med.* **3**, (2011).

6. Danksagung

Zuerst und besonders möchte ich Dominik danken, der mich in das Feld der Stammzellen und ihrer Möglichkeiten gebracht und mir die essenziellen Grundlagen beigebracht hat, mir die Möglichkeit gab, an diesem spannenden Projekt zu arbeiten, immer mit Rat und Tat zur Seite stand, mich beruflich immer gefördert und gefordert und die Teilnahme an vielen Konferenzen unterstützt hat.

Ein weiterer besonderer Dank geht an alle derzeitigen und früheren Mitglieder des Labors. Ich danke Angelika, der besten Tischnachbarin, die man sich wünschen kann, für all die Hilfe im Labor, all die mal mehr mal weniger tiefgründigen Gespräche und für viele schöne, gemeinsame Erlebnisse auf Bergen und in Wäldern, in Biergärten, Bars und Boulderhallen, auf Konferenzen und deren Parties, und und und. Ein großer Dank auch an Carolina für all die Hilfe beim Etablieren, Optimieren und Umsetzen der Experimente, für die Urlaubs- und Krankheitsvertretungen, und natürlich auch für die schönen und lustigen Abende außerhalb des Labors und die generelle unbegrenzte Hilfsbereitschaft und zahlreichen Geschenkideen/gestalteten Karten/Basteleien. Ich danke insbesondere auch Judit und Joey, Sophie, Alex, Meike, Jojo und Lili für die vielen lustigen Abende und Parties, die das Doktorandenleben immer versüßt haben, und dafür das sie immer für eine Ablenkung von der Arbeit zu begeistern waren. Vielen Dank auch an Dennis und Jenny, die das Labor am Laufen halten und immer wieder den Kampf gegen die Bürokratie, globale Lieferengpässe und das Bestellsystem für uns gewonnen haben. Ich danke außerdem Isabel für die gute Zusammenarbeit beim Aufbau des Labors und den vielen Etablierungen und Optimierungen und die Einführung in die Münchner Boulderwelt. Ein weiterer Dank geht an Annika Wagener, Merle Bublitz und Gülce Işıl Gökçe, die ich während meiner Arbeit betreuen durfte und die mir bei Experimenten und Analysen geholfen haben.

Ein großer Dank geht auch an alle, die mir bei der Umsetzung der Arbeit geholfen haben, durch die Hilfe bei Experimenten oder das Bereitstellen von Gerätschaften, Chemikalien, Antikörpern und samples. Dazu gehören Stephan Müller, Severin Filser, Lars Paeger, Brigitte Nuscher, Markus Utzt und Luisa Mutschler, Laura Sebastián Monasor, Martina Schifferer, Giovanna Sonsalla, Johannes Trambauer, Alexander Siebert, Miriam Christlmeier, Gernot Kleinberger und Maryam Khojasteh-Fard. Außerdem möchte ich Prof. Christian Haass und Prof. Thomas Misgeld danken für das hilfreiche Feedback in meinen TAC-Meetings, und dem gesamten Team der GSN für die Organisation all der Events und der immer schnellen und kompetenten Hilfe bei Fragen und Problemen.

Ich danke außerdem allen, die mich in meiner bisherigen beruflichen Laufbahn unterstützt und gefördert haben: Prof. Karlhans Endlich, Prof. Oliver von Bohlen und Halbach, Prof. Dagmar Galter, Dr. Ana Oliveira und Prof. Matthew LaVoie.

Ein weiterer Dank geht an Toni, Paul und Dorle und Jojo für unvergessliche Urlaube, die einen das Doktorandenleben sofort haben vergessen lassen, und generell die langjährige wunderbare Freundschaft trotz der räumlichen Distanz.

Ganz besonders möchte ich außerdem meinen Eltern und meinem Bruder danken für die ständige und bedingungslose Unterstützung in vielerlei Hinsicht und alles, was sie mir mit auf den Weg gegeben haben und immer noch geben. Ich bin mehr als froh und glücklich, euch zu haben.

Mein größter Dank gilt Hannah. All die Dinge aufzuzählen, für die ich dir dankbar bin, würden dieses Format hier sprengen, daher mache ich das später persönlich.

7. Curriculum Vitae – Julien Klimmt

Ed		~~	٠.	\sim	-
ГП				.,	
_~	•	·		•	

04/2017 – today	PhD Student in the group of Prof. Dominik Paquet, LMU Munich	
10/2014 – 03/2017	M.Sc. Molecular Biosciences – Major Neurosciences, University of Heidelberg Final grade: 1.0	
10/2011 – 9/2014	B.Sc. Human Biology, University of Greifswald, Final grade: 1.0	
09/2010 – 05/2011	Community service, Medical Center Chemnitz, Neuropsychiatric ward	
08/2002 – 06/2010	Johannes-Kepler-Gymnasium Chemnitz, In-depth STEM profile, Final grade (German Abitur): 1.2	
Practical experience		
04/2017 – today	Institute for Stroke and Dementia Research, LMU Munich, Prof. Paque (PhD project) - Generation of 3D cell cultures with Crispr/Cas9 edited, human iPSC- derived neurons and glia as new model for neurodegenerative diseases	
04/2016 – 02/2017	Interdisciplinary Center for Neurosciences (IZN), University of Heidelberg, Dr. Oliveira (Master thesis)	

 Examining the role of DNMT3a1 in memory formation using shRNA mediated knockdown of Dnmt3a1 mRNA in mouse hippocampus

09/2015 - 02/2016

Ann Romney Center for Neurologic Diseases, Harvard Medical School/ Brigham and Women's Hospital, Boston, Prof. LaVoie

> Examining the function of Parkin in the cytosol of Pink1-null Hela cells, dopaminergic rat neurons and iPSC-derived neurons using biochemical methods

03 - 09/2014

Institute for Anatomy and Cell Biology, University of Greifswald, Prof. von Bohlen und Halbach (Bachelor's thesis)

 Examining the density of dopaminergic neurons and neurites as well as the rate of neurogenesis in fixed brain slices of Ca_v1.3knockout mice treated with MPTP (Parkinson's disease model)

08 - 09/2013

Karolinska Institute, Department of Neuroscience, Prof. Olson

 Dissection of the enteric nervous system of MitoPark mice and examination of expression patterns of different mRNAs specific e.g. for dopaminergic neurons

8. List of publications

Reifschneider A, Robinson S, van Lengerich B, Gnörich J, Logan T, Heindl S, Vogt MA, Weidinger E, Riedl L, Wind K, Zatcepin A, Pesämaa I, Haberl S, Nuscher B, Kleinberger G, **Klimmt J**, Götzl JK, Liesz A, Bürger K, Brendel M, Levin J, Diehl-Schmid J, Suh J, Di Paolo G, Lewcock JW, Monroe KM, Paquet D, Anja Capell A, Haass C. (2022) Loss of TREM2 reduces hyperactivation of progranulin deficient microglia but not lysosomal pathology. **EMBO J** 2022 Jan 12; e109108

Weisheit I, Kroeger JA, Malik R, **Klimmt J**, Crusius D, Dannert A, Dichgans M, Paquet D. (2020) Detection of deleterious on-target effects after HDR-mediated CRISPR editing. **Cell Reports** 31:107689

Klimmt J*, Dannert A*, Paquet D. (2020) Neurodegeneration in a dish: advancing human stem-cell-based models of Alzheimer's disease. **Current Opinion in Neurobiology** 61:96-104. Review *equal first authors

9. Eidesstattliche Erklärung/Affidavit

Julien Klimmt

Hiermit versichere ich an Eides statt, dass ich die vorliegende Dissertation "A human stem-cell-derived cortical tissue model to investigate Alzheimer's disease" selbstständig angefertigt habe, mich außer der angegebenen keiner weiteren Hilfsmittel bedient und alle Erkenntnisse, die aus dem Schrifttum ganz oder annähernd übernommen sind, als solche kenntlich gemacht und nach ihrer Herkunft unter Bezeichnung der Fundstelle einzeln nachgewiesen habe.

I hereby confirm that the dissertation "A human stem-cell-derived cortical tissue model to investigate Alzheimer's disease" is the result of my own work and that I have only used sources or materials listed and specified in the dissertation.

München/Munich, 9.6.2022	Julien Klimmt		

10. Declaration of author contributions

Chapter 3.1: Neuron differentiation was optimized by Dominik Paquet (DP), based on the protocol by Shi et al. ²⁵². The protocol was established and further optimized in the lab by Julien Klimmt (JK), Isabel Weisheit (IW) and Dennis Crusius. Neurons for experiments were differentiated by JK and partially by Carolina Cardoso Gonçalves (CG). Astrocyte differentiation from the protocol by TCW et al. ²⁵¹ was established and characterized by JK. Astrocyte differentiation from the protocol by Perriot et al. ¹⁵⁰ was established and characterized by JK and CG. Astrocytes for experiments were differentiated by JK and CG. Microglia differentiation was established, optimized, and characterized by Gernot Kleinberger, Maryam Khojasteh-Fard, Miriam Vogt and JK. Microglia for experiments were differentiated by JK and CG.

Chapter 3.2: Matrigel cultures were established, optimized, and characterized by JK. 3BTM cultures were established and optimized by JK and CG.

Chapter 3.3: Characterization of 3BTMs by stainings were done by JK and CG. Mass spectrometry experiments were prepared by JK and performed by Stephan Müller (SM) at the Synergy Proteome Hub at AG Lichtenthaler (DZNE Munich). Mass spec data analysis was performed by SM and JK. Calcium imaging of 3BTMs was performed by JK, electrophysiology experiments were prepared by JK and performed and analyzed by Lars Paeger at AG Herms (DZNE Munich). 2-Photon live cell imaging experiments were prepared by JK and performed by JK and Severin Filser at AG Plesnila (ISD).

Chapter 3.4: Gene editing and quality controls were performed by JK

Chapter 3.5: KI 3BTMs for A β measurements were prepared by JK, for stainings by JK and CG. Single mutation lines and cultures for A β measurements were generated by Merle Bublitz. A β measurements were done by Brigitte Nuscher at AG Haass, DZNE Munich. Sequential protein extractions were done by JK and CG. Phospho-Tau western blots were done by JK. ScRNA sequencing experiments were prepared and optimized by JK, 3BTMs for scSeq were prepared by JK. Library preparation and sequencing as well as initial data quality controls and analysis was performed together with AG Beltrán (BMC Munich). Further scRNAseq data analysis was performed by JK and Gülce Isil Gökce. Experiments to induce plaque formation in 3BTMs (Matrigel embedding, seeding etc.) were done by JK.

Julien Klimmt	Prof. Dominik Paquet			